

(Annual Report) 1999-2000

## 1. Metabolic Studies of $^{11}\text{C}$ in Rabbit Thigh Muscle Implanted by Secondary Beams of HIMAC

Takehiro Tomitani, Joerg Pawelke<sup>1</sup>, Mitsutaka Kanazawa, Kyosan Yoshikawa, Katsuya Yoshida<sup>2</sup>, Mikio Sato<sup>2</sup>, Toru Takami<sup>2</sup>, Masahisa Koga, Yasuyuki Futami, Atsushi Kitagawa, Eriko Urakabe<sup>3</sup>, Mitsuru Suda, Tatsuaki Kanai, Hajime Matsuura<sup>4</sup>, Ikuhiro Shinoda<sup>4</sup> and Shigeo Takizawa<sup>4</sup> (<sup>1</sup>Forschungszentrum Rossendorf, Germany ; <sup>2</sup>School of Medicine, Chiba Univ <sup>3</sup>Institute for Chemical Research, Kyoto Univ <sup>4</sup>Simens-Asahi Medical Technologies Lid.)

**Keywords:** radioactive ion beam, metabolism, biological half-life

The accuracy of dose distribution of heavy ion therapy depends on the range estimation of ions in the target medium. Heavy ion range is estimated from the measured CT number by looking up a measured conversion table. The heavy ion range is a function of the electron density of the medium, while CT number is related to X-ray absorption coefficient and is a complex function of electron density, chemical composition and atomic numbers of the constituent elements. The empirical conversion leaves some ambiguities and some experimental checking means is needed. With  $\beta^+$  emitting ion beams, we can measure the end-points of heavy ions by measuring annihilation pair  $\gamma$  rays with a positron emission tomography (PET) or a positron camera. In our institute,  $^{12}\text{C}$  beams produced by HIMAC have been in use for heavy ion therapy. The secondary beam generator/separator was built in 1998. The  $^{11}\text{C}$  beam was selected, since its LET is the same as that of  $^{12}\text{C}$  and its half-life is 20.39 minutes, which is appropriate for the measurement. One ambiguity with the use of the positron emitter is the metabolism of implanted  $^{11}\text{C}$  inside living objects. We have already measured the metabolism of  $^{11}\text{C}$  generated through autoactivation of the  $^{12}\text{C}$  beam, in which the activity level is quite low, since  $^{11}\text{C}$  is the product of the fragmentation reaction of  $^{12}\text{C}$  beams. With the same dose, the  $^{11}\text{C}$  beams allow us about 50 times higher activity and thus the  $^{11}\text{C}$  metabolism can be measured with high accuracy. We measured metabolic rates of  $^{11}\text{C}$  inside the thigh muscle of rabbits with radioactive  $^{11}\text{C}$  ion beams with an off-site PET and an in situ positron camera. The latter instrument allowed measurement of the earlier transition and the result was compared with that obtained with PET.

Irradiation of  $^{11}\text{C}$  beams and PET emission measurement of the rabbit were performed under anesthesia to avoid movement. The rabbit was sacrificed after the emission measurement, since anesthesia can be maintained at most for 2 only hours. After the emission measurement, five markers loaded with  $^{18}\text{F}$  were attached on the body surface and measured with PET then the transmission measurement was performed. The rabbit with markers was transferred to the X-CT device and the CT scan was performed to see its anatomical structure. The markers were used to adjust two kinds of images. The same procedures were used for live and dead conditions. The experimental plan of rabbit experiments was approved by the committee for ethics in animal experiments in our institute.

The results of time-activity analyses measured with PET are shown in the left graph of [Fig.1](#). Measured half-life of the dead rabbit is 20.3 minutes, while that of the live rabbit is 16.0 minutes from which biological half-life is

74 minutes, or about 4 times longer than the physical half-life. The estimated initial activity of the live one is about 1/3 that of the dead one, which suggests the existence of a faster component. Due to the time for transportation of the rabbit from the irradiation site to PET site, the earlier transition cannot be measured with off-site PET. With an in situ positron camera, the earlier clearance can be observed. Counts in region-of-interest (ROI) versus time are shown in the right graph of [Fig. 1](#). The existence of the fast component is revealed. Biological half-life of the slow component is 89 minutes. Biological half-life of the fast component is 3.6 minutes. The initial activity is 0.74 of that under dead condition. This suggests the existence of an even faster third component that could not be measured due to the finite irradiation time of about 100 seconds.

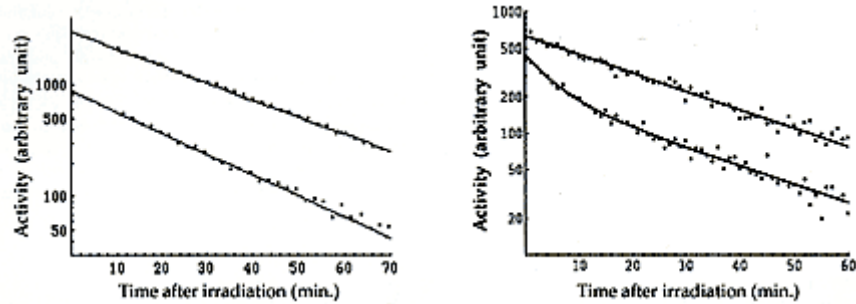


Fig.1. Time-activity curves. The left figure shows time-activity curves inside the ROI under live (lower) and dead (upper) conditions measured with off-site PET. The right figure shows time-activity curves under live (lower) and dead (upper) conditions measured with an in situ positron camera.

#### **Publications:**

- 1)Tomitani, T., Pawelke, J., Kanazawa, M. Yoshikawa, K., Yoshida, K., Sato, M., Takami, T., Koga, M., Futami, Y., Kitagawa, A., Urakabe, E., Suda, M., Kanai, T., Matuura, H., Shinoda, I. and Takizawa, S.: Jap. J. Med. Phys. 19, 192-195 1999.
  - 2)Tomitani, T., Futami, Y., Iseki, Y., Kouda, S., Nishio, T., Murakami, T., Kitagawa, A., Kanazawa, IVI., Urakabe, E., Shinbo M. and Kanai, T.: Conference Record of 1999 IEEE NSS/ MIC M7-29 1999.
-

## 2. High-speed Scanning of Atomic Force Microscope

**Nakahiro Yasuda<sup>1</sup> Mikio Yamamoto Mieko Kurano, Kuniaki Amemiya<sup>1</sup> Kazuyuki Uchikawa<sup>2</sup>, Hiromi Kanamaru<sup>3</sup> Yasuhisa Yamashita<sup>3</sup>, Hiroyuki Takahashi<sup>1</sup> Masaharu Nakazawa<sup>1</sup> and Koichi Ogura<sup>4</sup> (1Univ. of Tokyo; 2Toho Univ.; 3Toyo Corporation ; 4Nihon Univ.)**

**Keywords:** CR-39, atomic force microscope, high-speed scanning

The atomic force microscope (AFM) was introduced into the measurement of etch pits on CR-39 detector for the dosimetry under the high-density irradiation condition of the heavy ion beam. In this method, an individual etch pit can be measured even under the condition of  $10^8$  ions/cm<sup>2</sup> by shortening etching time. Quick analysis and/or in situ observation in the irradiation can be expected, since pretreatment of the surface is not needed, even for the insulator quality like the CR-39 detector. However, its scanning speed is too slow, it takes about 10 minutes/image. A application to fields which need statistics such as dosimetry is prevented by this slow speed. The AFM equipped with a 125  $\mu$ m cantilever having a typical probe tip length of 10  $\mu$ m. The sample surface is scanned over using this cantilever. The cantilever is driven by piezoceramic actuators, which change their dimensions according to the applied voltage. The AFM is usually operated in air in the tapping mode that has been developed as a method to achieve high resolution without inducing destructive frictional force. However, in the tapping mode, the probe tip scans by oscillating, and the probe tip does not follow a rapid change in ruggedness of the sample surface for high-speed scanning. It has been considered that the measuring speed for obtaining a clear image is limited to about 10 minutes/image (scan rate = 1Hz) using the tapping mode. Using the AFM (D3100: Digital Instruments) in the contact mode, we examined the effect on the image at high-speed scanning. In the contact mode, the probe tip is simply dragged across the surface. The dragging motion of the probe tip, combined with adhesive forces between the tip and the surface, can cause substantial damage to both sample and probe tip and create artifacts in image data. This scanning method, however, may be able to withstand high-speed operation better than the tapping mode, since the sample always has contact with the probe tip. The CR-39 sample was irradiated by 290 MeV/n C ions from HIMAC and etched for 40 minutes under the conditions of 7N NaOH solution and 70 °C. The sample was measured over the area of 10 X 10  $\mu$ m<sup>2</sup> which consisted of 512 X 512 pixels. Scanning speed was varied from 512 (scan rate = 1Hz) to 9 (58Hz) seconds/image. The piezo scanner was calibrated using the grating (10.0  $\pm$  0.3  $\mu$ m pitch and 180  $\pm$  5.4nm) at the every scanning speed. [Figure 2](#) shows the image of the CR-39 surface with etch pits at the different scanning speeds (512, 17 and 9 s). The striped pattern (artifacts) that originally did not exist is observed, as the scanning rate is quickened. The diameter of etch pit is reduced in the scanning direction (the X direction in this case). The vertical for the scanning direction shows hardly any effect from the high-speed measurement. Since the probe tip does not follow the depth of an etch pit, the depth direction is obtained as an image which is shallower than the real shape. It is considered that the 17 s/ image (scan rate = 30Hz) is acceptable for the etch pit measurement. This scanning rate is almost equivalent to that of a scanning electron microscope. Recently, research on high-speed scanning is being widely carried out looking at the following two challenges: 1) a method with simultaneous scanning using multiple probes to increase the scanning area per time; 2) a method with feedback signal processing to the piezoactuator taking out information which is not easily affected by the scanning rate. By introducing the latter method, we are trying to construct the system that allows even higher measurement speed and the application of in vivo dosimetry for routine clinical usage

of heavy ions and/or protons as radiation therapy modalities.

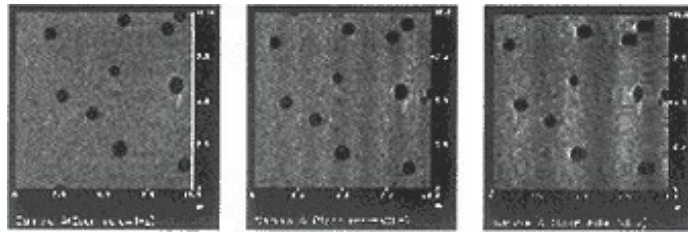


Fig.2. AFM images of CR-39 surface with etch pits. Scan rates are 1Hz(left), 30Hz(middle) and 50hz(right).

**Publication :**

K. Amemiya, H. Takahashi, M. Nakazawa, N Yasuda, M. Yamamoto, Y. Nakagawa, T. Kageji, M. Nakaichi, K. Ogura: Nucl. Inst. and Meth., B159 75-80 1999.

---

### 3. Parameter Analysis Method for Planar Type CdTe Detector with Its Output Pulse

**Masahiko Hirasawa and Mikio Yamamoto**

**Keywords:** CdTe, Schottky contact, dead region, mobility, pulse form

It is suggested in terms of spectrum analysis, photon counting, and so on that even planar type totally depleted semiconductor detectors with barrier contact include dead regions. A method is developed to derive the mobilities of electrons and holes, the dead region thickness, and so on by analyzing output pulse from a high resistivity CdTe gamma ray detector with Schottky barrier contact by the Pt cathode. The lifetimes of electrons and holes ( $\tau_e$  and  $\tau_h$ ) can be measured, but their mobilities ( $\mu_e$  and  $\mu_h$ ) are unknown because the measurement of the Hall coefficient is difficult with the high resistivity CdTe semiconductor.

For an easier calculation later, the dead region which is defined as the region of zero electric field in the electrically biased state is supposed as concentrated on the side of the anode. The thickness which is obtained by subtracting the total thickness of the dead regions from the real thickness of the CdTe detector is indicated by  $d$ . The electric field distribution in  $d$  is assumed to be approximately described by the linear expression  $ax + b$  where  $x$  is the distance from the anode, excluding the dead regions. The point of the photoelectric reaction is also expressed by the distance  $y$  from the anode, excluding the dead regions.

The output pulse form from the detector is broken at three points in almost all cases because the ratio of mobilities of electrons and holes is relatively big for semiconductors like CdTe. The  $V_1$  (voltage difference between the first and second broken point),  $V_2$  (between the first and third),  $T_1$  (time difference between the first and second broken point) and  $T_2$  (between the first and third) are analytically described by applying the system with energy conservation laws while the charge generated by the photoelectric reaction moves in the detector with the above electric field distribution. This leads to  $V_2/V_1$  and  $d$  as functions of only  $\mu_e$  and  $\mu_h$ ,  $a$  and  $b$  if  $\tau_e$  and  $\tau_h$  are known. The values of  $\mu_e$ ,  $\mu_h$ ,  $b$  and  $d$  for a given value of  $a$  are relatively easily solved from the values of  $V_1$ ,  $V_2$ ,  $T_1$  and  $T_2$  for the two pulses using the Newton-Raphson method independently of the initial values.

The pulses caused by the photoelectric reaction with gamma rays are measured using a 2-mm cube high resistivity CdTe with thin Pt electrode and 140 V of biased voltage. However largely different value sets of  $\mu_e$ ,  $\mu_h$ ,  $a$ ,  $b$  and  $d$  are reached by the calculation depending on the selection of a pair of pulses. This is thought to be mainly caused by ununiformity of  $\mu_e$  and  $\mu_h$  based on the inhomogeneous crystal and the impurity distribution in the detector. Accordingly the ratio of mean  $\mu_e$  and  $\mu_h$  in the detector is first estimated by the mean times to traverse the detector by electrons and holes which are measured using the pulses caused by the photoelectric reaction in the neighbourhood of the cathode and anode. Any pulse can be tested regarding the ratio of  $\mu_e$  and  $\mu_h$  using values of  $T_1$  and  $T_2$  and the pulse in which the ratio is nearest to the above one is selected and used as the optimum pulse. More pulse measurements provide more precise mean values of the parameters in this method.

#### **Publication:**

Hirasawa, M.: Nuclear Instruments and Methods in Physical Research, submitted.

---

## 4. Physiological Changes by Remote Influence

Hideyuki Kokubo, Mikio Yamamoto, Kimiko Kawano\* and Nobuo Fukuda (\*Nippon Medical School, Tokyo)

**Keywords:** electrodermal activity (EDA), skin conductance change, fluctuation, direct mental influence for living system (DMILS), anomalous cognition, telepathy

In the present experiment, two qigong practitioners were put in separate rooms with communication deprivation, while the authors measured physiological changes of one of the two, acting as a Receiver, when the other, acting as a Sender, attempted to give "remote influence" to the Receiver at a distance. These subjects had shown statistically significant coincidences of the time of their apparent motions in previous similar experiments by we had carried out<sup>2-3</sup>

The Receiver was seated in an electromagnetically shielding cage and the Sender performed only one "sending" motion per 80-second trial on double blinded and randomized conditions. The Receiver's skin conductances were sampled at a rate of 200Hz using an exosomatic method (DC 0.5V constant) When the Sender or Receiver pushed a switch as the event marker, output signals were produced. The signals were recorded as the sending time or the response time, along with EEG and other physiological data, by a recorder. Video cameras were set in each experimental room, and the whole process of the experiment was watched and recorded audiovisually at the central control room.

In the results of 35 trials, Receiver's EDA changes [ $\mu\text{S}$ ] were analyzed in the range of 5 seconds before or after the initial (or end) time of sending. While the average of EDA changes declined with fluctuation before the initial time, it declined linearly after that. The average of EDA changes also seemed to decline linearly both before and after the end of sending. Thus, for quantitative evaluation of fluctuations, the F-test was done on variances of the averages of EDA differences [ $\mu\text{S/s}$ ]. At first, the average of EDA differences was computed at every 0.05 second. Next, the 5-second frequency distribution of the average was obtained before or after the initial (or end) time of sending. The variance of the average of EDA differences after the initial time of sending was smaller than the one before. And the variance after the end time was larger than the one before ([Table 1](#)).

In the present experiment, there were no obvious changes in EEG, respiration and PPG.

In conclusion, fluctuation of the Receiver's skin conductance during "sending" was smaller than before and after. It was considered that these EDA changes were caused by remote influences and corresponded to the coincidence of the subject's motion times in the previous experiments.

Table 1. F-test on 5-second Frequency Distribution of Average of EDA Difference [ $\mu\text{S/s}$ ]

Time zone	Variance	F	Degree of freedom	P
Before initial time	.005229	1.809	99,99	0.00175
After initial time	.002891			
Before end time	.003799	0.4274	99,99	0.00002
After end time	.008890			

**Publications:**

- 1) Kokubo, H., Yamamoto, M., Hirasawa, M. Kawano K. Kokado, T., Taniguchi, J. and Fukuda, N.: J. Intl. Soc. LifeInfo. Sci., 18, 127-133, 1998.
  - 2) Yamamoto, M., Hirasawa, M., Kawano, K. Yasuda, N. and Furukawa, A.: J. Intl. Soc. Life Info. Sci., 14, 97-101, 1996.
  - 3) Yamamoto, M., Hirasawa, M., Kawano, K. Kokubo, H., Kokado, T., Hirata, T., Yasuda, N Furukawa, A. and Fukuda, N.: J. Intl. Soc. Life Info. Sci., 14, 228-248, 1996.
-

## 5. Physiological Measurements on Qigong Beginner

**Masataka Tanaka, Hideyuki Kokubo, Masahiko Hirasawa, Tomoko Kokado, Mikio Yamamoto and Kimiko Kawano\* (\*Nippon Medical School, Tokyo)**

**Keywords:** ECG, R-R interval, LF/HF, sympathetic nervous system, qigong

We have been periodically making physiological measurements of qigong beginners in a qigong school by Various Simultaneous Measurements (VSM) to study their value changes during qigong training. The present subject was a 38-year old male who started training 11 months ago. Measurements were done during foot massage for 15 minutes, standing posture qigong for 15 minutes and Soubikou (a dynamic qigong) for 4.5 minutes, each with the eyes closed and opened. Measurement items were ECGs (electrocardiograms: bipolar leads below the collarbones) and respiration patterns (thermocouple sensors on the mouth and the nose). Activity indexes (LF/HFs) of the sympathetic nervous system were calculated as follows. The data, from equal intervals of 0.175s, were calculated from R-R intervals in the ECGs with the cubic spline interpolation. The power spectrum was obtained from these 512 data by Fourier transform. LF was the area from 0.04 to 0.15 Hz and HF was the area from 0.15 to 0.5 Hz. LF/HF was calculated from them. Analysis data showed differences when the eyes were opened and closed ([Table 2](#)). 1) Both foot massage with the eyes closed and standing posture qigong with the eyes closed showed lower LF/HFs than when the eyes were opened. 2) Both foot massage with the eyes closed and standing posture qigong with the eyes closed showed longer respiration periods than when the eyes were opened. 3) Both foot massage with the eyes closed and Soubikou with the eyes closed showed smaller respiration amplitudes than when the eyes were opened.

Table 2. LF/HF and Respiration average with Eyes Closed and Eyes Opens

Item	Eye state	LF/HF	Respiration	
			Periods(second)	Amplitude( $\mu$ V)
Foot Massage	Closed	1.19	2.6	17.4
	Opened	1.44	2.2	19.1
Standing Posture Qigong	Closed	1.11	2.7	13.2
	Opened	1.24	2.6	13.6
Soubikou	Closed	-	2.1	8.8
	Opened	-	2.1	12.2

### Publication:

Tanaka M. Kokubo H. Hirasawa M. Kokado T., Taniguchi J., Yamamoto M. and Kawano K. : J. Intl. Soc. Life Info. Sci., 18, 98-108, 2000.

---

## 6. Reconstruction of Dose Distribution on CT-Image of a Patient

Manabu Mizota, Tatsuaki Kanai, Takashi Akagi, Haruo Yamashita, Munefumi Shimbo, Yasuyuki Futami, Ken Yusa and Masahiro Endo

**Keywords:** dose distribution, radiotherapy, RTP quality assurance

From the standpoint of quality assurance in radiotherapy, it is very important to compare the dose distributions realized by an irradiation system with the distribution planned by a treatment planning (RTP) system. For comparison of the two dose distributions, it is necessary to convert the dose distributions on CT images to those in a water phantom or convert the measured dose distributions to those on CT images. We developed tools for the visualization and comparison of these distributions.

To calculate the distribution on a CT-image from the measured dose, CT-images on the same planes as the measurements are extracted from a set of CT images in the RTP system. Water equivalent depth to each point on the plane from a beam source is calculated individually and an expected dose is derived by mapping on the measured distribution. Fitting of the depth-dose curve to the calculated SOBP curve also gives a biological distribution. Once calculated, dose distribution information can be easily handled to make a comparison to other calculations or to display in any form, such as color-coded isodose lines, or overlaid on the gray-scale CT-image.

As one example, Fig.3 illustrates differences between the RTP calculation distribution and one derived by this method using the same beam for treatment. In this figure, irradiation from the left side is separated into two fields by a block for eyeball protection. There are some under-dose or over dose areas near the border of the irradiation field, which is distinguished by colors.

In this way, quantitative comparison of dose distributions are made with anatomical information, which also gives a verification of the irradiation system in a very straightforward way. Together with developing a rapid dosimetry system, we intend to make use of this method to check the therapeutic beam for each patient.

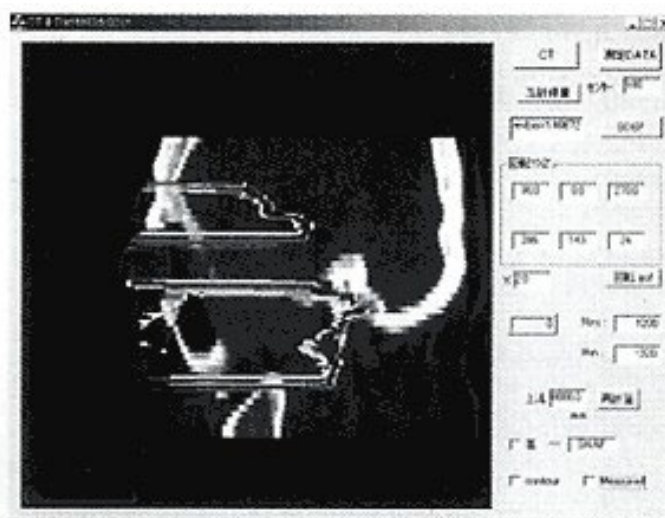


Fig.3. Colored biological dose difference between planning and reconstructed distribution from measurement. Areas of over 10% difference in the normalized to maximum value are painted.

# 7. Electron Emission from Foils: Application to the Beam Profile Monitor and Fast Detector

Yukio Sato and Daisuke Ohsawa

**Keywords:** secondary electron, foil, heavy ion, effective Live charge, stopping power

We precisely measured the secondary electron emission yield ( $\Upsilon$ ) from thin (1  $\mu\text{m}$  thick) Al-, Ag and Au-foils by exposure to fully stripped 6 MeV/n heavy ions (H, He, C, N, O, Ne, Si and Ar), which were accelerated by the HIMAC injector linac. The dependence of the forward ( $\Upsilon_F$ ) and backward ( $\Upsilon_B$ ) yields on the projectile nuclear charge ( $z$ ) showed a proportionality to the square of the effective Live charge ( $z_{\text{eff}}^2$ ) and an oscillatory behavior with atomic number  $z$ ; the yields were comparatively low for exposures to  $\text{He}^{2+}$  and  $\text{Ne}^{10+}$  beams. The forward enhancement was significant for Al-foil (light metal), depending on  $z$ ; in contrast, it was small for Ag- and Au-foils (heavy metals). The accuracy of the  $\Upsilon$ -values was evaluated by the determination of  $z_{\text{eff}}^2$  ( $\pm 5\%$ ) and the surface reproducibility of the foil ( $\pm 2\text{--}3\%$ ). Thus, the overall error was about  $\pm 6\%$ .

Figure 4 shows  $\Upsilon_F$  and  $\Upsilon_B$  from Al-foil scaled by  $z_{\text{eff}}^2$  in order to consider their correlation to the stopping power (the well known  $A$ ) and to compare our data with that of other experiments. The  $z_{\text{eff}}$  values were calculated using Ziegler's empirical formula, in which the accuracy is 5% for  $z$ -numbers of 6-92. For proton ( $z=1$ ) and helium ( $z=2$ ), this kind of accuracy could be much better. The best-fit results were  $\Upsilon_F \propto z_{\text{eff}}^{1.92}$  and  $\Upsilon_B \propto z_{\text{eff}}^{1.78}$ . The SE yield from foils was, to a first-order approximation, proportional to the stopping power; however, the characteristic obviously had an oscillation. The production mechanism of  $\delta$ -electrons or the behavior of two-center effects seemed to be related to this  $z$ -oscillation; the screening effects by target electrons in a continuum state may play an important role.

The ratio of  $\Upsilon_F/\Upsilon_B$  showed a large forward enhancement and its dependence on  $z$ , which suggested that many electrons initially ejected in the backward direction were pulled by the strong Coulomb field of a highly-charged projectile. For heavy metal (Ag and Au) foils,  $\Upsilon_F$  and  $\Upsilon_B$  were almost identical and the target dependence was small. These results showed that a sufficient relaxation of high-energy electrons occurred within dense materials, resulting in isotropic emission from the surface of heavy metal foils. Such secondary electrons (SE) are also applicable for a beam profile monitor and a fast detector, as briefly discussed in the following. Regarding sensitivity, the SE type monitor is compared with a conventional wire type. As can be seen from Fig.4, the forward SE yield from an Al-foil was around  $0.6z_{\text{eff}}^2(6/E)$  per ion, where  $E$  is the projectile energy (MeV per nucleon) and  $z$  is the projectile charge. Further, the induced charge on a wire was basically  $z$  per ion, if ions were stopped within the wire. In the energy region around 6 MeV/n, the SE type was more sensitive than the wire by a factor of  $0.6z$  (3.6 for  $z=6$ ), when  $z$  was roughly equal to  $z_{\text{eff}}$ . This meant that the SE type was particularly attractive for heavy ion beams. In addition, the energy loss within the foil was on the order of a few percent at this energy region; hence, this monitor can be used as a nearly non-destructive type. Using this SE emission from foils, we observed a micro-bunch structure of the HIMAC linac beams with a rise time of ns, which were accelerated at 100 MHz. The SE energy was generally lower than 20 eV and their traveling time between foils was of the order of 100 ps, which is comparable with that of the Pestov chamber. This fast-timing characteristic was also tested with a short-pulse obtained at the electron accelerator of the Nuclear Engineering Laboratory, University of Tokyo.

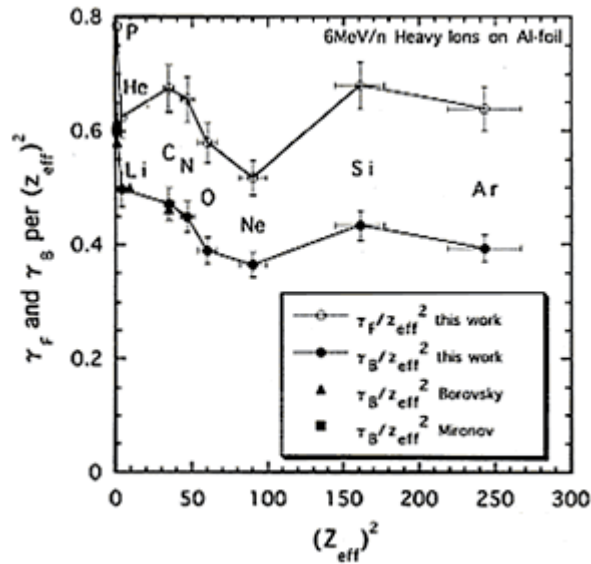


Fig.4.  $\gamma_F$  and  $\gamma_B$  per  $Z_{\text{eff}}^2$  on Al vs.  $z$  with exposure to 6 MeV/n heavy ions ( $\gamma_F^\infty Z_{\text{eff}}^{1.92}$  and  $\gamma_B^\infty Z_{\text{eff}}^{1.78}$ ). Some other data ( $H^{1+}$ ,  $Li^{3+}$ ,  $C^{6+}$ ) are also plotted, and  $z$ -oscillation can be clearly seen (Borovsky et al., Nucl. Instrum. & Meth., B36,377,1989 and B30,191,1988; Mironov et al., Sov. Ohys. JETP5, 188, 1957.)

**Publications:**

- 1) Sato, Y., et al.: Phys. Rev. A., 61, 0529011 0529016 2000.
  - 2) Iigashi, A., et al.: Proc. 12th Sympo. on Accel. and tech., 90-92, 1999.
  - 3) Ohsawa, D., et al.: Proc. BEAMS98 91-96 1998.
  - 4) Fujita, Y., et al.: Proc. EPAC98, 1503-1505, 1998.
-

## 8. A Depth Encoding Scintillation Detector Unit with a Position-sensitive Photomultiplier Tube

**Hideo Murayama**

**Keywords:** *scintillation detector, positron emission tomography, nuclear medicine*

A detector unit using a depth encoding scheme was designed. The unit consists of four  $\text{Gd}_2\text{SiO}_5:\text{Ce}$  (GSO) crystal blocks in a 2x2 array coupled to a position-sensitive photomultiplier tube (PS-PMT) having metal channel dynodes and 4x4 multi-anodes.

Figure 5 shows a schematic diagram of the detector unit. Element  $(i,j,k)$  represents the crystal segment which belongs to the  $i$ -th block and the  $j$ -th stage and is located on the  $k$ -th quadrant in a block. The four elements in the bottom stage in each block are optically coupled to the face plate of the PS-PMT, where each position of the sixteen bottom crystal elements in all the blocks corresponds to that of each anode segment. The position of a crystal element absorbing a gamma photon is detected by applying Anger-type position arithmetic to the output signals from PMT anodes. In each block, the crystal elements are coupled to each other with air gaps, various coupling compounds, or reflectors, so that the light sharing among elements can be optimized to identify each crystal element clearly in the positioning logic.

The dimensions of GSO crystal elements used in the following experiments to evaluate our proposed detector unit were 3.8 mm x 3.8 mm x 10 mm. Each crystal element of the top stage was optically coupled to another with air gaps, while each crystal element of the middle and bottom stages was optically separated from other elements in the same stage with two layers of 0.1 mm thick PTFE (polytetrafluoroethylene, Teflon) tape. Each stage of the 2x2 array was wrapped with a 0.2 mm thick PTFE tape and stacked together to form a threestage crystal block with Silicone oil (refractive index = 1.4). Four crystal blocks were coupled to a multi-anode PS-PMT (Hamamatsu R5900-M16). The R5900-M16 had an outline cross section size of  $26 \times 26 \text{ mm}^2$ , with the photocathode sensitive area of  $18 \times 18 \text{ mm}^2$ . It had 16 discrete channels arranged in a 4x4 array with individual readout through the segmented anodes.

A 0.1 mCi Cs-137 (662 keV) point source was used for gamma ray irradiation. Four 2D positioning histograms were obtained with the anode signals in four individual quadrants of the PS-PMT. In each histogram, 12 peaks were clearly visualized corresponding to the individual crystal elements. The energy resolutions for the bottom, middle and top stages were 17%, 21%, and 21% and the relative pulse height values for those stages were 1.0, 0.62 and 0.50, respectively. A fan beam of Cs-137 gamma rays was passed through a Pb slit collimator (slit width : 0.5 mm) and scanned along the side of the crystal blocks from the bottom stages to the top stages with 1.0 mm steps. The data were acquired in list mode and events were sorted using an island sorting method by which discrete islands were formed around each crystal element's position distribution in the positioning histograms. For each discrete island of the 2D positioning map, its energy threshold was set at 400 keV. The experimental results suggested that the light sharing method identified the depth of interaction should be a very reliable and simple solution suitable for volume PET devices since the proposed depth encoding scheme was constructed with all the same crystal elements and does not need additional photo-detectors nor a combination of different types of scintillators.

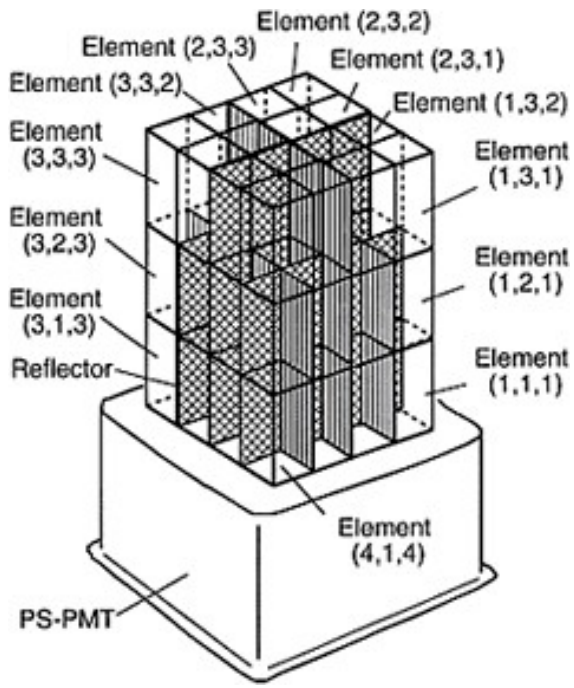


Fig.5. Schematic drawing of the depth encoding detector unit with a PS-PMT.

**Publication:**

Murayama, Fl., et al.: IEEE Trans. Nucl. Sci., 47 1045-1050 2000

---

# 9. A Build-up Treatment for Thickness Gauging of Steel Plates Based on Gamma-ray Transmission

**Yoshiyuki Shirakawa**

**Keywords:** *thickness gauging, gamma-ray transmission, build-up effect, steel plate, linear attenuation coefficient*

Gamma-ray thickness gauges are widely used in manufacturing plants such as hot strip mills and heavy plate mills of the steel industry. They are the most suitable instruments to carry out precise thickness control of steel sheets or plates in rolling mills. Much effort is needed to maintain these gauges, to keep their measuring accuracy and to calibrate parameters of conventional models installed in the gauges. The maintenance work is in general laborious because ordinary gauges have more than ten linear measurement models and they require the same number of standard steel plates for calibration. In order to decrease this work, a non-linear thickness measurement method with a new build-up model has been proposed and evaluated by using a real gamma ray thickness gauge.

A conventional gamma-ray thickness gauge employs many linear measurement models given by Eq (1),  
$$I = I_0 \exp(-\mu X_i) \quad (1)$$

where  $I_0$  and  $I$  are the numbers of incident and transmitted gamma-rays respectively,  $\mu$  ( $\text{cm}^{-1}$ ) is a linear attenuation coefficient of measured objects, in this case steel plates, and  $X_i$  (cm) is thickness in the  $i$ -th measuring range. The models deal with only a small measurement range each and the same number of standard steel plates is needed for model parameter calibration.

The proposed model with a variable linear attenuation coefficient ( $\text{cm}^{-1}$ ) shown in Eq. (2),

$$I = I_0 \exp(-\mu(X)X)$$

$$\mu(X) = (\mu_0/\beta)[\exp(-\alpha X) + (\beta - 1)] \quad (2)$$

where  $\mu_0$  is the ideal linear attenuation coefficient obtained under the condition of  $X \rightarrow 0$ ,  $\alpha$  and  $\beta$  are positive constants given by previous experiments, includes build-up effects in  $\mu(X)$ . The logarithmic expression of Eq. (2) is

$$K/x = \exp(-\alpha x) + M, \quad (3)$$

where  $K = -\beta/\mu_0 \ln(I/I_0) > 0$  and  $M = \beta - 1 > 0$

We consider two curves, which are

$$y_1 = K/x, \quad y_2 = \exp(-\alpha x) + M, \quad (4)$$

where  $y_1$  decreases from infinity to zero, and  $y_2$  from  $\beta$  to  $\beta - 1$ , monotonically as  $x$  increases. Hence, under these conditions, it is true that  $y_1$  and  $y_2$  intersect at only one point and the value  $x$  of the point is a solution of Eqs. (3) and (4). In practice, the intersection point is easily calculated with reasonable accuracy by the repetition method.

It was shown that the calculated values with the non-linear model of Eq. (2) were in good agreement with experimental data obtained by the gamma-ray thickness gauge in the range of 0-10cm thickness (Fig.6). The relative accuracy of thickness measurements was within  $\pm 0.05\%$  and the absolute accuracy was within  $\pm 2\mu\text{m}$  at the thickness range of 0-10cm. Hence the new model has a potential for real use in current thickness gauging systems for requirements of simplicity and easy handling.

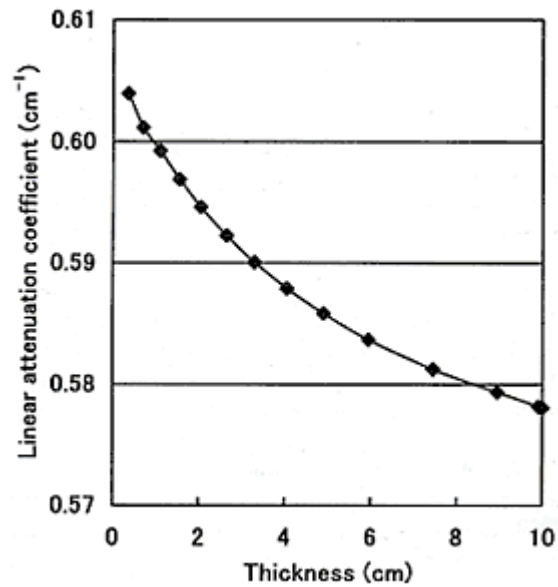


Fig.6. Experimental results of effective linear attenuation coefficients obtained by using a <sup>137</sup>Cs thickness gauge.

**Publications:**

- 1) Shirakawa, Y.: Applied Radiation and Isotopes, V4-4/2, 1-6, 2000
  - 2) Shirakawa, Y.: 4th Topical meeting of IRMMA99 189 1999
  - 3) Shirakawa, Y., Horikoshi, K., and Amano, H. IMEKO15, TC-14, 165-170, 1999
  - 4) Shirakawa, Y.: Horikoshi, K., and Amano, H. SICE, 35, 5, 693-695, 1999
  - 5) Shirakawa, Y.: Radioisotopes, 46, 371-377, 1997.
-

# 10. Adsorption Behavior of Ruthenium on Chitosan

Kiyoko Imai, Yoshikazu Nishimura and Kazuo Watari

**Keywords:** ruthenium, adsorption behavior, chitosan, sodium chloride solution

The chemical characteristics of ruthenium are quite complicated, because ruthenium possess many oxidation states and related compounds. Therefore, radioruthenium produced in relatively high fission yield shows complex behavior in nuclear fuel reprocessing, radioactive waste treatment, environmental samples and in the human body. In this study the authors have made experiments on the adsorption behavior of ruthenium on chitosan which is the deacetylated derivative of chitin. Chitin is distributed widely in nature, especially in shellfish and insects. This material is a cellulose-like biopolymer and known to be a natural chelating agents with adsorption ability for some heavy metal ions. This adsorbability is mainly due to the amino group presence. Adsorption experiments were carried out by the batch method to investigate the effect of chemical forms of ruthenium on the adsorption. Ten ml of sample solution containing 10-200  $\mu\text{g}$  of ruthenium labelled with  $^{103}\text{Ru}$  and 0.1g of chitosan were stirred in an erlenmeyer flask. Adsorption percentage was obtained by measuring the radioactivities of  $^{103}\text{Ru}$  in the supernatant solutions before and after a 20-hour agttatuon.

First, adsorption of chloro complexes of ruthenium ( $^{103}\text{Ru}(\text{III,IV})$ ) on chitosan was examined in distilled water, 1M hydrochloric acid solution and 1M sodium chloride solution. Ruthenium was effectively adsorbed in distilled water and 1M sodium chloride solution, while adsorption was negligible in 1M hydrochloric acid solution.

Adsorption behavior of chloro complexes and high oxidation state ruthenium anions ( $^{103}\text{Ru}(\text{VI})\text{O}_4^{2-}$ ,  $^{103}\text{Ru}(\text{VII})\text{O}_4^-$ ) on chitosan and cellulose powder is shown in [Table 3](#). Chitosan had relatively high adsorbability for both ruthenium SPCICI(IIS, while adsorptuon on cellulose was greatly influenced by its chemical forms. For comparison, other important radionuclides such as the fission products,  $^{137}\text{Cs}$ ,  $^{90}\text{Sr}$  and  $^{140}\text{Ba}$  or induced radioactive products,  $^{60}\text{Co}$ ,  $^{59}\text{Fe}$  and  $^{65}\text{Zn}$  were also examined using sodium chloride solution. It was found that chitosan could adsorb  $^{60}\text{Co}$ ,  $^{59}\text{Fe}$  and  $^{65}\text{Zn}$ . However, these nuclides except  $^{59}\text{Fe}$  were hardly adsorbed on cellulose. Adsorption of  $^{137}\text{Cs}$ ,  $^{85}\text{Sr}$  (to simulate  $^{90}\text{Sr}$ ) and  $^{133}\text{Ba}$  (to simulate  $^{140}\text{Ba}$ ) was negligible on both adsorbents. The results showed that adsorption of radionuclides such as  $^{60}\text{Co}$ ,  $^{59}\text{Fe}$  and  $^{65}\text{Zn}$  on chitosan was due to the formation of chelate compound. In the case of ruthenium, we thought that adsorption of chloro complexes was mainly due to formation of chelate compound, while adsorption of high oxidation state anions was due to formation of insoluble ruthenium dioxide ( $\text{RuO}_2$ ) by reduction.

In radiochemical analysis, an adsorption method is often used as the first step for concentrating and separating of desired radionuclides. Chitosan was successively applied to separating radionuclides of alkali and alkali earth elements from radioruthenium and other nuclides of transition elements.

Table 3. Effect of Chemical Forms on Adsorption of Ruthenium from 1M Sodium Chloride Solution

[Ru:200  $\mu\text{g}$ /10ml]

□@	Ru-chloro(III,IV)	$\text{RuO}_4^{2-}$ - $\text{RuO}_4^-$
cellulose powder	~5(%)	75%
chitosan	80(%)	95%

# 11. Asymmetric Synthesis of Stereoisomers of 2-(2,3-Dihydroxypropyl) piperidine Employing Double Asymmetric Dihydroxylation

**Nobuo Ikota and Hidehiko Nakagawa**

**Keywords:** piperidine alkaloid, asymmetric dihydroxylation, hydroquinine, regioselective cleavage, chiral synthesis

Optically active piperidine alkaloids show interesting biological activities and their synthesis has been a subject of recent research. From our continuing studies on synthesis of optically active polyhydroxylated piperidine alkaloids, we describe here the new asymmetric synthesis of both enantiomers of 2-(2-propenyl) piperidine via Sharpless asymmetric dihydroxylation of 5-hexenyl azide as the starting material, which was then converted into 2-(2,3-dihydroxypropyl) piperidine by a second asymmetric dihydroxylation. Asymmetric dihydroxylation of 5-hexenyl azide (1) using (DHQ)<sub>2</sub> PYR (hydroquinine 2,5-diphenyl-4,6-pyrimidinediyl diether) or (DHQD)<sub>2</sub> PYR (hydroquinidine 2,5-diphenyl-4,6-pyrimidinediyl diether) afforded the diols 2 and ent-2 shown in Fig. 7. These diols were converted into the epoxides 3 and ent-3 by one-pot procedure (1:CH<sub>3</sub>(COCH<sub>3</sub>)<sub>3</sub>; 2:CH<sub>3</sub>COBr; 3:K<sub>2</sub>CO<sub>3</sub>). The regioselective cleavage of the epoxide ring in 3 and ent-3 with vinylmagnesium bromide in combination with bromide-dimethyl sulfide complex was performed to yield the alcohol 4 and ent-4 in 75-86% yield, respectively. The treatment of 4 and ent-4 with mesyl chloride provided the corresponding mesylate, which was reacted with triphenylphosphine followed by hydrolysis in aqueous tetrahydrofuran to release the free amines, which immediately cyclized under inversion of configuration into the 2-propenylpiperidine 5 and ent-5 in 72 and 77% yields, respectively. The structure and optical purity of 5 were confirmed by conversion of 5 into the known (+)-coniine 6. Next, N-Z-protection of 5 and ent-5 (benzyl chloroformate/ K<sub>2</sub>CO<sub>3</sub>) gave 7 and ent-7 in 96% and 88% yields, respectively. Then, the second asymmetric dihydroxylation of the terminal olefin in 7 was carried out using (DHQ)<sub>2</sub> PYR to afford a readily separable mixture of the major diastereomer [2R-(2S)]-8 (>98% ee, 70% yield) and the minor diastereomer ([2R-(2R)]-8 (54% ee, 21% yield). On the other hand, the reaction of 7 using (DHQD)<sub>2</sub> PYR as the ligand gave [2R-(2R)]-8 (>98% ee, 69% yield) and [2R-(2S)]-8 (54% ee, 22% yield). Almost the same results were obtained in the double asymmetric dihydroxylation of ent-8 using (DHQ)<sub>2</sub> PYR ([2R-(2R)]-8 (>98% ee, 70% yield), [2S-(2R)]-8 (72% ee, 22% yield) and (DHQD)<sub>2</sub>-PYR ([2S-(2R)]-8 (98% ee, 74% yield), [2S-(2S)]-8 (47% ee, 14% yield)). Thus, all four stereoisomers of 2-(2,3-dihydroxypropyl) piperidine were prepared efficiently using the double asymmetric dihydroxylation reaction. The diols 8 could be useful intermediates for the naturally occurring piperidine alkaloids.

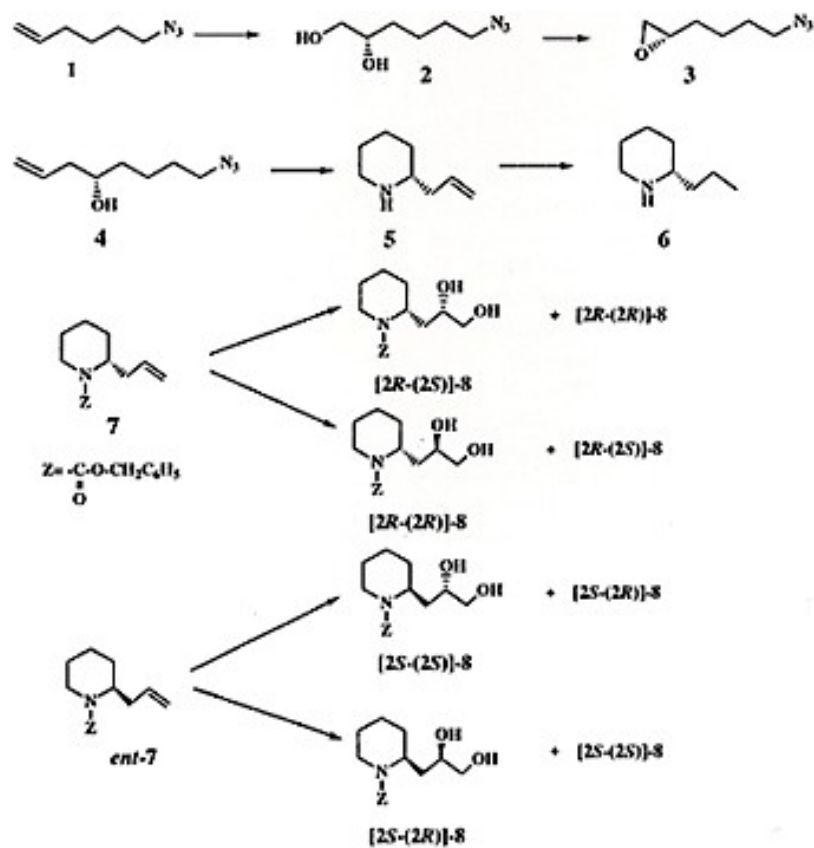


Fig.7. Synthetic Scheme for Optically Active 2(2,3- dihydroxypropyl) piperidines.

**Publication:**

Takahata, H, Kubota, M. and Ikota, N.: J. Org. chem., 64, 8594-8601, 1999.

## 12. Ascorbic Acid Inhibits the Oxidation of Linoleic Acid By Coaer (II) Complexes

Jun-ichi Ueda and Toshihiko Ozawa

**Keywords:** *ascorbic acid, linoleic acid, copper(II) complexes, lipid peroxidation, HPLC*

The oxidation of linoleic acid by Cu(II) (HGG) Cu(II)(en)<sub>2</sub>, or Fe(III)EDTA in the absence and presence of ascorbic acid was investigated by absorption spectroscopy and high performance liquid chromatography (HPLC). The absorbance at 234 nm due to the conjugated diene formed during Cu (II) or Fe(III)-catalyzed oxidation of linoleic acid increased with incubation time. However the addition of ascorbic acid to Cu(II) (HGG) or Cu(II) (en)<sub>2</sub> suppressed the increase in absorbance at 234 nm, depending on the increase in the concentration of ascorbic acid. By contrast, Fe(III)EDTA-mediated oxidation of linoleic acid was further accelerated by the addition of ascorbic acid.

A probable mechanism of Cu (II) -dependent oxidation of linoleic acid may involve the cleavage of preformed linoleic acid hydroperoxide (LOOH) in linoleic acid. Therefore, the amount of LOOH may be important to enhance the oxidation of linoleic acid. Then, to ascertain how ascorbic acid can influence Cu (II) -mediated oxidation of linoleic acid having a large amount of preformed LOOH, ascorbic acid was added to the reaction mixture after linoleic acid was incubated with Cu(II) (HGG) for 12 h. As a result, the absorbance at 234 nm at an ascorbic acid/ Cu (II) (HGG) ratio of 1 increased a little as compared with that in the absence of ascorbic acid.

When the molar ratio of ascorbic acid to Cu(II) (HGG) was 2:1, however, ascorbic acid suppressed the increase in absorbance at 234 nm. Furthermore, the absorbance at 234 nm due to LOOH decreased with the further addition of ascorbic acid, suggesting that LOOH was decomposed by Cu (I) (HGG) generated by the reduction of Cu(II) (HGG) with ascorbic acid. This was supported from HPLC results showing the disappearance of LOOH and the appearance of oxodiene compound. On the other hand, the addition of ascorbic acid to Fe(III)EDTA led to the promotion of Fe(III)- mediated oxidation of linoleic acid depending on the increase in the concentration of ascorbic acid.

Further the oxidation of linoleic acid by Cu(II) (HGG) or Cu(II) (en)<sub>2</sub> in the absence and presence of Trolox (a water soluble derivative of  $\alpha$ -tocopherol) was investigated by absorption spectroscopy and HPLC. The addition of Trolox to Cu(II) (HGG) or Cu(II) (en)<sub>2</sub> suppressed the increase in absorbance at 234 nm, depending on the increase in the concentration of Trolox. By contrast, Fe(III)EDTA-mediated oxidation of linoleic acid was completely inhibited by the addition of Trolox.

---

# 13. Radiation Induces Diacylglycerol Biphasic Production through Phosphoinoside-specific Phospholipase C and Phosphatidylcholine-specific Phospholipase C in Cultured Rat Hepatocytes

**Tetsuo Nakajima and Osami Yukawa**

**Keywords:** *rat hepatocytes, diacylglycerol, phosphoinosidespecific phospholipase C, phosphatidylcholine-specific phospholipase C, phospholipase D*

We have already reported that radiation induces protein kinase C (PKC) activation through radiation-induced lipid peroxidation. We also demonstrated that radiation induces diacylglycerol (DAG) biphasic production in cultured rat hepatocytes. DAG is a PKC endogenous activator and its DAG production might be related to radiation induced PKC signaling pathways. In the previous study, we suggested that DAG is produced by phosphatidylinositol-specific phospholipase C (PI-PLC) in the first production, using a generating system of hydroxyl radical, the main oxygen radical induced by radiation. But it remains unknown whether radiation induces PI-PLC activation. In addition, as it was reported that radiation induces phospholipase D (PLD) activation, PLD might participate in radiation-induced DAG production. PI-PLC produces inositol trisphosphates (IP<sub>3</sub>) and DAG. Though inositol phosphates including IP<sub>3</sub> are metabolized rapidly the metabolization is inhibited in the presence of LiCl. The inhibition results in accumulation of inositol phosphates. The accumulation can be an indicator to analyze rapid PI-PLC activation after irradiation. In this study, we investigated participation of PI-PLC and PLD in radiation- induced DAG production. Cultured rat hepatocytes were labeled with [<sup>3</sup>H] inositol, and the labeled hepatocytes were irradiated with 20 Gy in the presence of LiCl. Immediately after irradiation, inositol phosphates were fractionated by an SAX column. Accumulation of inositol phosphates involving IP<sub>3</sub> was observed in the fraction from the irradiated hepatocytes.

Though the accumulation might include other inositol phosphates, this result suggested participation of PI-PLC activation in radiation-induced DAG production. Measurement of the more purified IP<sub>3</sub> fraction is underway. Furthermore, PLD activity in hepatocytes was measured after irradiation. PLD activity was evaluated by measuring phosphatidylethanol production in the presence of ethanol in the labeled hepatocytes with [<sup>3</sup>H] myristic acid. However, PLD activity in irradiated hepatocytes showed no change within 1h after irradiation with 20 Gy. We have already suggested participation of phosphatidylcholinespecific PLC (PC-PLC) in radiation-induced DAG production. Overall, these results indicated that radiation induces DAG production through PI-PLC and PC-PLC.

Publication:

Nakajima, T. and Yukawa, O.: J. Radiat. Res., 40 135-144, 1999.

---

## 14. Discontinuous Translation and mRNA Structure of the Coding Region

**Mitsuo Zama**

**Keywords:** *translation, mRNA structure, silk fibroin*

Discontinuous translational elongation of polypeptides observed during the synthesis of proteins, silkworm fibroin, type I collagen, colicin A, chloroplast photosystem II reaction center protein D1, globin and spider fibroin, has been suggested to be attributable to the mRNA secondary structure of the protein-coding region by our preceding studies. We describe here the result of a further analysis on the correlation between discontinuous translation and mRNA structure in silkworm fibroin synthesis.

The products of fibroin being translated exhibit the ladder of electrophoretic bands smaller than fullsize fibroin in the SDS polyacrylamide gels, due to discontinuities or pauses in the translational process. Our detailed analysis of the published data of the electrophoresis of the fibroin heavy chain showed that the total number of the electrophoretic bands in the gel is about 60. On the other hand, it is known that most of the fibroin heavy chain gene (15kb) is composed of alternate arrays of crystalline and noncrystalline elements. By an analysis of the nucleotide sequence of the 3' end cDNA alone of the fibroin heavy chain gene of *Bombyx mori* available in the literature, we estimated that the total number of the alternate arrays repeating over the whole heavy chain gene is about 60. The results indicate that about 60 pauses occur during the translation of the mRNA. Furthermore, the coincidence of the total number of the electrophoretic bands with that of the alternate arrays suggests that one translational pause occurs at a specific site in each of the alternate arrays in the fibroin mRNA template.

---

# 15. Studies on Heavy Ion Radiation-induced Chromosome Aberrations on an Ionizing Radiation Sensitive Mutant Mouse Cell Line by Atomic Force Microscope

Masahiro Murakami, Masako Minamihisamatsu, Koki Sato\*, and Tsamu Hayata (\*Kinki Univ.)

**Keywords:** *chromosome aberration, heavy ion radiation, atomic force microscope*

Chromosome damage occurs following exposure of cells to ionizing radiation. The various types of chromosome aberrations, i.e. chromosome breaks, chromosome exchange, chromatid gaps, chromatid breaks etc., have been classified by light microscopy. Heavy ion radiation [classified as high linear energy transfer (LET) radiation], which densely deposits its energy along the path of particle radiation, causes clustered DNA breaks and various types of chromosome aberration.

Recently, atomic force microscope (AFM) imaging has been applied to radiation research for biological systems. AFM imaging revealed the specific induction of small DNA fragments by neutron irradiation. Shortening of plasmid DNA after  $\gamma$ -irradiation was observed by AFM.

We applied a new method employing AFM for nanometer-level structural analysis of chromosome damage induced by heavy ion irradiation. An X-ray sensitive mutant mouse cell line, SL3-147, was exposed to heavy ion [neon (an initial energy of 400 MeV/n) and carbon ion (an initial energy of 135 MeV/n)] radiation, then the fine structures of chromosome aberrations were visualized by AFM. After irradiation, the cells were kept under 5% CO<sub>2</sub> at 37 °C in a culture medium containing 0.05  $\mu$ g/ml of colcemid for 1.5h or 20h, and then collected. The cells were treated with a hypotonic solution of 0.075M KCl, fixed with methanol-acetic acid (3: 1) and then air-dried slides were prepared. The AFM can visualize the detailed structure of chromosomes on Giemsa stained or unstained samples. The surface of unstained chromosomes was rougher than that of those stained with Giemsa. A fibrous structure was observed on the unstained chromosomes. The structure of the break point induced by neon (LET=100keV/ $\mu$ m, 1.5Gy) or carbon ion (LET 100keV/ $\mu$ m, 1.5Gy) radiation was imaged by AFM. The fibrous structure was also observed in these break points. The section analysis revealed that chromosome fragments were connected by the chromatin fiber inside the chromatid gap. On the other hand, chromosomes with chromatid breaks were disconnected at the break region. These observations indicated that AFM is a useful tool for analysis of heavy ion radiation-induced chromosome aberrations.

---

## 16. Chemoprevention by Curcumin during Promotion Stage of Tumorigenesis of Mammary Gland in Rats Irradiated with Gamma-rays

Hiroshi Inano and Makoto Onoda

**Keywords:** chemoprevention, mammary tumor, curcumin

Epidemiological surveys suggest that diet has an impact on cancer incidence. Frequent consumption of vegetables and fruits decreases the risk for human cancer. Recently, attention has been focused on identifying dietary phytochemicals which have an ability to inhibit the processes of carcinogenesis. Extracts of plants or their fractionated ingredients were found to possess inhibitory effects against chemically induced carcinogenesis. Curcumin ([Fig.8](#)) is a major component of turmeric, the dried rhizome of *Curcuma longa* Linn which is commonly used as a yellow coloring and flavoring agent in food in Asian countries. We have evaluated the chemopreventive effects of curcumin on diethylstilbestrol (DES) induced tumor promotion of rat mammary glands initiated with radiation. Sixty-four pregnant rats received whole body irradiation with 2.6 Gy  $\gamma$ -rays from a  $^{60}\text{Co}$  source at day 20 of pregnancy and were divided into 2 groups after weaning. In the control group of 39 rats fed a basal diet and then implanted with a DES pellet for 1 year, 33 (84.6%) developed mammary tumors ([Fig.9](#)). Twenty five rats were fed a diet containing 1% curcumin immediately after weaning and received a DES pellet, the same as for the control. The administration of dietary curcumin significantly reduced the incidence (28.0%) of mammary tumors. Also, the incidence (12%) of pituitary tumors in the curcumin-fed rats was about one-fifth of that (56%) in the control rats. Multiplicity and Iballs index of mammary tumors were decreased by curcumin. Rats fed the curcumin diet showed a reduced incidence of the development of both mammary adenocarcinoma and ER(+)PgR(+) tumor in comparison with the control group. By long-term treatment of curcumin, body weight and ovarian weight were reduced, but liver weight was increased. Compared with the control rats, the curcumin-fed rats showed a significant reduction of serum prolactin, whereas, estradiol-17 $\beta$  and progesterone concentrations were not significantly different between the two groups. Curcumin did not have any effect on the concentration of free cholesterol, cholesterol ester and triglyceride. Feeding of the curcumin diet caused a significant increase of the concentrations of tetrahydrocurcumin, arachidonic acid and eicosapentaenoic acid, and a significant decrease of TBARS concentration in serum. Whole mounts of the mammary glands showed that curcumin yielded morphologically indistinguishable proliferation and differentiation from the glands of the control rats. These findings suggest that curcumin has a potent preventive activity during the DES-dependent promotion stage of radiation-induced mammary tumorigenesis.

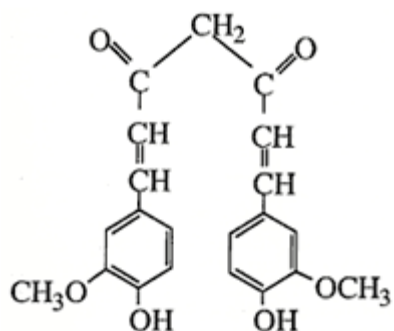


Fig.8. Chemical structure of curcumin. Chemical name: 1,7-bis (4'-hydroxy-3'-methoxyphenyl)-1,6-heptadiene-3,5-dione.

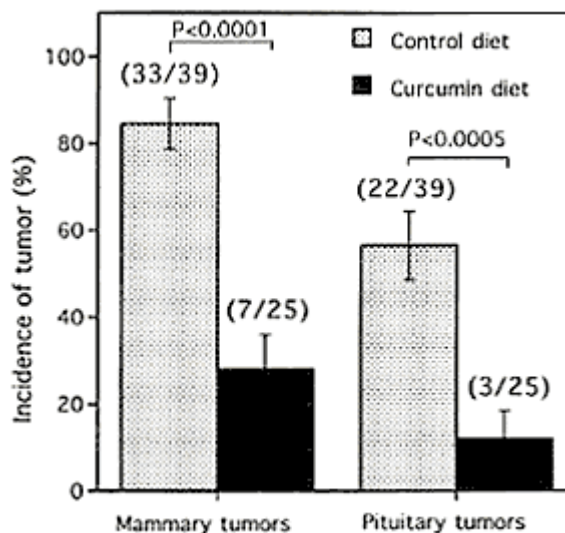


Fig.9. Incidence for mammary tumors and pituitary tumors in  $\gamma$ -ray-irradiated rats. Columns and vertical bars represent incidence(%) of tumor and standard deviation, respectively. The numbers in parentheses on the top of the bar represent the actual number of rats bearing tumors per rats used.

**Publication:**

Inano, H., Onoda, M., Inafuku, N., Kubota, M. Kamada, Y., Osawa, T., Kobayashi, H. and Wakabayashi, K.: Carcinogenesis, 20, 1011-1018, 1999.

# 17. Enhancement of Intracisternal A-particle RNA in Regenerated Myeloid Cells after Sub-lethal Doses of X rays in C3H/He Mice

Hiroshi Ishihara, Izumi Tanaka, Masako Furuse and Kazuko Tsuneoka

**Keywords:** radiation damage, myeloid cells, retrotransposon, intracisternal A-particle, transposition

Intracisternal A-particle (IAP) DNA element in sizes of 5-7 kb is one of the mouse retrotransposons and it is closely related with endogenous retrovirus in structure. Normal mouse genome contains more than one thousand copies of the IAP element per haploid. When the IAP RNA is reversely transcribed and re-integrated into genome, genetic information of the cells is modified. Even though the retrotransposition is considered as a rare event, many cases of IAP mediated gene rearrangement are reported in tumor as an event in somatic cells and in mutant mice as an event in the germ line.

Myeloid leukemia cells are derived from regenerated hematopoietic cells damaged by sub-lethal doses of x-ray irradiation in C3H/He mice. We have already found that the most of the leukemia cell lines generated from different individuals undergo IAP mediated retrotransposition in the genomic DNA. This indicates that the IAP element is activated in the myeloid cells after x-irradiation.

To clarify the behaviour of IAP element in mouse tissue, quantitative analysis of the IAP-RNA was conducted. In C57BL6 and STS/A inbred mice, basal IAP RNAs are detected only in the hematopoietic tissues such as thymus, spleen and bone marrow. In C3H/He inbred mouse, similar levels of IAP RNA are detected in non-hematopoietic tissues. In particular, the hematopoietic tissues of C3H mice possess 5 to 10-fold higher levels of basal IAP RNA than other tissues. This means that the C3H/He inbred mouse is IAP expressive strain. The decrease in the number of hematopoietic cells by whole body-irradiation of sublethal doses at 3Gy of x-rays recovers to the normal levels after 18 days. During and after the recovery step, the relative rate of IAP/ $\beta$ -actin RNA is increased in hematopoietic cells but not in non-hematopoietic cells (Fig. 10). The increase in the levels of IAP RNA is kept for at least 90 days after irradiation. This suggests that IAP tends to be activated in the recovered hematopoietic cells.

Among various types of IAP elements in the genome, all the retrotransposed ones at the rearranged sites in leukemia cells have a common structure in the nucleotide sequence at the regulator sequence of the promoter region. It is also found that the expression of this type of IAP is enhanced in all the leukemia cells. This shows that limited types in the IAP element population are activated in the leukemia cells. Since the IAP element behaves as an endogenous mutagen, the contribution of IAP in genomic instability should be considered.

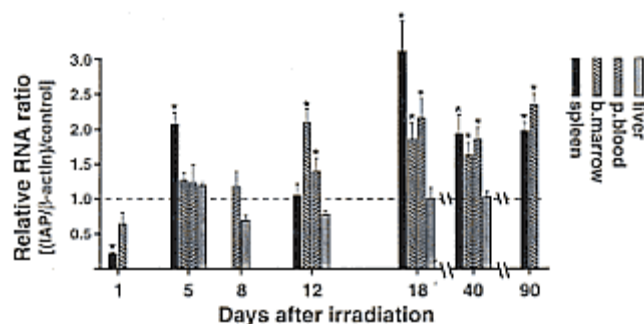


Fig.10. IAP expression during hematopoietic regeneration Spleen, femur, liver, and blood were isolated on the days indicated after

irradiation. For each period, 3 mice were analyzed separately. The RNA ratio of IAP /  $\beta$ -action to non-irradiated cells was calculated after quantitative Northern hybridization. The calculated relative RNA ratio values in hematopoietic (spleen, bone marrow and peripheral blood) and non-hematopoietic cells (liver) are shown with mean and standard deviation values for the relative RNA ratio of IAP /  $\beta$ -action among the 3 mice at each point. Asterisks(\*) indicate data at  $p < 0.05$  versus control by t-test.

**Publication:**

Ishihara, H., Tanaka, I., Furuse, M. and Tsuneoka, K.: Radiat. Res. 153, 392-397, 2000.

---

# 18. Singlet Oxygen Dependent Hydroxyl Radical Formation during Uroporphyrin-Photosensitization in the Presence of NADPH

**Keizo Takeshita, Claudio A. Olea-Azar Michiko Mizuno and Toshihiko Ozawa**

**Keywords:** singlet oxygen, hydroxyl radical, NADPH, photosensitization, uroporphyrin

The conversion of singlet oxygen ( $^1\text{O}_2$ ) to hydroxyl radical ( $\cdot\text{OH}$ ) during photosensitization of uroporphyrin (UP) in the presence of NADPH was examined by a spin-trapping technique using 5,5-dimethyl-1-pyrroline-N-oxide (DMPO).

Significant ESR signals of DMPO-OH adduct were observed during irradiation of the UP-NADPH system with visible light. Scavengers of  $\cdot\text{OH}$  reduced the signal intensity to 3-30 % of control, indicating that more than 70 % of DMPO-OH resulted from freely diffusing  $\cdot\text{OH}$  produced during irradiation of UP and NADPH, but not from decay of the  $\text{O}_2^-$  adduct of DMPO. The ESR signal almost completely disappeared when quenchers of  $^1\text{O}_2$  were added, and it was enhanced when the amount of deuterated solvent was increased. The appearance of  $^1\text{O}_2$  was determined by the oxidation of 2,2,6,6-tetramethyl-4 piperidone (TEMPD) to corresponding nitroxyl radical, 2,2,6,6 tetramethyl 4 piperidone N oxyl (TEMPO).

The ESR signal of TEMPO increased with an increase of irradiation time in the absence of NADPH. This signal significantly decreased when irradiation was performed in the presence of quenchers of  $^1\text{O}_2$  such as NaN<sub>3</sub> and L-histidine although  $\cdot\text{OH}$  scavengers, catalase, and SOD had less or no effect, indicating that oxidation of TEMPD to TEMPO was specific to  $^1\text{O}_2$  under this condition. The presence of NADPH delayed the appearance of TEMPO signal. The lag time increased with an increase in the concentration of NADPH. On the other hand, formation of DMPO-OH increased with the concentration of NADPH, when DMPO was used as a spin trapping agent instead of TEMPD. These observations implied that conversion of  $^1\text{O}_2$  to  $\cdot\text{OH}$  occurred quickly in the presence of NADPH. Hydrogen peroxide ( $\text{H}_2\text{O}_2$ ) was produced  $^1\text{O}_2$ -dependently during irradiation of UP in the presence of NADPH. However neither catalase nor desferrioxamine decreased the DMPO-OH signal, and addition of  $\text{H}_2\text{O}_2$  did not increase the signal. SOD slightly increased the signal. These results suggested that the production of  $\cdot\text{OH}$  from  $^1\text{O}_2$  involved neither superoxide anion radical nor  $\text{H}_2\text{O}_2$ .

## **Publication:**

Takeshita, K., Olea-Azar, C. A., Mizuno, M., and Ozawa, T. : Antioxidants and Redox Signaling, 2 355362 2000.

---

# 19. Difference in Calcium Mobilization between Human Leukemia Cell Line, HL60, and Its Hydrogen Peroxide Resistant Mutant Cell Line, HP100

**Kazunori Anzai and Guo-Jiang Zhang**

**Keywords:** HL60, HP100, fura-2, ATP, hydrogen peroxide, intracellular calcium

HP 100 is a hydrogen peroxide ( $H_2O_2$ ) -resistant cell line, which was constructed from HL60, a human leukemia cell line. In the present study, we have measured the change in the intracellular calcium concentration ( $[Ca^{2+}]_{in}$ ) responding to exogenous ATP or  $H_2O_2$  stimulation with fura-2 fluorescence technique.

HL60 and HP100 cell culture were maintained in (I -MEM supplemented with ION FBS.  $10 \mu M H_2O_2$  was added to the medium for HP100. Fura-2 was loaded inside the cells by mixing fura-2 AM ( $1 -2 /2M$ ) and the cell suspension ( $1-2 \times 10^6$  cells/ml) following incubation at  $37^\circ C$  for 1 h. The fura-2 loaded cells were washed with a buffer containing 141 mM NaCl, 5 mM KCl, 1 mM  $Na_2 HPO_4$ , 1 mM  $CaCl_2$ , 0.5 mM  $MgSO_4$ , 5 mM glucose, and 10 mM HEPES-Na (pH 7.4) and resuspended in the same buffer at  $1-1.5 \times 10^6$  cells/ml. The sample was kept at  $0^\circ C$  under dark until use within 4 h. The change in  $[Ca^{2+}]_{in}$  was measured at  $37^\circ C$  with an intracellular ion concentration monitor (JASCO CAFIIO)

ATP caused transient increase in  $[Ca^{2+}]_{in}$  both for HL60 and HP100 cells. The sensitivity to ATP in HL60 cells ( $EC_{50} \approx 0.5 \mu M$ ) was about five times higher than that in HP100 cells ( $EC_{50} \approx 2.5 \mu M$ ) ADP also caused similar transient increase in  $[Ca^{2+}]_{in}$ , but the sensitivity of these cells to ADP ( $EC_{50} : 16 \mu M$  for HL60) was lower than that to ATP. On the other hand,  $H_2O_2$  caused smaller increase in  $[Ca^{2+}]_{in}$ , and the recovery of  $[Ca^{2+}]_{in}$  to the basal level was slower than that observed by the stimulation with ATP. The maximum change in  $[Ca^{2+}]_{in}$  observed in HP100 cells was about twice larger than that observed in HL60 cells. Based on the results of time-dependent change in  $[Ca^{2+}]_{in}$  after extracellular calcium chelation with EGTA, existence of at least three compartments for calcium ion storage was suggested. The consecutive stimulation of ATP and  $H_2O_2$  or vice versa suggested that intracellular calcium pools responding to ATP and  $H_2O_2$  are at least partially different.

---

## 20. Increase in Spermidine / spermine N<sup>1</sup>-acetyltransferase mRNA as a Delayed Response of HeLa S3 Cells Following X-ray Irradiation

S. Ichimura, M. Neno, and K. Hamana\* (\*Gunma Univ.)

**Keywords:** X-ray irradiation, delayed cell death, polyamine, SSAT

In a broad range of biological organisms, including animals, plants, and microorganisms, polyamines mediate multiple essential functions such as DNA replication and protein biosynthesis. The cellular polyamine levels are regulated to maintain the optimal condition for the physiological state through biosynthetic, catabolic and transport pathways. Regulation of polyamines is also thought to be integral to the cellular response to toxic stresses. In fact, the polyamine catabolic enzyme spermidine/ spermine N<sup>1</sup>-acetyltransferase (SSAT) is activated by various anti-proliferative agents. For example N<sup>1</sup>, N<sup>11</sup> diethylnorspermtne, whrch us cytotoxic to cells and a potential chemotherapeutic polyamine analog for cancers, markedly enhances the cellular level of SSAT, while natural polyamine spermtne IS far less effective at increasing the SSAT levels. Our previous result LhxL SSAT mRNA accumulated at the plateau phase in HeLa cells suggests that SSAT mediates the growth arrest of these cells. In order to examine the contribution of SSAT to growth arrest following X-ray irradiation, we measured the intracellular levels of DNA, SSAT mRNA, ODC mRNA, 18S rRNA and polyamines at several days postirradiation.

Exponentially growing asynchronous HeLa S3 cells were irradiated by 2, 5 and 10 Gy X-rays and the proceeding growth was monitored according to DNA content. The growth was not inhibited up to 24 h after irradiation of even 10Gy in either series. The cell cycle of exponentially growing HeLa cells would be arrested after the first or second replication following X-irradiation. Total RNAs of cells in a dish were purified simultaneously with the DNA preparation at various post-irradiation times. 'The Northern blots of an aliquot of total RNA were hybridized with oligonucleotide probes for SSAT and ODC mRNAs and for 18S rRNA. SSAT mRNA increased after irradiation and reached a maxtmum amount at day 3. It is noteworthy that the increase in SSAT mRNA by X-ray treatment appeared suddenly at the beginning of growth inhibition. On the other hand, the ODC mRNA level decreased as the growth proceeded in both irradiated and non-irradiated cells, and reached the minimum level at day 2. The level of 18S rRNA, which would correlate with the translational activity, was maximal at day 1 and decreased gradually to a stationary state in control cells. The fact that X-ray irradiation had only a slight effect on the rRNA level suggests that the growth inhibition induced by X-ray irradiation was not due to the depression in translational activity

The content of individual polyamines among the cells adhering to each dish was also measured. As expected, the levels of N<sup>1</sup>-acetylspermidine increased in parallel with the enhancement of SSAT mRNA. The relatively lower level of acetylated polyamines would be due to rapid gradation by polyamine oxidase to reduced polyamines.

---

## 21. Transformed Keratinocyte Colonies in Serum-Free Primary Culture of Epidermal Cell Suspension from UVB Induced Pigmented Spots in Mice

**Tomohisa Hirobe**

**Keywords:** *melanoblast, melanocyte, keratinocyte, UVB, proliferation, differentiation*

Long-term exposure to ultraviolet radiation B (UVB) induced pigmented spots in the dorsal skin of hairless mice. To clarify the cellular mechanism for the development of these UVB-induced pigmented spots, epidermal cell suspensions from the dorsal skin of hairless mice at 37 weeks (the stage of development of medium-sized pigmented spots) after the cessation of 8-week UVB exposures were cultured in a serum-free medium supplemented with dibutyryl adenosine 3':5'-cyclic monophosphate (DBcAMP) and basic fibroblast growth factor (bFGF). After 14 days, most of the keratinocytes had died and pure cultures of melanoblasts and melanocytes were obtained. However, when the culturing of melanoblasts and melanocytes was continued further, numerous transformed keratinocyte colonies (3-20/35 mm dish) were observed after 20 days. It may be assumed that a small number of keratinocytes remained in the dishes, and they were initiated to proliferate dramatically. Around the colonies, numerous melanoblasts and melanocytes were observed and some of them were in mitotic division. On the other hand, no transformed keratinocyte colonies were observed in control culture. These results suggest the possibility that the increase in the number of melanocytes observed in pigmented spots is caused by the changes brought about by the transformation of keratinocytes.

### **Publication:**

Hirobe, T. and Abe, H.: *Pigment Cell Res.*, 12, 147-163, 1999.

---

## 22. Accelerated Reoxygenation of a Murine Fibrosarcoma after Carbon Ion Radiation

**Koichi Ando, Sachiko Koike, Chisa Oohira, Y. -J. Chen, Kumie Nojima, Soichiro Ando Toru Ohbuchi, Nobuyoshi Kobayashi, Wakako Shimizu and Muneyasu Urano**

**Keywords:** *tumor growth delay, lung colony, carbon ions, LET, OER*

Reoxygenation of a murine tumor after irradiation with carbon ions was investigated and compared to that after gamma ray irradiation. NFSa fibrosarcoma cells were transplanted into the right hind legs of syngeneic C3H male mice. Conditioning irradiation of either 290 MeV/u carbon ions or  $^{137}\text{Cs}$   $\gamma$ -rays was delivered to the tumors (8 mm diameter). At given times after irradiation, the leg tumors, either clamped or intact received test doses of photons. Difference in tumor growth delay between the clamped and non-clamped tumors were interpreted in terms of reoxygenation. A lung colony assay was used to obtain cell survival curves. The oxygen enhancement ratio of the NFSa tumor for 74 keV/ p m carbon ions was 1.6 while that for  $\gamma$ -rays was 3.4. The NFSa tumors reoxygenated 4 days after 30 Gy of  $\gamma$ -ray irradiation, but reoxygenated as early as 1 day after 16 Gy of carbon ions. Reoxygenation after  $\gamma$ -rays was shortened to 1 day when the tumors were initially clamped for the conditioning irradiation. We conclude that the fraction of surviving oxic cells in the NFSa tumors would be larger after irradiation with carbon ions than with  $\gamma$ -rays, resulting in accelerated reoxygenation.

### **Publication:**

Ando, K., Koike, S., Oohira, C., Chen, Y. -J., Nojima, K., Ando, S., Ohbuchi, T., Kobayashi, N., Shimizu, W. and Urano, M.: *Int. J. Radiat. Biol.* 75(4), 505-512, 1999.

---

## 23. Chromosome Breakage and Cell Lethality in Human Hepatoma Cells Irradiated with X-rays and Carbon Ion Beams

Masao Suzuki, Toru Ofuchi, Yoko Kase and Koichi Ando

**Keywords:** *hepatoma, colony formation, chromosome damage, premature chromosome condensation, heavy*

Prediction of radiosensitivity would be valuable for heavy ion radiotherapy. The premature chromosome condensation (PCC) technique is a potential predictive assay in photon radiotherapy, but it has not been investigated for hepatomas receiving heavy ions. Two human hepatoma cell lines, i.e., HLE and HLF, were irradiated with either 290 MeV/u carbon ions or 200 kVp X-rays. Cell lethality was assayed by colony formation and compared with the unrejoined fraction of chromatin breaks as measured by the PCC technique. Carbon ions at linear energy transfer (LET) of 76 keV/ $\mu$ m produced cell death more effectively than those of 13 keV/ $\mu$ m and X rays. Regarding the cell killing, relative biological effectivenesses (RBEs) of 13 and 76 keV/ $\mu$ m carbon ions, compared with X-rays, were 1.10-1.24 and 2.57-2.59, respectively. Mean numbers of chromosomes in HLE and HLF cells were similar i.e., 60.48 and 60.28. RBEs for chromatin breaks of 13 and 76 keV/ $\mu$ m carbon ions were 1.30-1.31 and 2.64-2.79 respectively. A strong correlation between unrejoined chromatin breaks and cell killing for human hepatoma cells was observed irrespective of radiation quality. We conclude that PCC is a potential predictor for the radiosensitivity of individual hepatoma that are treated with photons as well as heavy ion irradiation.

### **Publication:**

Ofuchi, T., Suzuki, M., Kase, Y., Ando, K., Isono, K. and Ochiai, T. : J. Radiat. Res., 40, 125-133, 1999.

---

## 24. TPA-induced Apoptosis Is Mediated by TNF $\alpha$ in Human Monocytic U937 Cells

**Makoto Akashi, Misao Haehiya, Sakae Tanosaki, Yoshikazu Kuroiwa, Yoshiko Kawase and Toshiyasu Iirama**

**Keywords:** *apoptosis, TPA, TNF $\alpha$ , TNFRI, MAPK*

12-O-tetradecanoylphorbol-13-acetate (TPA), a phorbol ester which is known as a tumor promoter induces differentiation of myeloid cells and suppresses their proliferation. We studied the regulation of apoptosis by TPA in human monocytic cell line U937 cells that lack p53. Untreated U937 cells constitutively underwent apoptosis and TPA enhanced apoptosis in these cells. Further studies showed that TPA increased production of tumor necrosis factor- $\alpha$  (TNF $\alpha$ ) in U937 cells, and exogenously added TNF $\alpha$  induced apoptosis. Moreover, the induction of apoptosis by TPA was blocked by anti TNF $\alpha$  antibody. Similar results were obtained in the myeloblastic cell line KY821 cells. We also found that the induction of apoptosis by TPA was increased in cells overexpressed with TNF receptor 1 (TNFR1) but not in control cells. Furthermore, TPA failed to induce the production of TNF $\alpha$  and apoptosis in cells with either their protein kinase C (PKC) or mitogen-activated protein kinase (MAPK) pathway blocked. Our results indicate that TPA induces apoptosis, at least in part, through a pathway which requires endogenous production of TNF $\alpha$  in U937 cells. Our data also suggest that the induction of apoptosis by TPA occurs through activation of PKC and MAPK, and TNF $\alpha$  as an autocrine-stimulating factor for the induction of apoptosis in these cells.

### **Publication:**

Takada, Y., Iiuchiya, I., O sawa, Y., Flasegawa, Y., Ando, K., Kobayashi, Y. and Akashi, M : J. Biol. chem. 274 28286-28292 1999.

---

## 25. p53 Deficiency Backcrossed into C3H/He Mice Produced High-incidence of Stemcell Leukemia after Irradiation

**Kazuko Yoshida, Shirou Aizawa and Yoko Hirabayashi\* (\*Visiting Scientist, National Institute of Health Sciences)**

**Keywords:** *p53 homo-deficient mice, stem-cell leukemia*

The mice lacking a p53 suppressor gene were developed independently in three laboratories by a gene-targeting strategy. Although these strategies differed, they were essentially all null mutants; the resulting homozygous deficient mice all are highly predisposed to malignancy, most often malignant lymphomas. Other types of tumors, including osteosarcomas, and hemangiosarcomas, also develop with some frequency. These mice have a mixed inbred genetic background of C57BL/6 and 129/SV or CBA. Purely bred C57BL/6 mice themselves are highly predisposed to lymphoma; therefore, the high frequency of lymphoma in p53-deficient mice reflects this genetic background. To test the effect of the genetic background on the spectrum of tumors, we obtained pure C3H/He p53-deficient mice by crossing p53-deficient C57BL mice back to C3H/He. C3H/He mice show a relatively high incidence of radiation-induced myeloid leukemia.

Bone marrow cells were harvested from p53 homo-deficient C311/IleNrsMs male mice, and  $1 \times 10^6$  cells were injected through a tail vein of the lethally irradiated mice (transplantation assay). The hematopoietic cells in these recipient mice were replaced with p53 homo-deficient cells within 4 weeks after transplantation; then, they were further exposed to whole-body irradiation at 1, 3, or 5 Gy. Large numbers of mice are required for studies of carcinogenesis, and the transplantation assay is a good tool to meet this need, because 40-50 mice can be uniformly repopulated with bone marrow from one p53 homo-deficient mouse. In addition, analysis of the function of p53 gene is limited to the hematopoietic tissue.

When mice with p53 deficiency were backcrossed into C311/Ile mice, there was a dramatic difference, with 77% developing undifferentiated leukemias compared with 22.2% with lymphomas. The leukemias were negative for either the T cell markers (Thy1.2 and CD3), or for the B cell markers (B220 and s-IgM), and also, for myeloid lineage cell markers (Mac-1 and Gr-1). The leukemia cells only expressed c-Kit and Pgpl. c-Kit is the receptor for the stem cell factor and it was expressed on almost all hematopoietic progenitor cells. Pgpl was positive for all bone-marrow cells at varying intensities; however, lymphoid cells appeared dull, CFU-s were intermediate, myeloid lineage-committed stem cells were brighter, and mature myeloid cells were very bright. Therefore, this undifferentiated leukemia seemed to be a stem cell leukemia with myeloid differentiation. These leukemic cells occasionally showed a minimum differentiation, with megakaryocytic, myeloblastic, and erythroblastic elements observed histologically in the leukemic infiltrate. Further, TER119 was positive in 35% of the cases when the enlarged splenic cells were examined.

By contrast, thymic lymphomas, the second most common malignancy in the p53 deficient C3H/He mice, appeared relatively later than the stem cell leukemias. Thymic lymphoma has rarely been seen in wild type C3H/He mice. Even with the same p53 deficiency, the incidence of the thymic lymphoma in the C3H/He mice was much less than in C57BL animals, probably because of the high incidence of myeloid prone tumors of the C3H/He mice.

We also found that radiation dramatically decreased the latency of leukemia in p53 homozygous deficient mice, and depended on the dose of radiation; the largest decrease in the 50% incidence, from 118 days to T4 days, appeared in the 5 Gy irradiated group.

---

## 26. Different Cellular Basis for the Resistance of C3H and STS Strain Mice to the Development of Thymic Lymphomas Following Fractionated Whole-body Irradiation: Analysis Using Radiation Bone Marrow Chimeras

**Hitoko Kamisaku, Shiro Aizawa, Kaoru Tanaka, Keiko Watanabe and Toshihiko Sado**

**Keywords:** *thymic lymphomas, strain difference, bone marrow transplantation*

B10 strain mice are susceptible to the induction of thymic lymphomas by fractionated whole-body X irradiation (FI), whereas C3H and STS mice are resistant. The nature of the factors responsible for the strain difference in the susceptibility to thymic lymphomagenesis was investigated by using radiation bone marrow chimeras. Radiation bone marrow chimeras were constructed in the reciprocal donor/host combinations of susceptible and resistant mice using Thy 1 markers that allow the genetic origins of thymocytes and thymic lymphomas to be determined. B10.Thy 1.1→C3H, B10.Thy 1.1→STS as well as B10.Thy 1.1→B10 bone marrow chimeras manifested a high incidence of thymic lymphomas after FI-treatment, whereas C3H.Thy 1.1→B10 and STS→B10.Thy 1.1 as well as C3H.Thy 1.1→C3H and STS→STS chimeras manifested a low incidence of thymic lymphomas. Furthermore, FI-treatment of [B10.Thy 1.1|C3H]→B10.Thy 1.1 mixed chimeras resulted in the generation of similar numbers of thymic lymphomas of B10 and C3H origins, whereas FI-treatment of [B10.Thy 1.1|STS]→B10.Thy 1.1 mixed chimeras preferentially induced thymic lymphomas of B10 origin. These results indicated that (1) genetic factors responsible for the strain-independent susceptibility and/or resistance to FI-induced lymphomagenesis exert their effects entirely on bone-marrow derived cells, (2) host environments of C3H and STS resistant mice are not inhibitory for the development of thymic lymphomas and (3) the resistance of STS mice to FI-induced thymic lymphomagenesis is an intrinsic property of thymocytes, whereas C3H and B10 thymocytes themselves are similarly susceptible for FI-induced thymic lymphomagenesis.

### **Publications:**

- 1) Kamisaku, H., Aizawa, S., Kitagawa, M., Ikarashi, Y. and Sado, T.: *Int. J. Radiat. Biol.*, 72, 191-199, 1997.
  - 2) Kubota, Y., Takahashi, S., Sun, H-Z., Sato, H., Aizawa, S. and Yoshida, K.: *Int. J. Radiat. Biol.* 76, 649-659, 2000.
  - 3) Kamisaku, H., Aizawa, S., Tanaka, K., Watanabe, K. and Sado, T.: *Int. J. Radiat. Biol.*, 76, 1105-1111, 2000.
-

## 27. Absence of Linkage between Radiosensitivity and the Predisposing Atp7b Gene Mutation for Heritable Hepatitis in the LEC Rat

Toshiaki Ogiu, Mayumi Nishmmura, Fumiaki Watanabe, Hideki Ukai, Hiroko Ishii-Ohba, Yoshiya Shimada, Hideo Tsuji, Junko Sakurai and Okio Hino

**Keywords:** LEC rats, radiosensitivity, X-rays, Atp7b gene, linkage analysis

The LEC rat is known to be a mutant strain that spontaneously develops heritable hepatitis due to copper accumulation, caused by mutation of the copper transporting ATPase gene (Atp7b). Immunodeficiency and radiosensitivity have also been observed. Hayashiet al. extensively examined the radiosensitivity of the LEC rat and concluded that its hypersensitivity is controlled by a single autosomal gene. Furthermore, they suggested the possibility that it correlates to copper accumulation due to the Atp7b gene mutattion, because ionizing radiation-induced hydroxyl radicals might act in concert with copper-induced hydroxyl radicals. In the present experiment, we analyzed linkage between radiosensitivity and the mutatnion responsible for LEC hepatitis in F<sub>1</sub> animals of cross with the F344 rat ([Table 4](#)). Our results clearly demonstrated an absence of any significant association. In addition, partial dominance for radiosensitivity was o bserved and radiosensitive (F<sub>1</sub> X LEC) backcross rats were twice as numerous as their radioresistant counterparts, suggesting the possibility of control by two or more recessnve genes.

Table 4. Number of [(F344xLEC) F1xLEC] backcross Rats with Each Combination of Radiosensitivity and Atp7b Genotype

Combination of Radiosensitivity and Atp7b genotype		Number of Rats
Radiosensitivity <sup>a</sup>	Atp7b genotype <sup>b</sup>	
Sensitive	LEC	36
	F344	45
Resistant	LEC	21
	F344	19

<sup>a</sup>Radiosensitivity was determined on the basis of the mortality at 30 days after whole body irradiation with 4.0 or 4.5Gy of X-rays.

<sup>b</sup>Genotype was determined by Southern blot analysis. LEC means LEC genotype and F344 genotype.

---

## 28. Effects of Orchidectomy on Bone Metabolism in Beagle Dogs

Satoshi Fukuda and Haruzo Iida

**Keywords:** canine, bone histomorphometry, iliac bone, orchidectomy

The effects of orchidectomy on bone metabolism in male beagle dogs were examined using twelve 2 year-old dogs that were orchidectomized. The bilateral iliac bones, double-labeled with tetracycline and calcein for the histomorphometry, were obtained from three dogs prior to orchidectomy and at 3, 6, 9 and 12 months afterwards. The serum biochemical constituents related to bone metabolism were examined before and every month after orchidectomy. Between 1 and 6 months after orchidectomy, the value of serum testosterone decreased (1 month) while the levels of parathyroid hormone, calcitonin, total calcium, osteocalcin, and alkaline phosphatase activity increased significantly, indicating a high bone turnover. The mean trabecular thickness and the fraction of labeled osteoid surface decreased significantly 3 months after orchidectomy, but other histomorphometric parameters were unchanged. In the period 7-12 months after orchidectomy, the parathyroid hormone level increased above that of the first 6-month period, while the levels of calcitonin, osteocalcin, alkaline phosphatase activity, and phosphorus decreased. The bone volume, mean trabecular thickness, and the fraction of labeled trabecular surface decreased significantly compared with the pre-orchidectomy values. These findings indicate an imbalance in bone metabolism (i.e. bone resorption > bone formation).

These results indicate that a loss of bone volume accompanied the fall in sex hormone levels following orchidectomy and suggest that the orchidectomized dog is available as an animal model for studying osteoporosis caused by hypogonadism and the decline of sex functions in male humans.

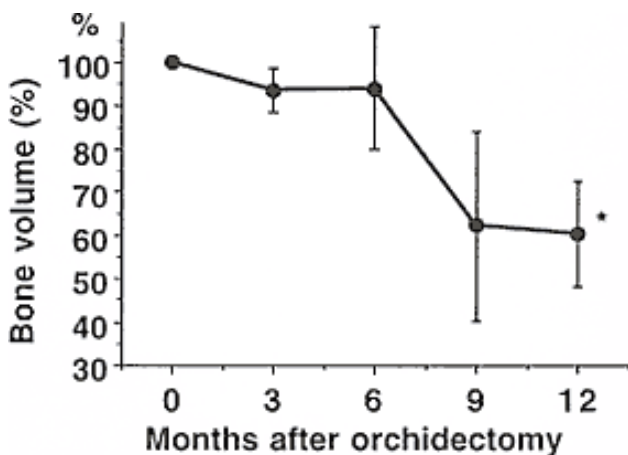


Fig.12. Decrease in bone (BV/TV) after orchidectomy, shown as percentages of the value before orchidectomy, shown as percentages of the values before orchidectomy in each group. There was a significant decrease in bone volume ( $p < 0.05$ ) at 12 months compared to the value before orchidectomy.

### Publication:

Fukuda, S., and Iida, H.: Jpn.Vet. Sci., 62, 69-73, 2000.

## 29. Sequence of 16S rRNA Gene of Rat Origin CAR Bacillus SMR Strain

**Akihiro Kawano Mitsuru NCIIIIOI, Satoru Matsushita, Tsuneya Matsumoto, Hiromi Takahashi-Omoe and Kazuei Mita**

**Keywords:** *CAR bacillus, sequence similarity, 16S rRNA gene.*

Cilia-associated respiratory (CAR) bacillus is an unclassified, gram-negative, filamentous bacterium that was tentatively designated in 1985 as one of the agents that cause chronic respiratory diseases in laboratory rodents. Recently, 16S rRNA gene analysis has indicated that the rat and mouse-origin CAR bacilli were most closely related to members of the Flavobacter/Flexibacter group, while the rabbit origin CAR bacilli were most closely related to members of the genus Helicobacter. In the present study, the 16S rRNA gene of the SMR strain of cilia associated respiratory (CAR) bacillus, which was isolated from a spontaneously infected rat at our institute, was sequenced, and its 1,521 nucleotides were determined. On the basis of the results of the homological analysis, it was revealed that the SMR strain was most closely related to *Flavobacterium ferrugineum* (83% similarity), *Chitinophaga pinensis* (83%), and *Flexibacter sancti* (81%) belonging to the Flavobacter/Flexibacter group. This result coincides with the previous taxonomic analysis of the rat and mouse-origin CAR bacillus. This sequence was compared with the previously determined 16S rRNA gene sequences (rat-origin: the CARB-NIH strain, the CBR strain and the R isolates; mouse-origin: the CBM strain; rabbit-origin: the 13 isolates) of CAR bacillus isolates. Between the SMR and the CARB-NIH strains, the sequence similarity was 99%. That is, only a single nucleotide was different among 1,489 overlapped nucleotides. Therefore, within the accuracy of sequencing technology, we conclude that these two strains, SMR and CARB-NIH, are genetically identical based on the analysis of the 16S rRNA gene. As a result of the comparison of the 16S rRNA gene sequences of the abovementioned rat and mouse-origin CAR bacillus strains, almost identical sequences were recognized from positions 269 to 454. In the 16S rRNA gene sequence, it is known that there are conserved regions and variable regions. The former regions are those that are fully conserved over the species and genera in eubacteria, while the latter regions differ between species. Accordingly, it is suggested that positions 269 to 454 are peculiar to the rat and mouse-origin CAR bacillus, and this region of the gene may therefore be useful in diagnosing rat and mouse-origin CAR bacillus infection by the PCR method.

### **Publication:**

Kawano A. Nenoj, M., Matsushita, S., Matsumoto T. and Mita, K.: *J. vet. med. sci.*, 62, 797-800, 2000

---

## 30. Effect of Deficiency of DNA-dependent Protein Kinase Catalytic Subunit on Mutational Properties in Cultured Mouse Mammary Tumor cells

**Yuko Hoki-Fujimori, Ryoko Araki, Ryutaro Fukumura, Akira Fujimori, Ikuko Furuno-Fukushi, Koki Sato Masumi Abe and Kouichi Tatsumi**

**Keywords:** adenine phosphoribosyltransferase (APRT) hypoxanthin phosphoribosyltransferase (HPRT), non homologous end joining (NHEJ), 8-aza-adenine (8AA)

DNA-dependent protein kinase (DNA-PK) composed of catalytic subunit (as), Ku70 and Ku86 is indispensable for repair of DNA double-strand breaks and V(D)J recombination. As it binds to DNA double-strand breaks and requires such structural alterations for its enzymatic activity, DNA-PK has been presumed as being one of the key molecules for sensing DNA damages. However, neither true in vivo substrates for the kinase activity nor the precise mechanisms for controlling the signal transduction triggered by DNA double-strand breaks have been clarified yet. Recently we have found that SX9, a radiosensitive subline of mouse mammary tumor FM3A cells, bears a T→C transition at 9572 of the Dna-pkcs gene that causes a Leu→Pro substitution at codon 3191 and results in a complete loss of the DNA-PKcs functions. The effect of total deprivation of DNA-PKcs on mutational properties was examined by comparing the mutabilities at the hemizygous X-linked Hprt focus and the autosomal Aprt focus between the null mutant SX9 cells and their parental SR-1 cells that are heterozygously inactivated at the Aprt gene (Aprt +/-). SX9 cells were approximately 4-fold more sensitive than SR-1 cells to X-ray cytotoxicity with the lost shoulder and the steeper slope in the survival curve. Spontaneous mutant fractions in SX9 cells were 4-fold ( $8 \times 10^{-4}$ ) and 9-fold ( $1.7 \times 10^{-4}$ ) higher than in SR1 cells for 8-azaadenine (8AA) resistance and 6-thio-guanine (6TG) resistance, respectively. While a statistically significant increase was induced by X-rays for 8AA resistant mutant fraction in both SX9 and SR-1 cells, 6TG resistant mutant fractions were clearly increased only in SR-1 cells. When increased mutant fractions were replotted against surviving fractions instead of exposure dose of X-rays, the hypomutability of SX9 cells for the two markers became conspicuous at least in the dose range allowing survival above 10%. The impairment of non-homologous end-joining of DNA double-strand breaks appeared to result in the hypomutability to X-rays by rendering cells with potentially mutagenic DNA insults more vulnerable to cell killing.

---

## 31. A Medaka Mutant, Oot(ONE-sided optic tectum), That Breaks Bilateral Symmetry of the Developing Brain

**Yuji Ishikawa**

**Keywords:** *mutation, brain, mutant, morphology anomaly, development, teleost fish, medaka*

A spontaneous viable maternal-effect mutation, Oot (One-sided optic tectum), was newly found in a population of the HO4C inbred strain of the medaka (*Oryzias latipes*). The mutant phenotype was observed at only restricted stages of the morphogenesis of the brain. The Oot phenotype is as follows: In a normal embryo, the hemilobes of the optic tectum (dorsal part of the midbrain) bulge out laterally, or evaginate, on both sides at early embryonic stages (at stages 23-25), forming a mirror symmetry along the midline axis; namely, the left hemilobe is a mirror image of the right hemilobe. However, in the mutant embryo at the same stages, only one of the hemilobes of the optic tectum evaginates, while the hemilobe on the other side does not evaginate but instead invaginates or bulges medially. The frequency ratio of the right/left directions of the expansion is 1/1 among sibling mutant embryos. Other body parts of the mutant embryo are completely normal without any associated situs inversus or unusual cardiac looping. Thus, in the Oot phenotype the mirror symmetry or bilateral symmetry is broken only in the developing optic tectum, and both hemilobes exhibit the same morphology on both sides. At stage 26, the invaginated optic tectum hemilobe starts to evaginate in the mutant embryo, and the optic lobes become normally symmetrical at later stages. The mutant fry hatch and grow almost normally. This kind of brain mutant has never been reported so far in other vertebrates including zebrafish. Thus, this is the first report to show that there exists a maternal gene that affects the bilaterally symmetrical evagination of the developing optic tectum.

### **Publications:**

- 1) Ishikawa Y.: *Bioessays*, 22, 487-495, 2000.
  - 2) Ishikawa, Y., Hyodo-Taguchi, Y., Aoki, K. Yasuda, T., Matsumoto, A. and Sasanuma, M. *Fish Biol. J. Medaka*, 10, 27-29, 1999.
  - 3) Ishikawa, Y., Yoshimoto, M. and Ito, II.: *Fish Biol. J. Medaka*, 10, 1-26, 1999.
-

## 32. Cloning of huNp95 : A Novel Human Homologue of Mouse Np95 Gene

Masahiro Muto, Yasuyoshi Kanaru, Eiko Kubo, Kouichi Tatsumu

**Keywords:** *novel nuclear protein Np95, human homologue, PCNA, DNA replication, cell cycle*

We previously produced a monoclonal antibody Th-10a mAb, that recognizes a 95 kDa mouse nuclear protein (Np95). Np95 was stained with the Th10a mAb specifically in the S-phase of normal mouse thymocytes. In contrast, mouse T cell lymphoma cells showed a constantly high level for Np95 accumulation irrespective of cell stages during the cell cycle. By immunoscreening a  $\lambda$ gt11 cDNA expression library with the Th-10a mAb, we isolated the cDNA encoding the mouse nuclear protein Np95. Sequencing of the whole 3.5 kb cDNA revealed that Np95 is a novel nuclear protein with an open reading frame (ORF) consisting of 782 amino acids. The ORF contains a leucine zipper motif, a zinc finger motif, a potential ATP/GTP binding site, a putative cyclin A/ E-cdk2 phosphorylation site and retinoblastoma protein (Rb) binding motifs "LXCXE" and "IXCXE". Np95 was strongly expressed in the testis, spleen and thymus, lung tissues, but not in the brain, liver and skeletal muscles. Microscopically Np95 appeared as foci in nuclei through late G1 to S phase of m5S cells, and these foci coincided with those for proliferating cell nuclear antigen (PCNA) in double immunostaining studies. These results collectively implicate this novel nuclear protein in cell cycle progression and/or DNA replication. In this study, to identify the human homologue of mouse Np95, we carried out sequence database searching using the Blast algorithm. A tblastn search of the Genbank database using the mouse Np95 amino acid sequences revealed that several EST clones with the accession numbers, AA811055, AA908902, AA306523, AA827671 and AA811217 have an amino acid sequence similarity with that of mouse Np95 in two parts. Using the sequence information, these cDNA fragments were amplified by PCR using 8 primers and a human testis cDNA library (GibcoBRL). Amplification of the 3' region was carried out by the two-step PCR procedure using the testis cDNA library. Since we could not amplify the 5' region, pMyr human testis cDNA library (Stratagene) and multiple testis cDNA (CH 1011; Origene technol. Inc.) were used to obtain the 5' region. We finally isolated a 3295-bp cDNA which contains a single large open reading frame encoding a polypeptide of 793 amino acids. We also isolated three other isoforms of the homologue cDNA. To investigate the localization on chromosome and the exon and intron of this gene, three bacterial artificial chromosome (BAC) clones which contain huNp95 gene were obtained by screening of BAC libraries of Roswell Park Cancer Institute and RPCI 11 human BAC library (Nihon Techno. Serv Japan).

### **Publication:**

Uemura, T., Kubo, E., Kanaru, Y., Ikemura, T., Tatsumi, K. and Muto, M.: Cell Structure and Function, 10, 149-159, 2000.

---

### 33. Nonsense Mutation at 124 in the XRCC4 of Radiosensitive Cell Line M10

Masahiko Mori, Hiromi Itsukaichn and Koki Sato\* (\*Kinki Univ.)

**Keywords:** DNA-double strand breaks repair, XRCC4 gene, potnt mutatton

The XRCC4 gene is required for the repair of DNA double-strand breaks in mammalian cells. Without XRCC4, cells are hypersensutuve to IOIIIZIIB radiation and deficient for V(D)J recombination. The mouse lymphoma L5178Y cell mutant MID is defective in DNA-double strand breaks repair and hypersensitive to ionizing radiation. The complemen tation test by expression of human XRCC4 cDNA in MID cells suggested that the MID cell line belongs to a x-ray cross complementing group 4 (XRCC4)

We isolated the open reading frame (ORF) of XRCC4 cDNA from MID and 1,5178Y cells and compared them at DNA sequence level. Consequently point mutation A to T (370) was discovered in XRCC4 cDNA of MID cells. l'he mutation is located in exon 4 and results in an arginine (124) to termination codon. To verify our findings, we assessed the mutation with genomic DNA prepared from L5178Y and MID cells, since substitution oc curring in MID created the restriction enzyme Nde I recognition site. Interestingly, analysis of genomic DNA revealed the presence of two kinds of chromosomes related to the mutated region in MID cells. One allele had the Nde I recognition site while the other did not. This means that the mutation took place in only one of two alleles. Indeed, only T peak appeared at nucleotide number 370 in the cDNA sequence pattern, while A and T peaks clearly appeared at the corresponding nucleotide in the genomic DNA sequence pattern. To analyze complementation of the radiosensitivity characteristic of MID cells the pME18S puromycin vector alone or pME18S murine XRCC4 cDNA was introduced into MID cells and stable transfectants were selected by use of the puromycin resistant marker. The clones were corrected for radiosensitivity similar to that of the wild type, L5178Y, levels. The clones formed transfections with pVIE18S vector alone which showed the radiosensitivity of MID cells.

```

                                370
L5178Y      nt. GAA GTC ATA AGA GAA CTC ATT
              a.a. Glu Val Ile Arg Glu Leu Ile
                                124
                                Nde I
M10         nt. GAA GTC ATA TGA GAA CTC ATT
              a.a. Glu Val Ile Ter * * *
```

Fig.13. Nonsense mutation in murine XRCC4 gene in M10 cells

## 34. Phosphorylation Sites of NPAT by CyclinE/ CDK2 Complex

Yasuharu Ninomiya, Kanae Hitomi\* Akiyo Nishiyama, Masashi Sagara, Yoichi Taya \*and Takashi Imai  
(\*Natl. Cancer Center Research Institute)

**Keywords:** NPAT, phosphorylation, cyclin/CDK

We identified a housekeeping gene, the NPAT gene which is located 0.5kb from the 5' end of the ATM gene. As these two genes share the same promoter region, there is a possibility that the NPAT gene is also related to ATM functions such as genome stability, cellular responses to DNA damage or cell cycle control. Recently, Dr. Zhao shows that NPAT is a substrate of cyclin/ CDK2 and NPAT plays a role in S-phase entry. To characterize the NPAT product in detail, we determined the modification sites of NPAT by cyclinE/CDK2. The only carboxylterminal region of the NPAT was obviously phosphorylated by cyclin/ CDK2 in vitro. We also found that other sites of NPAT were phosphorylated by other CDKs which were known to be active in S or G2/M phases of cell cycle. These results suggested that the NPAT functions at not only the G1 / S boundary, but also S and G2/M phases.

---

# 35. The Subcellular Localization and the Subcellular Translocation Mechanism of Ku70 and Ku80

**Manabu Koike, Aki Koike, and Tadahiro Shiomi**

**Keywords:** *Ku70, Ku80, DNA-PKcs, nuclear localization signal, cell cycle*

The Ku protein is a complex of two subunits, Ku70 and Ku80. Ku plays an important role in DNA-PKcs-dependent double-strand break repair and V(D)J recombination, and in growth regulation, which is DNA-PKcs-independent. We studied the expression and the subcellular localization of Ku and DNA PKcs throughout the cell cycle in several established human cell lines. Using immunofluorescence analysis and confocal laser scanning microscopy, we detected Ku70 and Ku80 in the nuclei in interphase cells. In mitotic cells (1) most of the Ku protein was found diffused in the cytoplasm, (2) a fraction was delocalized at the periphery of condensed chromosomes, and (3) no Ku protein was present in the chromosome interior.

Association of Ku with isolated chromosomes was also observed. On the other hand, DNA-PKcs was detected in the nucleus in interphase cells and not at the periphery of condensed chromosomes during mitosis. Our findings suggest that the localization of Ku at the periphery of metaphase chromosomes might be imperative for a novel function of Ku in the G2/M phase, which does not require DNA-PKcs.

Ku is generally believed to always form and function as heterodimers on the basis of in vitro observations. Here, we demonstrate that the localization of Ku80 does not completely coincide with that of Ku70. Ku70 and Ku80 were colocalized in the nucleus in the interphase but not in the late telophase/early G1 phase of the cell cycle. Since the in vivo function of Ku might be partially regulated by the control of its transport, we attempted to investigate the molecular mechanisms underlying the nuclear translocation of Ku. The nuclear translocation of Ku80 started during the late telophase/early G1 phase after the nuclear envelope was formed and this was preceded by the nuclear translocation of Ku70. Furthermore, we found that the Ku80 protein was transported to the nucleus without heterodimerization with Ku70. To understand in detail the mechanism of transport of Ku80, we attempted to identify the nuclear localization signal (NLS) of Ku80 and defined a region spanning nine amino acid residues (positions 561-569). The Ku80 NLS was demonstrated to be mediated to the nuclear rim by two components of PTAC58 and PTAC97. All these findings support the idea that Ku80 can translocate to the nucleus using its own NLS independent of the translocation of Ku70.

## **Publications:**

- 1) Koike, M., Ikuta, T., Miyasaka, T. and Shromt, T.: *Oncogene*, 18, 7495-7505, 1999.
  - 2) Koike, M., Awaji, T., Kataoka, M., Tsujimoto, G, K3rtasova, T., Koike, A. and Shiomi, T.: *J. Cell. S.*, 112, 4031- 4039, 1999.
  - 3) Koike, M., Ikuta, T., Miyasaka, T. and Shiomi, T., *Exp.Cell Res.*, 250, 401-413, 1999.
  - 4) Suzuki, T., Kurosaki, T., Shimada, K., Kansaku, N. Kuhnlein, U., Zadworny, D., Agata, K. Hashimoto, A., Koide, M., Koike, M., Takata, M. Kuroiwa, A., ]Iinai, S., Namikawa, T. and Matsuda Y.: *Cytogenet Cell Genet.*, 87, 32-40 1999.
-

## 36. Mammalian Cell Lines Expressing Functional RNA Polymerase II Tagged with the Green Fluorescent Protein

**Kimihiko Sugaya, Mare Vigneron<sup>1</sup> and Peter R. Cook<sup>2</sup>** (<sup>1</sup>Institut de Genetique et de Biologie Moleculaire et Cellulaire (CNRS/INSERM/ULP), France <sup>2</sup>The Sir William Dunn School of Pathology Oxford Univ. UK)

**Keywords:** *complementation, green fluorescent protein, RNA polymerase, mutant, transcription*

RNA polymerase II is a multi-subunit enzyme responsible for transcription of most eukaryotic genes. It associates with other complexes to form enormous multifunctional 'holoenzymes' involved in splicing and polyadenylation. We wished to study these different complexes in living cells, so we generated cell lines expressing the largest, catalytic, subunit of the polymerase tagged with the green fluorescent protein. The tagged enzyme complements a deficiency in tsTM4 cells that have a temperature-sensitive mutation in the largest subunit. Some of the tagged subunit is incorporated into engaged transcription complexes like the wild-type protein; it both resists extraction with sarkosyl and is hyperphosphorylated at its C-terminus. Remarkably, subunits bearing such a tag can be incorporated into the active enzyme, despite the size and complexity of the polymerizing complex. Therefore, these cells should prove useful in the analysis of the dynamics of transcription in living cells.



### **Publications:**

- 1) Sugaya, K., Vigneron, M. and Cook, P. R.: J. Cell. Sci., 113, 2679-2683, 2000.
  - 2) Pombo, A., Jones, E., Iborra, F. J., Kimura, H. Sugaya, K., Cook, P. R. and Jackson, D. A. Critical Reviews<sup>TM</sup> in Eukaryotic Gene Expression, 10 21-29 2000.
-

## 37. Bombyx EST Database, 'SilkBase', for Genome Analysis of Bombyx mori

Kazuei Mita, Mitsuoki Morimyo Yoshiko Koike<sup>1</sup>, Junko Nohata, Masataka Suzuki<sup>1</sup>, Kazuhiro Okano<sup>2</sup> Susumu Maeda<sup>2</sup> and Toru Shimada<sup>1</sup> (<sup>1</sup>Univ. of Tokyo; <sup>2</sup>RIKEN)

**Keywords:** *cDNA library, Bombyx mori, EST database, multi-cellular organism, BAC library*

Aiming at the genome analysis of Bombyx mori, we are constructing the EST database through the analysis of cDNA libraries. The gene expression patterns significantly depend on tissues as well as developmental stages in multi-cellular organisms, unlike the case of uni-cellular organisms such as yeast. The cDNAs from which the ESTs are derived are present in libraries in proportion to the level of mRNA in the tissues from which the libraries were prepared. Thus, ESTs are subject to 'expression bias' for multi-cellular organisms. Therefore, we took the following strategy: cDNA libraries of various tissues (and different stages) were constructed by the directional cloning method. 1,000 cDNA clones were chosen at random from each library and around 700-base nucleotide sequences from the 5' end of the cDNA were determined, followed by gene identification with a protein homology search in public protein databases. Random sequencing of approximately 1,000 cDNA clones is effective to configure the abundantly expressed genes in the tissue from which the cDNA library is constructed, and analyses of various tissues (and different stages) will provide a sufficient amount of ESTs for genome analysis. In addition, this approach explicitly represents the gene expression patterns of all genes identified. Another advantage of the cDNA catalog is to figure out all members of related genes and display the whole pathway that the cells (or tissues) employ.

So far we have determined over 20,000 cDNAs derived from 29 cDNA libraries and identified more than 7,600 independent ESTs which cover about 40% of the total genes of B. mori. All ESTs are compiled into 'SilkBase' at the WEB site <http://www.ab.a.u-tokyo.ac.jp/silkbase/>

Recently, we have succeeded in the construction of a high quality B. mori BAC library in collaboration with Dr. Pieter de Jong's group at Roswell Park Cancer Institute. Its average insertion size was estimated to be 168 kb with 1.1 times redundancy. The genome size of B. mori was estimated to be 530 Mb. If 6,200 independent ESTs are available, one BAC clone will have 2-3 EST markers on an average. Therefore, more than 6,200 independent ESTs are needed for the construction of BAC contigs. We proceeded the construction of BAC contigs by hybridization using independent ESTs as probes.

### Publications:

- 1) Mita, K., Morimyo, M., Okano, K., Shimada, T and Maeda, S.: RIKEN Review, 22, 63-67, 1999
  - 2) Lee, A. J., Hahn, Y., Yun, J. H., Mita, K. and Chung, J. H.: Biochim. Biophys. Acta 1491, 355-363, 2000
  - 3) Yoshiga, T., Okano, K., Mita, K., Shimada, T and Matsumoto, S.: Gene in press.
-

## 38. Genome Sequencing of *Schizosaccharomyces pombe* Chromosome III

Mitsuoki Morimyo, Kazuei Mita, Etsuko Hongo, Tomoyasu Higashi, Kimihiko Sugaya, Shuichi Hiraoka, Masahiro Ajimura, Go Kenu, Shunichi Sasanuma, Miyako Gotou, Takumi Era, Yukari Ito Yoshie Ishihara and Etsuko Shiroma

**Keywords:** *S. pombe*, cDNA, BAC clone, DNA sequencing

In a study of the structure and function of the housekeeping genes of eukaryotic cells, we chose *Schizosaccharomyces pombe* (*S. pombe*) as a model organism. It is assumed to have 6,000 genes and the genome size of 14 megabases (Mb) compared to 100,000 genes and 3,000 Mb for humans. In spite of the greater numbers for humans, *S. pombe* can be used as a model organism for humans, because its genes are similar to human genes which can be normally expressed in yeast, its housekeeping genes are considered to be conserved through eukaryotic evolution and many of its genes have introns which make cDNA sequences essential to determine physical organization of genes from the genomic DNA sequence.

Moreover, the functions of *S. pombe* genes are easily identified by disrupting the genes with homologous recombination.

We have analyzed 12,000 cDNA clones made by mRNA prepared from late log phase cells of *S. pombe* and identified over 2,500 genes (900 similar clones with known genes and 1800 newly found clones). Among the cDNA clones, 8,118 were deposited with the DDBJ and put on the WWW homepage of NIRS (<http://www.nirs.go.jp>). By using these cDNA clones mapped on the chromosome III of *S. pombe*, we started genome sequencing. We made a BAC contig map of chromosome III and selected a minimum set of 18 BAC clones covering the whole chromosome III. The BAC DNA was partially digested by an endonuclease followed by sedimentation in a sucrose gradient and DNA fragments ranging from 1 to 3 kb were recovered for a shotgun sequencing. We finished sequencing of all 18 BAC clones and determined DNA sequence of chromosome III except three gaps, the centromere and both chromosome ends carrying tandem repeats of rDNA region. We identified an ORF found in an assembled DNA sequence as a gene by a homology search in protein databases and our *S. pombe* cDNA database (<http://133.63.36.123>). On average, we found a gene without introns every 4 kb, which is about half the prediction. This is because about 50% genes are known to have introns. A systematic disruption of genes related to radiation sensitivity is in progress to identify their functions.

### Publications:

- 1) Morimyo, M., Hongo, E., Ajimura, M., Mita, K., Higashi, T., Sugaya, K., Inoue, H., Yamauchi, M., Tsuji, S., Saito, T., Ito, H., Sasanuma, S., Nohata, J., Kimura, T., Ishihara, Y., Hattori, A., Hayashi, A., Koike, Y., and Shiroma, E.: *lth tcnn*, 123, 1999
  - 2) Yasuhira, S., Morimyo, M., Yasui, A.: *J. Biol. Chem.* 274, 26822-26827, 1999.
-

## 39. Strain Differences in Carcinogenic and Hemopoietic Responses of Mice Following Injection of Plutonium Citrate

**Yoichi Oghiso and Yutaka Yamada**

**Keywords:** *osteosarcoma, lymphoma, hematology mouse strains,  $^{239}\text{Pu}$  citrate*

The carcinogenicity of injected  $^{239}\text{Pu}$  citrate was compared among C3H, C57BL/6 and BC3F<sub>1</sub> hybrid strains of female mice with different spontaneous or radiation-induced tumor spectra. Significant survival reduction due to early neoplastic death particularly caused by induction of osteosarcomas was noted in each strain after injection of 500 Bq or more. The dose response of osteosarcomas appeared to show mostly similar patterns in each strain, except for the differences in the skeletal dose ranges for the maximum induction. While the incidence of lymphoid tumors decreased as osteosarcomas sharply increased up to the maximum at higher doses, their histological phenotypes were predominantly non-thymic, pre-B-cell leukemia lymphomas as compared to the controls in each strain. Myeloid leukemias were rarely or not observed and solid tumors involving other organs were rather reduced in each strain after injection of 500 Bq or more.

To follow up the hematological kinetics related to alpha particle irradiation of bone marrow hemopoietic stem cells, sequential examinations were done in each strain of mice within one year after injection of 5000 Bq. The cellularities of peripheral white blood cells and bone marrow cells were persistently reduced in each strain from the early periods, while spleen cells increased from 180 days later. Granulocyte-macrophage and macrophage colony-forming cells (GM and M-CFC) were also persistently reduced in the bone marrow, but were compensatively increased in the spleen from the early periods. Neither myeloid nor lymphoid tumors were found in any strains of mice during one year after the injection.

These findings indicate carcinogenic and hemopoietic responses specific to alpha particle irradiation, but independent of mouse strains injected with  $^{239}\text{Pu}$  citrate.

### **Publications:**

Oghiso, Y. and Yamada, Y.: *Radiat. Res.*, 153, S27-S30 1999.

---

# 40. Chromosomal Aberrations Detected by Interphase Chromosome Painting in Lymphocytes from Cancer Patients Given X-ray or Carbon Ion Therapy

Shigeru Yamada<sup>1</sup>, Marco Durante<sup>2</sup>, Ryonfa Lee<sup>3</sup>, Takashi Nakano<sup>1</sup>, Koichi Ando<sup>3</sup> and Hirohiko Tsujii<sup>1</sup>; <sup>1</sup>Research Center of Charged Particle Therapy <sup>3</sup>International Space Radiation Laboratory National Institute of Radiological Sciences, Chiba, Japan, <sup>2</sup>Department of Physics, University Federico II, Italy

**Keywords:** chromosome aberration, carbon ion beam, clinical research

We measured chromosomal aberrations in peripheral blood lymphocytes from cancer patients treated with X-rays or carbon ions. Blood samples from patients diagnosed for esophageal or uterus cervix cancer were obtained before, during, and at the end of the radiation treatment. Patients with similar pathologies, tumor positions, and field sizes were compared in the present study. The novel technique of interphase chromosome painting was used to detect aberrations in prematurely condensed chromosomes 2 and 4. Fraction of aberrant lymphocytes was measured as a function of the tumor. The results demonstrate that carbon ions induce a lower level of cytogenetic damage in lymphocytes than X-rays.

A total of 40 patients being treated for different cancers at NIRS were involved in the study. Patients were treated either with carbon ions accelerated at the HIMAC or IOM/v X-rays produced in a LINAC Tumor pathology was squamous cell carcinoma for all patients, except for one melanoma of the esophagus inferior. Treatment planning with IOMV X-rays consisted of daily fractions of 1.6-2.0 Gy. Patients treated with carbon ions were exposed at the HIMAC, 290 or 350 MeV, 6-8 cm spread out Bragg peak (SOBP) Treatment planning was designed to deliver a uniform equivalent dose (in GyE) to the target volume. GyE was calculated as the product between physical dose distribution and RBE values for cell killing in each point along the SOBP. RBE values ranged from 2 to 3 along the SOBP. Daily fractions of 2.7-3.6 GyE were used.

Blood samples were obtained at different times before, during, and at the end of treatment. Pretreatment samples were exposed in vitro to X-rays (200 kVp) in the dose range 1-4 Gy at a dose rate of 1 Gy/min. PBL from 3 uterus cancer patients were also exposed in vitro to the 290 MeV carbon ion beam at a dose rate of approximately 5 Gy/min at 13 and 83 KeV/mm.

Lymphocytes were isolated from the whole-blood and stimulated to in vitro growth in medium supplemented with phytohemagglutinin. PCC was induced by calyculin A. Slides were hybridized in situ with whole-chromosome human DNA probes specific for chromosomes 2 and 4. Fraction of aberrant cells was calculated at the ratio between the number of spreads containing one or more aberrations involving chromosomes 2 and/or 4, and the total number of PBL scored (ranging from 200 to 2000).

The in vitro experimental data for X-rays were pooled from 11 different patients, while data for carbon ion beams are pooled from three different patients. No significant differences in the in vitro response of PBL from the different patients were detected.

Similarly, no significant difference was observed for PBL exposed in vitro to carbon ions at the HIMAC. Carbon ions were more efficient than X-rays in the induction of chromosomal aberrations in vitro. The RBE (evaluated at 15% aberrant cells, corresponding to an X-ray dose of 2 Gy) of carbon ions was 1.43 and 3.97 at 13 and 83 KeV/mm, respectively.

Eleven patients treated for cancer in esophagus inferior were examined as in the in vivo study Frequency of

chromosomal aberrations increased as a function of the number of fractions delivered to the target volume. The dose-response curves of the two X-ray patients had a similar shape, but one patient showed more damages than the other. The differences could be explained based on the X-ray field size difference, which was 140cm<sup>2</sup> for the patient displaying a higher frequency of chromosomal aberrations, and 84cm<sup>2</sup> for the other. The three carbon ion beams patients displayed similar response, although different field sizes were exposed (115, 108 and 61 cm<sup>2</sup>). The fraction of aberrant PBL was lower for two carbon ion beams patients as compared to X-ray patients.

For uterus cervical cancer the field size was around 200cm<sup>2</sup> for all patients. All patients treated with carbon ions presented a lower frequency of aberrant PBL than X-irradiated counterparts.

It was concluded that interphase chromosome painting (chemical induction of PCC combined with FISH) is a useful tool for monitoring patient response to X-rays or charged-particle cancer therapy. The fraction of complex type chromosomal exchanges correlates with acute toxicity in patients treated for esophageal cancer.

### **Publications:**

- 1) Yamada, S., Durante, M., Ando, K., Furusawa, Y., Kawata, T., Majima, H. and Ando, K. *CANCERLETTERS* 150 215-221 2000.
  - 2) Durante, M., Yamada, S., Ando, K., Furusawa, Y., Kawata, T., Majima, H., Nakano, T. and Tsujii, H. *Int. J. Radiation Oncology Biol. Phys.* 47, 793-798, 2000.
  - 3) Durante, M., Yamada, S., Ando, K., Furusawa, Y., Kawata, T., Majima, H., Nakano, T. and Tsujii, H. *Int. J. Radiation Oncology Biol. Phys.* 44, 1289-1298, 1999.
  - 4) Durante, M., Kawata, T., Nakano, T. and Yamada, S. *Int. J. Radiation Oncology Biol. Phys.* 22, 1653-1662, 1998.
-

## 41. The Phase I & II Clinical Study of Carbon Ion Therapy for Cancer of the Uterine Cervix

**Takashi Nakano,M.O., Michiya Suzuki,M.D Atsuko Abe,M.O., Yoshiyuki Suzuki,M.O Shinroku Morita,M.D., Junetsu Mizoe,M.O Shinichiro Sato , PhD . , M . D Tadaaki Miyamoto,M.O., Tadashi Kamada,M.D Hirotooshi Kato,M.D., and Hirohiko Tsujii,M.O**

**Keywords:** *clinical trial, carbon ion beam, heavy ion therapy, cervical cancer, radiation therapy, prognosis, local control, radiation response*

The phase I&II clinical study of carbon ion beam therapy was undertaken for 31 advanced cervical cancers of stages 3B and 4A from June 1995 to November 1997. The main purposes were to determine clinically taseful fraction dose without severe acute reaction of normal tissues and to assess tumor control dose levels achievable without significant normal tissue toxicity.

The treatment consisted of four fractions per week, 24 fractions over 6 weeks and was initiated with a fraction dose of 2.2 GyE which increased as 2.4 GyE, 2.6 GyE, 2.8 GyE, and 3.0 GyE. Consequently the total dose was initiated with 52.8 GyE, increasing up to

72.0 GyE by 4.8 GyE steps in dose escala tion fashion. Thirty patients with eligible advanced cervical cancers, i.e. 27 squamous cell carcinomas and three adenocarcinomas, were analyzed.

Acute response of normal tissues was less than photon treatment until fraction doses of 2.8 GyE and patients finished their treatment under comfortable conditions. Severe late complication occurred in two patients who received more than 67.2 GyE. The 2 year cumulative survival rate and local control rate of 27 patients with squamous cell carcinomas were 61.5 % and 59.3 %, respectively. According to stages, the 2-year survival rates of stages 3B and 4A patients were 54.4 %, and 75.0 %, respectively. The 2-year-local control rates of stages 3B and 4A patients were 52.6 %, and 75.0 %, respectively.

These results indicated that the disease control seemed to be relatively better for very advanced disease and dose escalation treatment. Local control was not significantly correlated with total dose and tumor volume. The present study, in spite of its small numbers and short observation period, suggested that adequate fraction dose for pelvis fields in 2.8-3.0 GyE and carbon ion beam therapy might be of advantage for advanced cervical cancer.

---

## 42. Serum CYFRA 12-1 in Cervical Cancer Patients Treated with Radiation Therapy

**Yoshiyuki Suzuki,M.D., Takashi Nakano,]VI.D Tatsuya Ohno,M.O., Atsuko Abe,M.O Shinroku Morita,M.D., and Hirohiko Tsujii,M.D**

**Keywords:** *radiation therapy, cervical cancer*

A fragment of cytokeratin 19, referred to as CYFRA 21-1 is abundant in serum of many patients with malignant tumors and it is recognized as a tumor marker, especially for non-small cell lung cancer. In this study, clinical usefulness of CYFRA 21 1 was investigated in cervical cancer patients treated with radiation therapy, with reference to squamous cell carcinoma related antigen (SCC-Ag) which is a common tumor marker for cervical squamous cell carcinoma.

The serum levels of CYFRA 21-1 and SCC-Ag were measured for 50 patients with squamous cell carcinoma of the uterine cervix before and after treatment their radiation treatment. The percentage of abnormal level of CYFRA 21-1 was 52 %. The incidence increased with stage advancement. The increase in the level of the patients after treatment was a sign of the disease progression. During radiation, serum level of CYFRA 21-1 decreased significantly for patients who had obtained local control and the level reflected the radiation effect well.

Additionally, CYFRA 21-1 was negative in all patients without distant metastasis at the end of radiation therapy. Compared with SCC-Ag, the positivity of CYFRA 21-1 was statistically lower. As for a correlation between the levels of CYFRA 21-1 and SCC-Ag, there was a statistically positive correlation (correlation matrix=0.69). These results indicated that CYFRA 21-1 can play an important role in monitoring outcome of patients with squamous cell carcinoma of the uterine cervix. The usefulness may be significant for patients without SCC-Ag.

---

## 43. Progesterone Receptor Is Favorable Prognostic Factor of Radiation Therapy for Adenocarcinoma of the Uterine Cervix

**Yoshiyuki Suzuki,M.D., Takashi Nakano,M.D Atsuko Abe,M.O., Shinroku Morita,M.D Hirohiko Tsujii,M.D., and Kuniyuki Oka,M.O**

**Keywords:** *adenocarcinoma, radiation therapy*

The prognostic significance of the expression of estrogen receptors (ER) and progesterone receptors (PgR) in adenocarcinoma of the uterine cervix has been controversial. Hence, the relationship between the expression of the hormone receptors and clinical outcome was evaluated for patients with adenocarcinoma treated with radiation therapy alone. This study involved 66 patients with cervical adenocarcinoma consisting of 44 adenocarcinomas and 22 adenosquamous cell carcinomas. They received radiation therapy at the NIRS Hospital between 1962 and 1993. The mean age of the patients was  $62.0 \pm 12.0$  years (range, 36-82 years). The numbers of patients with stage I, II, III and IV diseases were 7, 17, 27, and 15, respectively. Their ER and PgR statuses were investigated immunohistochemically for biopsy specimens excised from the cervical tumors before radiation therapy.

ER staining was positive in 12 patients (19%). ER status did not correlate with the 5-year cause specific, local control, and disease free survivals. PgR staining was positive in 12 patients (19%). The disease-free survival rate of PgR positive patients was significantly higher than that of PgR negative patients ( $p=0.044$ ). Although PgR status did not reach statistical significance in relation to the 5-year cause specific survival and local control, the better survival was due to less local recurrence rather than distant metastasis. The present study suggested that PgR status was associated with prognosis after radiation therapy for adenocarcinoma of the uterine

---

## 44. Clinical Trial Research on Radiotherapy for Cervical Cancer in the Asian Regional Cooperation Project

**Takashi Nakano,M.D., Hirohiko Tsujit,M.D Shinroku Morita,M.O., Atsuko Abe M.O Kunio SakashitaM.D. Hiroshi Sato Shinichiro Sato,Ph.D.,M.O and Sakata suhou,M.O**

**Keywords:** *cervical cancer, radiation therapy, cooperative research*

This research is a promotion of medical applications of radiation and radioisotopes supported by the Japan Atomic Energy Agency. Cervical cancer was targeted as it is one of the most frequent cancers observed in Asian countries. Treatment for patients is by radiotherapy, based on the unified-standardized treatment policy. The project aims at improving radiotherapy for cervical cancer throughout Asian countries through evaluating the treatment results in the international cooperative clinical trial. An international meeting was held at Suzhou Medical College Affiliated Hospital, Suzhou, China, in December 1999. The status of cervical cancer and the standard protocol pilot study were described at the meeting as follows:

1. 219 patients were registered as a pilot study which was tentatively analyzed. The 3-year survival rate of 60.3% and the local control rate of 83.7% were obtained.
2. Accelerated Hyperfractionation Radiotherapy NIRS and other participating countries reported on preliminary treatment results of Accelerated Hyperfractionation Radiotherapy for cervical cancer. Practical and reasonable treatment methods were discussed and the final treatment protocol was prepared.
3. Making Standard Treatment Protocol of radiation therapy for cervical cancer in Asian countries The Standard Treatment Procedure for cervical cancer was discussed and results of the last 6 seminars from 1993 were put on record. It was decided to edit booklets on the protocol and treatment results.
4. Education Lecture : Education lectures for medical students and related doctors were held for the first time. Three committees gave highly regarded lectures on brachytherapy, heavy particle radiotherapy, and the introduction to medical treatment at Saitama Cancer Center.

The following comments are made on the project.

1. The cooperative research has progressed successfully, and reached the stage to submit results to international journals. The accumulated knowledge should be spread into the participating countries and also in our own institute.
  2. We adopted the start of another international research theme for regional cooperation, which is Accelerated Hyperfractionation Radiotherapy
  3. We confirmed that it is meaningful to visit regional facilities where and when seminars are held in order to see the actual conditions and needs of the facilities in terms of practicing radiation therapy in regional countries.
  4. Our new type of technical cooperation, or technology transfer by means of software, is attracting a great deal of attention for our project aims at producing results not only by a surveillance study but also by this type of collaboration.
-

## 45. Functional Diagnosis and Evaluation of Therapeutic Effects for Cancer using PET

**Kyosan Yoshikawa, Katsumi Tamura, Yasunori Imai, Noriyo Matsuno Masahisa Koga, Masakuni Kanai, Susumu Kandatsu, Hirohiko Tsujii, Tetsuya Suhara, Katsuya Yoshida, Kazutoshi Suzuki, Osamu Inoue, Fumio Shishido and Hiroshi Fukuda**

**Keywords:** *positron emission tomography, heavy ion beam therapy, therapeutic effects*

Positron emission tomography (PET) can demonstrate increased metabolic demand as visual images, and it provides alternative information for diagnosis which can be used to complement morphological observations. We have showed the usefulness of PET with  $^{11}\text{C}$ -methionine for the diagnosis of Nymph node metastases in patients with lung cancer. This time, we evaluated the relationship between the tendency for Nymph node metastases to appear after heavy ion beam therapy and  $^{11}\text{C}$ -methionine PET diagnosis before and/ or soon after heavy ion beam therapy in patients with lung cancer. We selected 53 patients, with stage I non-small cell lung cancer, which were observed more than 1 year after heavy ion beam therapy. Eleven patients in our cases showed Nymph node metastases after irradiation. Mean term from the end of irradiation to the final diagnosis of Nymph node metastases was seven months. Some cases showed somewhat or considerably high methionine accumulation by PET before and/ or soon after heavy ion beam therapy. PET diagnosis seemed to be useful for selecting patients who need strict follow up for Nymph node metastases. Precise follow up, early detection of Nymph node metastasis and adequate therapy for the metastatic lesion seemed to improve prognosis of lung cancer patients.

We studied the usefulness of methionine PET for the evaluation of esophageal cancer. We checked mainly these three points: (1) how much methionine accumulates in non-treated esophageal cancer, (2) the role of PET in the evaluation of therapeutic effects, and (3) the relation between appearance of distant metastasis after therapy and methionine PET findings before treatment. Methionine PET tended to show high accumulation in non-treated esophageal cancer and mean TMR was 5.99 (from 1.93 to 11.7) When we evaluated the therapeutic effect using PET by change of methionine accumulation between preirradiation and postirradiation, it was important that the tumor shows a high accumulation of methionine (more than 5.0 TMR) before irradiation. If TMR of esophageal cancer lesion was higher than 5.0 at pretreatment and TMR was reduced to less than 3.5 at post treatment, we could evaluate the benefit of the treatment. Cases which showed very high methionine accumulation at preirradiation, TMR > 8, showed high distant metastases late at 83%. Other cases, with intermediate or less methionine accumulation, showed low distant metastases late at 0%. We thought that the high level of methionine accumulation in esophageal cancer at pretreatment might indicate high risk of distant metastasis possibility.

---

## 46. Clinical Application of Autoactivation PET Imaging Derived from C-12 Ion Radiotherapy

**Kyosan Yoshikawa, Takehiro Tomitani, Mitsutaka Kanazawa, Tatsuaki Kanan, Masahiro Endo, Katsumi Tamura, Masahisa Koga, Hirotohi Kato, Susumu Kandatsu, Junetsu Mizoe, Hirotohi Tsujii, Katsuya Yoshida, Kazutoshi Suzuki, Fumio Shishido and Hiroshi Fukuda.**

**Keywords:** *positron emission tomography, C-12 ion radiotherapy, autoactivation imaging*

Clinical application of PET imaging of autoactivation derived from C-12 ion radiotherapy was studied. We introduced the patient fixation system for auto activation PET measurements. Using this fixation system, we can get PET images with the same patient positioning as with patient positioning of HIMAC therapy planning CT. It is very important to perform the PET measurements under exactly same patient positioning as HIMAC therapy to compare RI distributions. We performed a phantom simulation study to get parameters for making superimposed images of PET and CT planning. We used two phantoms, one was a cylinder phantom which contains  $^{68}\text{Ge}$ - $^{68}\text{Ga}$  RI sources, i.e. a hot phantom and the other was a cylinder phantom which contains water, i.e. a cool phantom. The two phantoms were the same size and shape. We carried out therapy planning for this cool phantom in the same manner as usually used for patient treatment. CT planning was obtained using cool phantom. For PET measurements, the hot phantom was used. We got two sets of image data, PET images and planning CT images. We discussed adjustment of (a) the base line of the two image sets, (b) the amount of the slice gap, (c) the size of images in the X-Y plane, and (d) the position of each slice in the Z axis. We have gotten basic data for clinical applications from this simulation study.

---

## 47. Diagnosis-Dynamic Characteristic Model

**Toru Matsumoto, Akira Furukawa, Koji Suwa\*, Nobuo Fukuda (\*School of Dentistry at Tokyo, Nippon Dental University)**

**Keywords:** *image perception, decision-making model, search time, confidence rating*

A study was undertaken to construct a descriptive model for both the facilitation of an abnormality detection and the effect of search time on perception. In this study, we propose a model named the diagnosis-dynamic characteristic model (DDC). An outline of the model is as follows. Generally when medical doctors read an image and decide a "normal" or "abnormal" or "intermediate confidence level", they require some time to search the image. In this model, it is supposed that the time required for searching an image depends on several factors of image quality, skill of the reader, facilitation of diagnosis of an image and preconception before reading. Then psychological conflicts thinking "normal or abnormal" take place in the brain due to these factors, therefore, searching time is required. A mathematical formulation was made by incorporating these factors and it was fitted to the time(t) abnormal confidence level(p) data based on experiments.

To demonstrate the hypothesis derived from the DDC model, the model was applied to the oral CT image reading. A group of 20 oral CT images was carefully selected, which was comprised of 10 cases with abnormalities and 10 cases of non-lesion. Their image quality were worsened by a thinned-out operation of pixels of the image matrix. Four groups (20 images/group) of different image quality which depended on the degree of the thinned-out operation were generated in addition to the 20 originals. In the 20 CT images, 8 subjects searched for tumors. Eye movement data of subjects were measured by means of an eye tracking system. The length of time taken for each observation from beginning of image reading until the decision-making, was calculated from the value of time accompanying eye-movement data. Moreover, after an image reading, each subject answered a confidence rating score of abnormality (with 4 steps) which was used to construct an ROC curve.

Results applied for the DDC model analysis for these experimental data showed that the model explains the relation between search time and confidence level (Fig.14). That is, the confidence level (p) derived from the DDC model which exhibits the probability of abnormality varies non-linearly as the function of search time(t) of an image and the position of preconception which a subject had about a preconceived "normal" or "abnormal" at the start of diagnosis.

Finally, we confirmed that ordinal category scores of equal interval asked for the purpose of the ROC analysis (in Fig.14, they are 1, 2, 3 or 4) are equivalent to integrate the continuous confidence level obtained from the DDC model for each observation of each subject. If search time measured at each observation and the DDC model is applied, although a judgement of subject is zero or one ("normal" or "abnormal"), we can compose the ROC curve by using continuously-distributed probability of the DDC model.

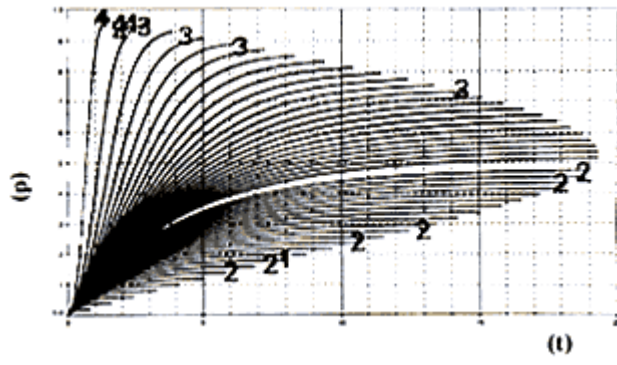


Fig.14. A sample of the relationship between search time (t) and confidence rating (p) obtained by a fitting of the DDC model.

---

## 48. Comparison of Stable Cesium and Radiocesium on Dietary Intakes in Japanese Subjects Using 18 Food Categories

**Kunio Shiraishi, Tadaaki Ban-nai, Yasuyuki Muramastu and Masayoshi Yamamoto\* (\*Kanazawa Univ.)**

**Keywords:** dietary intakes,  $^{137}\text{Cs}$ , Cs, Japanese, market basket study

The assessment of radiation doses in humans from man-made sources is important because artificial radiation is the largest contributor to committed internal doses in a nuclear emergency. Dietary intake of radioactive Cs has been studied since nuclear weapons testing began. Although analyses of many kinds of foodstuffs have been started, most results for Japanese subjects were obtained for total diet samples by duplicate portion studies. Furthermore, information on dietary element intakes is important from the viewpoints of not only radiation protection, but also public hygiene and nutrition. It is also of interest to know the relationships for both radioactive and non-radioactive nuclides in food chains. Recently, inductively coupled plasma mass spectrometry (ICP-MS) has become a valuable instrumental method for trace element detection because of its wide dynamic range and capability for multi element analyses. In this report, stable Cs in 18 food categories was determined using a market basket study to clarify the food pathways of  $^{137}\text{Cs}$  in Japanese subjects.

Three hundred and thirty-six foodstuffs were purchased from markets during 1994-1995. Total fresh weight treated was about 120 kg. Statistical consumption data of 1989-1991 (The Report of National Nutrition Survey) was used for collection of the food samples. Food categories are shown in Fig 15. The 18 categories were: 1) rice; 2) cereals, excluding rice; 3) nuts and seeds; 4) potatoes; 5) sugars and confectioneries; 6) fats and oils; 7) bean products; 8) fruits; 9) green vegetables; 10) other vegetables; 11) mushrooms; 12) seaweeds; 13) seasonings and beverages; 14) fishes and shellfishes; 15) meats; 16) eggs; 17) milk and milk products; and 18) cooked meals. Each food group was homogenized and freeze-dried. The obtained dry matter (approximately 500g) was incinerated in a muffle furnace at a final temperature of 400 °C. Most of the ashed parts obtained were first used for  $\gamma$ -ray measurements using a Ge-detector coupled to a multichannel analyzer. A 0.25g aliquot of ash sample was digested repeatedly with a mixture of nitric acid, perchloric acid, and hydrofluoric acid. Stable Cs was determined by ICP-MS.

The Cs concentrations in the 18 food categories were found range from 0.123 to 35.9ng per g-fresh. Five food categories, i.e. mushrooms (35.9ng), nuts and seeds (33.6ng), meats (26.8ng), fishes and shellfishes (21.6ng), and potatoes (19.2ng), were remarkably higher compared with other food groups. The groups of low Cs concentration were fats and oils (0.123ng) and rice (0.737ng). The total daily Cs intake ( $9.12 \pm 0.11 \mu\text{g}$  per person) was estimated from the daily intakes of the 18 food categories.

$^{137}\text{Cs}$  concentrations (mBq per kg-fresh) of the 18 food categories are shown in Fig 15. They were in the range of 0.022 (non-detectable; N.O.) and 1.7 Bq per kg-fresh. One category, mushrooms, as the highest at 1.7 Bq, was significant among the food groups. The next highest groups were nuts and seeds (0.23Bq), fishes and shellfishes (0.16Bq), meats (0.13Bq), potatoes (0.11Bq), and seaweeds (0.092Bq). The groups with low  $^{137}\text{Cs}$  contents were rice (<0.02Bq), fruits (<0.02Bq), green vegetables (<0.03 Bq), seasonings and beverages (<0.04 Bq) and other vegetables (<0.05 Bq). The total daily  $^{137}\text{Cs}$  intake (<0.10 Bq per person) was estimated from the daily intakes of the 18 food categories. The total of the values, excluding n.o. values, was 0.061 Bq per person.

In conclusion, daily Cs and  $^{137}\text{Cs}$  intake for Japanese were estimated to be 9.1 ng and 61mBq per person using

a market basket study, respectively Mushrooms, fishes and shellfishes, milk and milk products, meats, potatoes, and nuts and seeds were found to be key food categories of Cs and  $^{137}\text{Cs}$  intake in Japanese. Dietary intake studies by using eighteen or more food categories should be an effective procedure to resolve critical foods and critical pathways for Japanese. Critical pathways of radionuclides could be estimated more effectively by the analyses of stable isotopes using highly sensitive analytical methods.

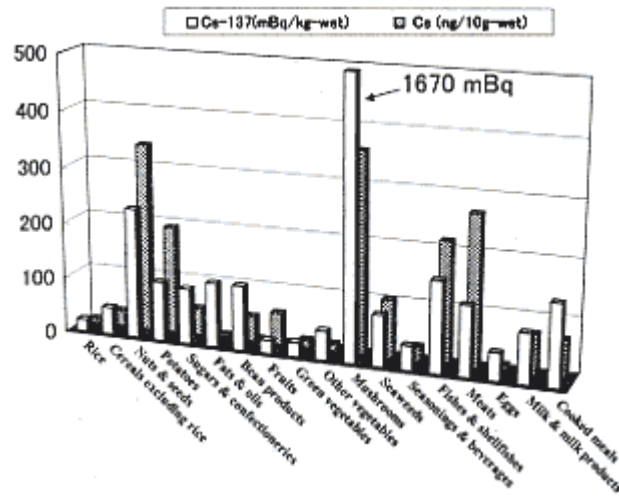


Fig.15. Comparison of concentrations between  $^{137}\text{Cs}$  and stable Cs in 18 categories for Japanese.

**Publication:**

Shiraishi, K., Ban-nai, T., Muramastu, Y. and Yamamoto M.: J. Radioanal. Nucl. Chem. 242, 687 692 1999.

## 49. Radiation Effects on Growth and Seed Germination of Arabidopsis

Yoshito Watanabe, Masae Yukawa, Kim Hee-Sun and Yoshikazu Nishimura

**Keywords:** environmental protection, plants, arabidopsis, germination

With the increasing interest about the impact of human activities on the ecology, environmental protection against ionizing radiation is getting attention. There is, however, only limited information about radiation effects on environmental organisms such as plants. In field studies of a nuclear accident, deleterious effects such as poor growth and genetic damages were observed in plants after a large dose of irradiation. On the other hand, some reports have shown that a low dose of irradiation could stimulate plant growth. In this study, we used a biological model plant, arabidopsis, to elucidate the radiation effects on plants.

The seeds of arabidopsis (var. Columbia) were surface sterilized and soaked in water at 4 °C for 2 days, before being cultured on the medium containing 0.8% agar under light in a controlled environment chamber. The plants were irradiated with X rays (0.5 20 Gy, 1 Gy/min) or gamma rays (50 Gy 1000 Gy, 10 Gy/min) at various growth stages. When young plant seedlings were irradiated, their root elongation was inhibited at doses more than 100 Gy, although elongation of the hypocotyls was not affected even at 1000 Gy. This indicates that the inhibition of growth by a high dose of irradiation varies with tissues, and the root is relatively sensitive to irradiation.

Irradiation of seeds did not affect their germination when they were cultured at the cultural temperature of 23 °C. However, when the seeds were cultured at 8 °C which is almost the lower limit for germination, the irradiated seeds germinated faster than the non-irradiated seeds. The effect of seed irradiation could be observed at a dose as low as 0.5 Gy. The acceleration of germination by seed irradiation was observed not only under the chilling stress, but also under the stress induced by a chemical agent. When seeds were grown at 23 °C on medium containing methyl viologen, a biological radical generator, pre-irradiation of seeds reduced the methyl viologen-induced retardation of germination (Fig 16). This suggests that irradiation of seeds could enhance anti-oxidant systems that enable seeds to germinate promptly under stress.

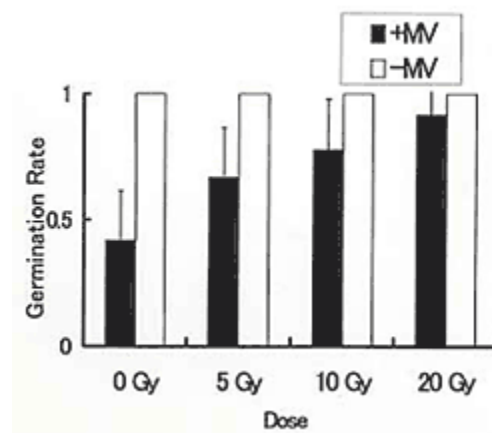


Fig.16. Reduction of methyl viologen (MV) - induced retardation of seed germination by X-ray pretreatment.

## 50. Cancer Mortality among Radiological Technologists in Japan: Updated Analysis of Follow-up Data from 1969 to 1993

**Shinji Yoshinaga, Takahashi Aoyama, Yasuhiko Yoshimoto, and Tsutomu Sugahara**

**Keywords:** *radiation, cancer mortality, radiological technologists, healthy worker effect, standardized mortality ratio*

A retrospective cohort study was conducted for 12,195 male radiological technologists who received occupational exposure to low dose radiation over a long term. A total of 1,097 deaths including 435 from cancer were ascertained by Koseki and by death certificates from 1969 to 1993. Cancer mortality among the study population was basically compared with that of all Japanese men. Significant low SMRs were obtained for all cancers, stomach and lung cancer partly due to the Healthy Worker Effect, unlike the results of the earlier reports with some inappropriateness in the methods. Apparent high risks of lymphatic and hematopoietic cancers were observed, although none of the site-specific cancers revealed a statistically significant increase. For these cancers, the SMRs of old sub-cohort were somewhat higher than those of young sub-cohort, whereas similar SMRs for solid cancer were obtained between the two sub-cohorts. The SMR for leukemia reached a statistically significant level of 1.75 (95%CI: 1.07-2.71) when all whole professional and technical workers as a standard population. The study results seem to suggest that the chronic exposure to low-dose radiation enhanced the risk of lymphatic and hematopoietic cancers.

### **Publication:**

Yoshinaga, S., Aoyama, T., Yoshimoto, Y., and Sugahara, T. : *Journal of Epidemiology*, 9, 61-72 1999.

---

# 51. Determination of U and Th in Soil and Plants Obtained from High Natural Radiation Area in China Using ICP-MS

Masae Yukawa, Yoshito Watanabe, Yoshikazu Nishimura, Yicao Guo, Yongru Zha Hui-min Lu, Wei Zhang, Luxin Wei and Zufan Tao

**Keywords:** *U, Th, daily dietary intake, high natural radiation, internal dose, annual effective dose*

There are high natural radiation areas of China, where the high radiation is caused by  $^{238}\text{U}$ ,  $^{232}\text{Th}$  and their decay products that are present in soil at higher levels than elsewhere. Area inhabitants ingest these nuclides through food grown in the soil. The internal radiation doses of these radionuclides have not been sufficiently evaluated. We collected soil and foods in a high natural radiation area (High Background Radiation Area: HBRA) and a control area (CA) in Guangdong Province of China in summer 1997 and winter 1998, and determined U and Th in the samples using ICP-MS (Inductively Coupled Plasma Mass Spectrometry)

Three hamlets from HBRA and one hamlet from CA were selected as sampling areas, and three families from each hamlet were chosen for this study. We interviewed the heads of the selected families in each hamlet concerning their eating habits to get information about the food consumption of one person in the hamlets. In all hamlets, the major food is rice and the second one is sweet potato. The main vegetable is water spinach in summer and cabbage in winter. Soil samples from rice and sweet potato fields, and summer vegetables, cereals and drinking water in each family were collected for the analysis in 1997. Total diet samples and winter vegetables were obtained in 1998 from the same families as the summer 1997.

About 20mg of dried soil was digested with a mixture of ultra-pure nitric acid, hydrogen peroxide and hydrofluoric acid using a microwave digester. Elemental concentrations in the solution were determined by ICP-MS. U and Th in plants were also determined by ICP-IVYS in almost the same way as in soils. Sample weights of dried leaf and rice grain were about 100mg and 1g, respectively. In the case of animal food, about 200mg of the ash were used for ICP-MS analysis to determine U and Th. We checked accuracy and precision of the results by analyzing standard reference materials, repeating the analysis and comparing to the results of INAA (Instrumental Neutron Activation Analysis) and  $\gamma$  spectrometry. The accuracy and precision of ICP-MS are good enough for the determination of U and Th in soil and food samples obtained from HBRA and CA.

[Table 5](#) shows the concentrations of U and Th in major plant food and some animal meat with their daily consumption in HBRA and CA. The daily dietary intake of the element shown in the table was calculated by summing up the products of concentration of the element in each food and the daily consumption. The effective dose coefficients of  $^{232}\text{Th}$  and  $^{238}\text{U}$  are given as  $0.22\ \mu\text{Sv/Bq}$  and  $0.044\ \mu\text{Sv/Bq}$  respectively in ICRP68. The annual effective doses derived from these data are  $0.302\ \text{p Sv/y}$  for  $^{238}\text{U}$  and  $1.86\ \text{p Sv/y}$  for  $^{232}\text{Th}$  in average in HBRA, and  $0.0101\ \text{p Sv/y}$  for  $^{238}\text{U}$  and  $0.177\ \mu\text{Sv/y}$  for  $^{232}\text{Th}$  in CA. An earlier study reported that the whole annual effective dose is  $2.1\ \text{mSv/y}$  in HBRA and  $0.68\ \text{mSv/y}$  in CA. The contribution rate of internal dose from these two radionuclides ingested into the human body is approximately 0.1% in HBRA and less than 0.1% in CA.

Table 5. Concentrations of Th and U in in Food Group and Their Daily Intakes

Th	Hamlet-1	Concentration(ppb)		D.D.I microg	Hamlet-2	Concentration(ppb)		D.D.I microg	Hamlet-3	Concentration(ppb)		D.D.I microg	Hamlet-CA	Concentration(ppb)		D.D.I microg
	D.C.(g/p/b)	Average	S.D.		D.C.(g/p/b)	Average	S.D.		D.C.(g/p/b)	Average	S.D.		D.C.(g/p/b)	Average	S.D.	
Rice Grain	500	4.12	5.5	2.06	650	2.04	2.35	1.32	750	0.461	0.510	0.346	600	0.255	0.046	0.119
Water Sp.	94.6	11.8	7.7	1.12	500	11	9	5	500	13	3	6.43	200	1.84	1.53	0.483
Cabbage	214	□@	□@	□@	200	□@	□@	□@	500	□@	□@	0.00	300	□@	□@	□@
Sweet Po.	37.5	0.169	□@	0.00636	200	3.43	5.54	0.685	500	□@	□@	0	68.5	0.386	□@	0.0265
Fish	71.7	0.00400	□@	0.000287	50	0.00400	□@	0.0002	30	0.00400	□@	0.00012	42.9	0.00400	□@	0.000171
Duck	□@	0.0244	□@	□@	3.3	0.0244	□@	8.05E-05	2.20	0.0244	□@	5.37E-05	1.10	0.0244	□@	2.68E-05
Pork(Yang)	75.0	U.D.L..	□@	□@	50	U.D.L.	□@	□@	21.4	U.D.L.	□@	□@	□@	U.D.L.	□@	□@
Pork(Heng)	□@	U.D.L..	□@	□@	□@	U.D.L.	□@	□@	□@	U.D.L.	□@	□@	33.3	U.D.L.	□@	□@
Total	□@			3.18	□@			7.29	□@			6.77	□@			0.629

U	Hamlet-1	Concentration(ppb)		D.D.I microg	Hamlet-2	Concentration(ppb)		D.D.I microg	Hamlet-3	Concentration(ppb)		D.D.I microg	Hamlet-CA	Concentration(ppb)		D.D.I microg
	D.C.(g/p/b)	Average	S.D.		D.C.(g/p/b)	Average	S.D.		D.C.(g/p/b)	Average	S.D.		D.C.(g/p/b)	Average	S.D.	
Rice Grain	500	0.291	0.194	0.145	650	0.662	0.7900	0.430	750	0.115	0.113	0.086	600	0.0753	0.0163	0.0452
Water Sp.	94.6	2.39	1.16	0.226	500	1.97	1.46026	0.983	500	5.01	3.24	2.505	200	0	0	□@
Cabbage	214	□@	□@	□@	200	□@	□@	□@	500	□@	□@	□@	300	□@	□@	□@
Sweet Po.	37.5	0.0449	□@	0.00168	200	0.805	□@	0.161	500	□@	□@	□@	68.5	0.0492	□@	0.00337
Fish	71.7	0.0448	□@	0.00321	50	0.0448	□@	0.00224	30.0	0.0448	□@	0.00134	42.9	0.0448	□@	0.00192

Duck	□@	0.05 74	□@	□@	3.3	0.05 74	□@	0.000 189	2.20	0.05 74	□@	0.000 126	1.10	0.05 74	□@	6.31 E-05
Pork(Yang)	75	U.D.L. .	□@	□@	50	U.D.L. .	□@	□@	21.4	U.D.L. .	□@	□@	□@	U.D.L. .	□@	□@
Pork(Heng)	□@	U.D.L. .	□@	□@	□@	U.D.L. .	□@	□@	□@	U.D.L. .	□@	□@	33.3	U.D.L. .	□@	□@
Total	□@			0.37 6	□@			1.58	□@			2.59	□@			0.05 05

D.C. : Daily Consumption of food D.D.I. : Daily Dietary Intake U.D.L. : Under Detection Limit

## 52. Precise Determination of the Isotopic Composition of Tellurium by Negative Thermal Ionization Mass Spectrometry

Sarata Kumar Sahoo, Hidenori Yonehara, Katsumi Kurotaki, Shigekazu Yoneda<sup>1</sup> and Akimasa Masuda<sup>2</sup> (<sup>1</sup>National Science Museum, <sup>2</sup>University of Tokyo)

**Keywords:** tellurium, isotopic composition, negative thermal ionization mass spectrometry

Precise determination of the isotopic composition of tellurium is of great interest in various fields such as geochemistry, cosmochemistry and environmental sciences. The relative abundance of Te in natural samples is not well documented. In fact, nature has provided three early solar system chronometers based upon refractory-siderophile (Ru, Pd) and volatile-chalcophile (Te) nuclide yields from <sup>244</sup>Pu spontaneous fission. Te has eight stable isotopes, <sup>120</sup>Te (0.096%), <sup>122</sup>Te (2.60%), <sup>123</sup>Te (0.908%), <sup>124</sup>Te (4.816%), <sup>125</sup>Te (7.139%), <sup>126</sup>Te (18.952%), <sup>128</sup>Te (31.687%) and <sup>130</sup>Te (33.799%) and it has a relatively high elemental abundance owing to its even atomic number (Z=52) and the relatively high abundance of its r process isotopes. Three of the isotopes are s-only <sup>122</sup>Te and <sup>124</sup>Te being shielded from the r-process by heavy tin isotopes, and <sup>123</sup>Te by <sup>123</sup>Sb. Te has a p-process nuclide <sup>120</sup>Te and two r-only isotopes <sup>128</sup>Te and <sup>130</sup>Te having enormously long half-lives of more than  $10^{24}$  y and  $10^{21}$  y. <sup>123</sup>Te, <sup>128</sup>Te and <sup>130</sup>Te isotopes are radioactive.

The development of high precision, high ion-yield, negative thermal ionization mass spectrometry (NTIMS) techniques for analysis at low quantity levels is considered important to produce reliable data in terrestrial and extraterrestrial samples. Isotopic analysis by NTIMS has been developed by K.G. Heumann and his coworkers. For non-metals and refractory metals with higher first ionization potential (>7eV) such as Mo, Te, Sn and W, the precision of TIMS measurements is usually restricted by low ionization efficiencies. Recently NTIMS has been widely used to determine the isotopic composition of refractory metals and the precision of the data has been improved considerably compared to that achieved by conventional PTIMS. This technique takes advantage of the much higher ionization efficiencies at lower temperature for negatively charged oxide ions relative to positively charged ions for non-metals and refractory metals, hence it is capable of making high precision isotope measurements.

For the NTIMS a VG Sector 54-30 thermal ionization mass spectrometer equipped with 9 Faraday cup collectors, a Daly-ion counting system, WARP (wide aperture retardation potential) filter and double filament ion source were used (Fig 17). The Pt filament was 0.03 mm thick and 0.75 mm wide. Twenty  $\mu$ g Ba as a solution of Ba (OH)<sub>2</sub> were deposited on the ionization filament and dried at a 0.6 A filament current in air. Addition of Ba reduces the electron work function of the Pt filament and promotes the production of negative thermal ions. 0.51.0  $\mu$ g Te as H<sub>2</sub> TeO<sub>3</sub> solution were deposited on the evaporation filament. After loading, the filaments were introduced into the mass spectrometer. Intense ion beams of negatively charged species of Te (Te<sup>-</sup>) were observed at 850-950 °C under an accelerating voltage of -6kV (ionization filament current 1.4-1.8 A, evaporation filament current 0.7-0.9 A). A mass spectrum obtained by NTIMS is shown in Fig 18. This method is free from oxygen correction during measurement.

In the past, isotope ratios of Te were usually determined by electron impact ionization or by positive TIMS. The samples are loaded in the later case by electroplating which is more time consuming and complicated. Since ion currents are low with those techniques, isotope ratios are measured by using a secondary electron multiplier detection system. The electron multiplier method introduces a mass discrimination into the isotopic

abundances, since the signal from a light isotope is enhanced with respect to the signal from heavier isotopes because the secondary electron yield at the first dynode is velocity dependent. This mass discrimination is approximately proportional to the square root of the mass ratio. Therefore to overcome this, the most suitable method is to measure the isotopic abundances of Te using Faraday cup mode of detection. This does not eliminate all the sources of mass spectrometer bias, but it does account for the major sources of mass discrimination which are introduced by the electron multiplier detection system. [Table 6](#) summarizes results obtained by other researchers who have measured the isotope ratios of Te. Since the present TIMS is equipped with the WARP filter, it is possible to measure the abundance of  $^{120}\text{Te}$ , which is an improvement over the earlier NTIMS technique. The determined ratios  $^{120}/^{130}$ ,  $^{122}/^{130}$ ,  $^{123}/^{130}$ ,  $^{124}/^{130}$ ,  $^{125}/^{130}$ ,  $^{126}/^{130}$  and  $^{128}/^{130}$  are within the precision range of 0.002 to 0.008j (relative standard deviation)

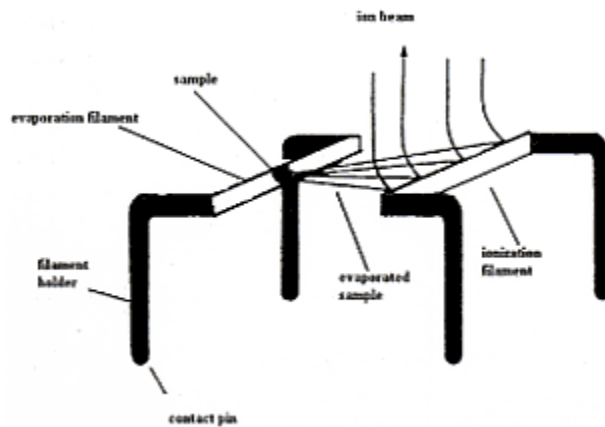


Fig.17. Schematic diagram of a double filament thermal ion source.

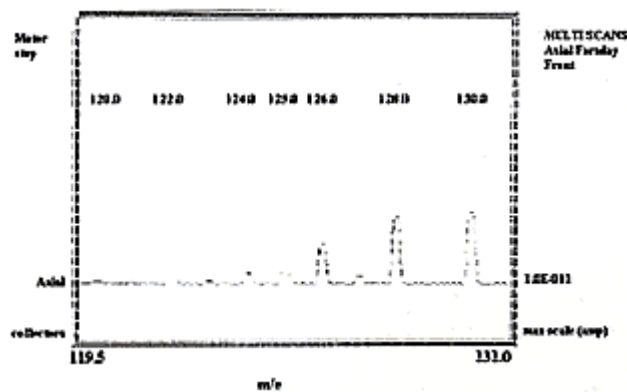


Fig.18. Mass spectrum of tellurium obtained by NTIMS using a single collector.

Table 6. Comparison of Tellurium Isotopic Composition

Researcher	Method	$^{120}\text{Te}/^{130}\text{Te}$	$^{122}\text{Te}/^{130}\text{Te}$	$^{123}\text{Te}/^{130}\text{Te}$	$^{124}\text{Te}/^{130}\text{Te}$	$^{125}\text{Te}/^{130}\text{Te}$	$^{126}\text{Te}/^{130}\text{Te}$	$^{128}\text{Te}/^{130}\text{Te}$
Smith et al.	PTIMS (SEM)	0.00273(2) )	0.07460(1) )	0.02614(2) )	0.13917(6) )	0.20712(6) )	0.56073(14) )	0.93029(16) )
De Laeter	PTIMS (Faraday cup)	0.00268(3) )	0.07368(4) )	0.02584(3) )	0.13767(7) )	0.20551(5) )	0.54828(15) )	0.92688(14) )
Wachsman & Heumann	NTIMS (Faraday cup)	□@	0.0736(4)	0.0256(2)	0.1372(5)	0.2053(6)	0.5484(2)	0.928(1)
This study	NTIMS (Farady cup)	0.00265(2) )	0.07349(4) )	0.02576(2) )	0.13725(6) )	0.20533(6) )	0.54822(7)	0.92731(8)

---

## 53. Comparative Biokinetics of Tritium in Rats during Continuous Ingestion of Tritiated Water and Tritiated Food

**Hiroshi Takeda, Kiriko Miyamoto Shoichi. Fuma, Kei Yanagisawa, Nobuyoshi Ishii. and Noriko Kuroda**

**Keywords:** *tritiated water, tritiated wheat, biokinetics, dose estimation, rat*

In the present study, we investigated the dynamics of tritium in rats during about 100 days' continuous ingestion of tritiated water and tritiated wheat. Wistar strain male rats weighing about 450 g were used. Sixty rats were separated into two groups. Each group of rats were continuously ingested tritiated water as drinking water or tritiated wheat as food. Throughout the experiment, rats were housed in metabolic cages (JVIetabolica, Sugiyama gen Iriki Instrument Co.) in order to measure consumption of water and food and to collect daily samples of urine and feces from each animal. Tritiated water was purchased from NEN and diluted to an appropriate concentration with distilled water to prepare the tritiated drinking water and tritiated food. The concentration of tritium in drinking water was adjusted to 6.3 kBq/ml. For preparation of tritiated food, wheat was grown in a 1/50 m<sup>2</sup> plastic Wagner's pot in a metabolic chamber. After flowering the plant was sometimes irrigated with tritiated water. At the time of ripening, the plants were harvested and the edible part was used for administration to rats as a tritiated food. Before administration to rats, the tritiated wheat was pulverized, freeze-dried and mixed with the powdered standard chow. The concentration of tritium in the food including tritiated wheat was 0.18 kBq/g. The rats were sacrificed by decapitation under ether anesthesia on the 1, 2, 3, 4, 5, 6, 8, 10 and 14th week after beginning of the ingestion. Various tissue samples were taken from the sacrificed animals and immediately the activity of total tritium in the fresh wet tissues was determined. A part of each tissue sample was lyophilized for determination of OBT in dry tissue sample. All samples were combusted in an oxidizer and tritium activity in the combustion water was measured with a liquid scintillation counter.

Time-variations of the concentration of total tritium and OBT in the tissues of rats during the continuous ingestion of tritiated water showed that the concentrations of total tritium increased rapidly and attained an equilibrium state at 2-3 weeks after start of the exposure to tritiated water and the equilibrium state of OBT concentrations was observed at about the 4th week. In the case of the chronic exposure to tritiated food, the equilibrium state for both total tritium and OBT was not observed for 10 weeks after start of the exposure in almost all tissues except for liver, in which the equilibrium was attained at 4 weeks after start of the exposure. R-value, defined as the ratio of specific activity (T/H) of tritium in dry tissues to specific activity (T/H) of tritium in daily ingested drinking water or food, is an important factor for evaluating the extent of tritium incorporation into the tissue organic constituents of organism. In this study, R-values for different tissues of rats after 98 days' continuous ingestion of tritiated water and tritiated food were calculated. For this calculation, we used the values of hydrogen contents for organic component of various tissues given by Pietrzak-Flis et al. Hydrogen content for daily ingested drinking water should be 11.1% and that for tritiated food was estimated to be 7.0% from the list of its composition. Results are shown in [Table 7](#). We found that the R-values for the exposure to tritiated water ranged from 0.15 for heart to 0.24 for testis, while the R-values for the exposure to tritiated food ranged from 0.36 for brain to 0.78 for lung. Thus, the R-values for the exposure to tritiated food were obviously higher than those for the exposure to tritiated water. In the previous study, we have also estimated the R-values for the 22 days' chronic exposure to tritiated water and tritiated food (wheat).

Compared with this previous result, the present R-values for the exposure to tritiated water did not differ so significantly, but those for the exposure to tritiated food were evu dently greater. Nevertheless, they were never over 1.0, indicating that the specific activity of tritium in the tissue organic constituents of rat did not exceed the specific activity of tritium in the food as well as that in the drinking water.

The radiation dose rates from total tritium in the different tissues at the end of chronic exposure to tritiated water or tritiated food were calculated. OBT contribution to the total dose rates was also calculated using the data on the dose rates from OBT and the water content for individual tissue. [Table 8](#) shows the calculated dose rates and OBT contribution. The ratios of the dose rates from the ingestion of tritiated food to those from the ngestion of tritiated water are also given. The total dose rates from the exposure to tritiated food were higher than those from the exposure to tritiated water by a factor of 1.3 to 4.5 but the factors were within 2 in the majority of tissues except for small intestine and adipose tissue.

In our previous study in which tritiated water and tritiated wheat were continuously ingested for 3 weeks, the dose rates from tritiated foods were higher than those from tritiated water by a factor of 2.1 to 3.6. The results of the present study, therefore, indicated that the difference in the dome rates between tritiated water and tritiated foods would not increase by lengthening the period of chronic ex posure.

Table 7. Ratio of Specific Activity (T/H) of Tritium in the Dry Tissue to Specific Activity (T/H) of Tritium in the Daily Ingested Tritiated Food in the 14thWeek of Chronic Exposure

Tissue	Hydrogen content(%)	R value (Ratio of T/H in dry tissue to T/H in the daily ingested HTO or <sup>3</sup> h-food)	
		Tritiated water	Tritiated food
Liver	7.11	0.23	0.70
Kidney	7.62	0.20	0.62
Testis	6.32	0.24	0.68
Spleen	6.12	0.19	0.69
Brain	9.26	0.16	0.36
Muscle	5.93	0.21	0.67
Small intestine	7.95	0.17	0.56
Lung	5.61	0.23	0.78
Heart	8.15	0.15	0.59
Adipose tissue	11.69	0.13	0.36

Table 8. Radiation Dose Rates from Total Tritium and OBT Contribution to the Dose Rates in the 14th Week of Chronic Exposure to Tritiated Water and Tritiated Wheat.

Tissue	Dose rate (mGy/day) <sup>a</sup> and OBT contribution <sup>b</sup>		
	Tritiated water	Tritiated food	<sup>3</sup> H-food/HTO
Liver	18(11.3)	36(49.3)	2.1
Kidney	20( 7.7)	34(39.8)	1.7
Testis	22( 4.3)	28(24.3)	1.3
Spleen	20( 6.6)	31(37.5)	1.6
Brain	17( 8.9)	30(29.4)	1.8
Muscle	19( 7.0)	30(36.8)	1.6
Small intestine	17( 8.5)	44(30.0)	2.6
Lung	19( 6.8)	30(36.9)	1.6
Heart	19( 7.0)	31(45.3)	1.6
Adipose tissue	9(66.4)	42(82.0)	4.5

<sup>a</sup> : The dose rates were calculated assuming tritium exposure to be 3.7 MBq/g body weight.

<sup>b</sup> : OBT contribution is expressed as a percentage of total dose rate, which is shown in parentheses

---

## 54. Determination of $^{99}\text{Tc}$ Deposited on the Ground within the 30-km Zone around the Chernobyl Reactor and Estimation of $^{99}\text{Tc}$ Released into Atmosphere by the Accident

S. Uchida, K. Tagami, W. Ruhm<sup>1</sup> and E. Wirth<sup>2</sup> (<sup>1</sup>Institute for Radiation Biology Ludwig Maximilians Universitat Munchen, Germany; <sup>2</sup>Federal Office for Radiation Protection, Institute of Radiation Hygiene, Germany)

**Keywords:**  $^{99}\text{Tc}$ , Chernobyl accident, forest soil, deposition,  $^{137}\text{Cs}$ , migration

There have been many reports concerning radionuclides' concentrations in environmental samples due to the accident in Unit 4 of the Chernobyl Nuclear Power Station (CNPS). At present, however there are almost no data on  $^{99}\text{Tc}$  contamination of environmental samples and consequently, limited information on the  $^{99}\text{Tc}$  activity released by the Chernobyl accident is available. In this study, results of  $^{99}\text{Tc}$  and  $^{137}\text{Cs}$  measurements in samples taken from three forest sites within the 30-km zone around the CNPS are presented.

Soil samples collected within three forest sites around Chernobyl in 1994 and 1995 were used. The sites DI and D3 are located 28.5 km and 26.0 km to the south of the CNPS, respectively, while K2 is located 6.0 km to the southeast of the CNPS. The  $^{137}\text{Cs}$  activities in the samples were measured with a Ge detector system before chemical separations. Then, the  $^{99}\text{Tc}$  concentrations in each solution were determined by ICP-MS after the chemical separation.

We plotted our data for  $^{137}\text{Cs}$  in addition to the data given by Aarkrog et al. (J. Environ. Radioact 6, 151-162, 1988) versus distance from the CNPS. A least squares fit of these data gives a regression function of  $D_{\text{Cs}} = 5.14 \times 10^4 R^{-1.477}$  where  $D_{\text{Cs}}$  is the  $^{137}\text{Cs}$  deposition on the ground ( $\text{GBq km}^{-2}$ ) and  $R$ , the distance from the CNPS (km) (see Fig. 19) Assuming the same horizontal distribution of the  $^{137}\text{Cs}$  deposition in all directions from the CNPS, we calculate the  $^{137}\text{Cs}$  release as

$$\int_1^{10000} 2\pi R \times 5.14 \times 10^{-2} \times R^{-1.477} dR \approx 76 \text{ PBq.}$$

A similar procedure was applied in order to estimate the  $^{99}\text{Tc}$  release due to the accident, using our  $^{99}\text{Tc}$  depositions for distances of 6 km (K2), 26 km (D3), and 28.5 km (DI). For a distance of 1000 km, we assumed the  $^{99}\text{Tc}$  deposition from the  $^{99}\text{Tc}/^{137}\text{Cs}$  ratio of  $1.01 \times 10^{-5}$  given by Aarkrog et al. The resulting regression function is  $D_{\text{Tc}} = 4.88 \times R^{-1.771}$  where  $D_{\text{Tc}}$  is the  $^{99}\text{Tc}$  deposition on the ground ( $\text{GBq km}^{-2}$ ) and  $R$ , the distance from the CNPS (km) (see Fig. 19). Again, the release may be calculated by integration over  $R$  as

$$\int_1^{10000} 2\pi R \times 4.88 \times R^{-1.771} dR \approx 970 \text{ GBq.}$$

The total core inventory of  $^{137}\text{Cs}$  is estimated to range from 210-290 PBq. A  $^{137}\text{Cs}$  release of 76 PBq, as estimated in this paper, corresponds therefore to a fraction of 26% to 36% of the total  $^{137}\text{Cs}$  core inventory. From the inventory of  $^{137}\text{Cs}$  and from the theoretical ratio of  $^{99}\text{Tc}$  to  $^{137}\text{Cs}$  of  $1.4 \times 10^{-4}$  the total inventory of  $^{99}\text{Tc}$  can be calculated to range from 30 to 40 TBq. Consequently, the percentage of  $^{99}\text{Tc}$  released into the atmosphere by the accident could be estimated to range from 2% to 3%. This result is close to the estimate given by Aarkrog et al. who suggested the release percentage of  $^{99}\text{Tc}$  would be an order of magnitude less than that of  $^{137}\text{Cs}$ . However, our result is higher by a factor of 3 to 4 compared to the estimate of the release percentage of  $^{103}\text{Ru}$  and  $^{106}\text{Ru}$  given in the report of Gudiksen et al., which is

believed to be similar to the release percentage of  $^{99}\text{Tc}$ . Since data on  $^{99}\text{Tc}$  concentrations in environmental samples are quite limited, further investigations are required for a precise estimate of the amount of  $^{99}\text{Tc}$  released by the accident.

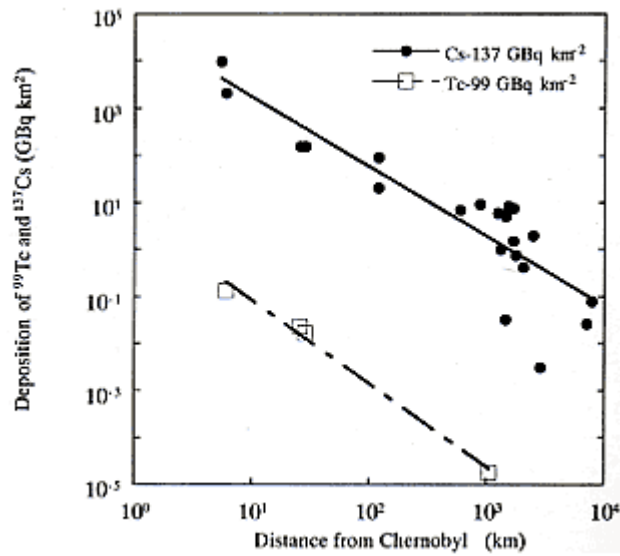


Fig.19.  $^{137}\text{Cs}$  and  $^{99}\text{Tc}$  deposition as function of distance from Chernobyl.  $^{137}\text{Cs}$  deposition data are from this study and from Aarkrog et al.  $^{99}\text{Tc}$  deposition data are from this study and from Aarkrog et al. which was estimated for a distance of 1000 km.

**Publicatton:**

Uchida, S., Tagami, K., Ruhm, W. and Wirth, E. Chemosphere, 39, 2757-2766, 1999.

---

## 55. Determination of Uranium Isotopes in Soil and Plant Samples Collected around the Uranium Conversion Building on the JCO Grounds Following the Criticality Accident

Satoshi Yoshida, Yasuyuki Muramatsu, Keiko Tagami, Shigeo Uchida, Tadaaki Ban-mat, Hidenori Yonehara and Sarat Kumar Sahoo

**Keywords:** JCO criticality accident, uranium,  $^{235}\text{U}$ / $^{238}\text{U}$ , isotope ratio, soil, plant, ICP-MS

Appreciable amounts of gaseous fission products and activation products were observed in some soil and vegetation samples collected near the JCO campus immediately after the criticality accident on September 30, 1999. However, there were almost no data on the levels of U in the environment around the uranium conversion building. Since enriched U (18.8% of  $^{235}\text{U}$  by mass) was used in this facility the  $^{235}\text{U}/^{238}\text{U}$  ratio might be useful in assessing the possible contamination of U. In the framework of studies on environmental effects of the criticality accident, we collected soil and plant samples on the JCO grounds.

This study determines the U isotopes ( $^{235}\text{U}$  and  $^{238}\text{U}$ ) in these soil and plant samples.

Surface (0-5 cm) soil samples were collected around the uranium conversion building on October 7, 1999. Sampling points were decided considering the distance and direction from the center of the building. After removing stones, the soils were oven-dried at 80 °C until constant weight, and ground into powder. Plant samples belonging to four species were collected around the building on October 26, 1999. In the laboratory, leaves were oven-dried at 80 °C until constant weight and pulverized with a blender. Samples (0.1 g for soils and 0.2 g for plants) were digested with  $\text{HNO}_3$ , HF and  $\text{HClO}_4$ . A microwave digester (CEM, MDS-2000) was used for heating the samples. After digestion, the samples were evaporated to dryness on a hot plate. Then, the residues were dissolved in 1-2%  $\text{HNO}_3$  to yield the sample solutions. Decomposition and analysis were duplicated for each sample. ICP-MS (Yokogawa PMS-2000) was used for the analysis of  $^{235}\text{U}$  and  $^{238}\text{U}$ .  $^{232}\text{Th}$  was also measured for soil samples. Standard reference materials such as GSJ-JB-1a (basalt) and NIST-SR1573a (tomato leaves) were used to validate the analytical procedure. Concentrations of U in soils were comparable to the U values for common Japanese soils. However, the U/Th ratios for these soil samples were markedly higher than the control value, suggesting the possible contamination of U. The  $^{235}\text{U}/^{238}\text{U}$  atom ratios in soil and plant samples were notably higher than the natural ratio, 0.00725. The highest values, 0.0162 for soil and 0.0193 for plant were found in samples collected near the conversion building as shown in Fig. 20. However, a relatively high ratio was observed at the site more than 50 m from the building, indicating that enriched U may have been released not only from the conversion building, but also from other unknown sources. The  $^{235}\text{U}/^{238}\text{U}$  atom ratios were in general higher in plants than those in soils collected at the same points.

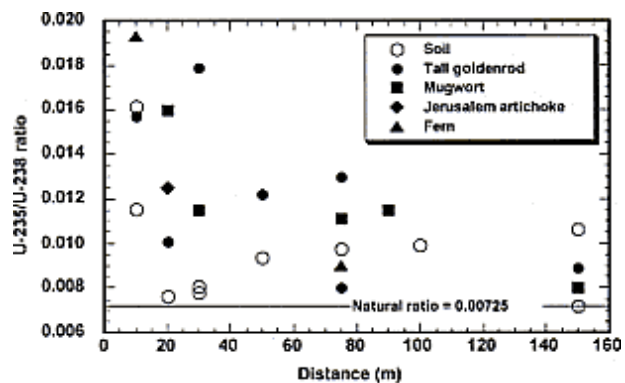


Fig.20.  $^{235}\text{U}/^{238}\text{U}$  atom ratio in soils and plants with function of distance from the JCO uranium conversion building.

□

**Publication:**

Yoshida, S., Muramatsu, Y., Tagami, K., Uchida, S. Ban-nai, T., Yonehara, H. and Sahoo, S.: J Environ. Radioactivity, 50, 161-172, 2000.

## 56. Use of a Combustion Apparatus for Lowlevel $^{99}\text{Tc}$ Separations from Soil Samples

**Keiko Tagami and Shigeo Uchida**

**Keywords:**  $^{99}\text{Tc}$ , volatilization, ICP-MS, soil sample

In the present study,  $\text{To}$  volatilization behaviour was studied to improve our analytical method for  $^{99}\text{Tc}$  ( $T_{1/2}=2.1 \times 10^5\text{y}$ ) in environmental soil samples by ICP-MS.

A soil contaminated with  $^{99}\text{Tc}$  for 1 y (1-y-aged) was used. At first, the soil was heated in an electrical oven at 450 C for 8 h to decompose organic matter. Then 80 g of the incinerated soil, which had already been contaminated with  $^{99}\text{Tc}$ , was mixed with  $^{99\text{m}}\text{Tc}$  3 h before using in the test (freshly added). The sample contaminated with both  $^{99\text{m}}\text{Tc}$  and  $^{99}\text{Tc}$  was heated from 500 to 1000 C in 100 C increments. The volatilization at 1000 C was carried out twice. The temperature was raised to the next step during a 10 min period and held there for 50 min. The oven, which was set just before the traps, was kept at 1000 C during the study to avoid Tc fixation on the inside of the outer quartz tube.

The trap solutions, each containing 150 ml of deionized water, were changed at the end of each step, then 100 mL of a trap solution was transferred into a plastic vessel (250 ml). The activity of  $^{99\text{m}}\text{Tc}$  in the solution was measured with the Ge detector system. For  $^{99}\text{Tc}$  measurement, the trap solution was passed through a TEVA resin column (Eichrom Industry Inc.) to separate and concentrate the nuclide. The  $^{99}\text{Tc}$  concentration was measured by ICP IVYS (Yokogawa, PMS-2000)

The percentages volatilized for  $^{99\text{m}}\text{Tc}$  and  $^{99}\text{Tc}$  were almost the same; these Tc isotopes showed the same volatility behaviour although their contaminated periods differed. Thus, the freshly added  $^{99\text{m}}\text{Tc}$  could be used as a yield monitor of originally included  $^{99}\text{Tc}$ .

The volatility of  $^{99\text{m}}\text{Tc}$  from the Andosol soil sample is shown in Fig. 21. The  $^{99\text{m}}\text{Tc}$  volatility increased with temperature. However, the result of continuous heating at 1000 C showed no remarkable increase.

Technetium in the soil sample might not be completely volatilized even if the temperature of 1000 C was maintained for a longer time. In our separation scheme, therefore, we decided to heat the soil sample for 3 h at 1000 C

From the results, procedures to improve the method were changed as follows: 1)  $\text{To}$  in soil (incinerated at 450 C) is volatilized in a combustion apparatus for 3 h at 1000 C and trapped in deionized water. 2) The trap solution is passed through a TEVA resin to remove Ru and to concentrate Tc. 3) After the eluate with 8M  $\text{HNO}_3$  containing  $\text{To}$  is evaporated to dryness,  $\text{To}$  is dissolved in a 2%  $\text{HNO}_3$  solution. 4)  $^{99}\text{Tc}$  in the solution is measured by ICP-MS.

Three environmental soil samples were treated by the method to determine their  $^{99}\text{Tc}$  concentration. The recoveries varied from 62 to 73%. Although soil samples differed from one another in their land usages and soil types, we saw that the recoveries were almost the same. The  $^{99}\text{Tc}$  concentrations in these soils were 5 to 30  $\text{mBq kg}^{-1}\text{Tc}$  dry weight basis.

The values were similar to previous reports.

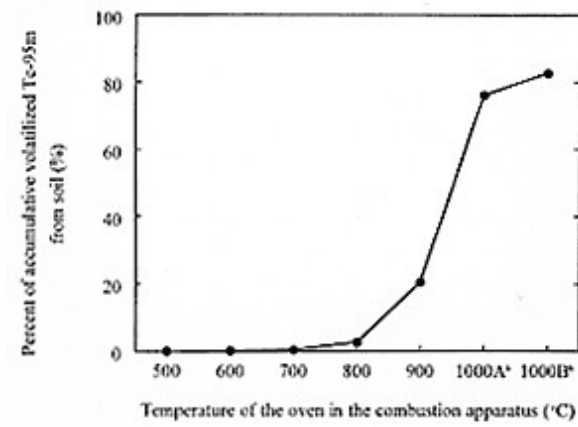


Fig.21. Temperature effect on Tc volatilization from Andosol sample<sup>a</sup>. a: The soil sample was volatilized for 1 h at each temperature. b: 1000A and 1000B: First and second volatilizations at 1000 C

**Publication:**

Tagami, K. and Uehida, S.: Radioact. Radiochem.10 30-34, 1999.

---

## 57. An Ecological Evaluation of Gadolinium Toxicity Using an Aquatic Microcosm

Shoichi Fuma, Hiroshi Takeda, Kiriko Miyamoto, Ket Yanagusawa, Yoshikazu Inoue, Nobuyoshi Ishii, Kazunori Sugai, Chitose Ishii and Zen'ichiro Kawabata\* (\*Kyoto University)

**Keywords:** aquatic microcosm, ecological assessment, *Escherichia coli*, *Euglena gracilis*, gadolinium, model ecosystem, *Tetrahymena thermophila*

Gadolinium (Gd) is one of the rare earth metals. It has been used as an admixture to superconductors, magnets, fluorescent materials, electronic materials, glasses and so on. It has also been recently used as a paramagnetic contrast-enhancing agent in nuclear magnetic resonance imaging (MRI). It is possible that natural ecosystems will be damaged by the increasing industrial and medical uses of gadolinium. However, there are few trials for ecological evaluation of gadolinium toxicity, especially at the community level. The authors investigated gadolinium toxicity to microbial communities of an aquatic microcosm.

The microcosm used in this study was developed by Kawabata et al. (V. Protozool. Res., 5, 23-26, 1995). It consists of flagellate algae *Euglena gracilis* Z as a producer, ciliate protozoa *Tetrahymena thermophila* B as a consumer and bacteria *Escherichia coli* DH5  $\alpha$  as a decomposer. The details of procedures of the microcosm's construction, its incubation and measurement of the population densities of each microorganism are in the literature (for example, Fuma et al., Int. J. Radiat. Biol., 74, 145-150, 1998).

The population change of each organism in the microcosm reaches a steady state 50 days after inoculation as a result of interactions between the species. All species can co-exist in the microcosm for as long as one year. In the case that each organism is cultured alone in the same medium and conditions as the microcosm, *T. thermophila* dies out without reaching a steady state. *T. thermophila* cannot exist without *E. coli*, because *T. thermophila* grazes *E. coli* as its staple food. The microcosm is maintained with energy of protease peptone in the early stage of culture. After exhaustion of protease peptone, it is maintained with energy which *E. gracilis* fixes by photosynthesis. Each species is supported with metabolites or the breakdown products of the other two species. The microcosm is therefore considered to simulate a basic process in aquatic microbial communities. It also makes the microcosm available as an ecotoxicological test tool because there is good repeatability in these population changes in the microcosm and pure-culture systems, respectively.

In this study, the microcosm system, and pureculture system of *E. gracilis* and *E. coli* were exposed to gadolinium on the 56th, 58th and 59th day after the beginning of the culture, respectively. As for *T. thermophila* pure-culture system, *T. thermophila* was inoculated to the microcosm medium to which gadolinium had been added. Gadolinium was added to each system in the form of  $\text{GdCl}_3$  solution at nominal concentrations of 50, 100, 300 and 1000  $\mu\text{mol}$  of total gadolinium atoms per a liter ( $\mu\text{mol/L}$ ). The same volume of distilled water was added to each system for controls. There were three replicates for each treatment.

[Fig. 22](#) shows the changes in the population densities of the three species in the microcosm after exposure to gadolinium. In controls, the populations of each species remained almost constant for the duration of the experiment. At 50  $\mu\text{mol/L}$  gadolinium, the population of no species in the microcosm were affected significantly. However, the population of *E. coli* showed a tendency to be larger than the controls, though this increase was not statistically significant. At 100  $\mu\text{mol/L}$ , the population of *E. coli* temporarily decreased compared with controls, though this decline was not statistically significant. However the population of *E. coli*

recovered to the control levels soon, and after the 32nd day of exposure they were maintained at larger levels than controls. The populations of the other two species in the microcosm were not affected. At 300  $\mu\text{mol/L}$ , *E. coli* almost died out just after exposure. The population of *T. thermophila* decreased, and became smaller than controls on the TLh day. This decline was maintained until the 50th day. However, the populations of *T. thermophila* recovered to control levels on the 87th day. The populations of *Eu. gracilis* at these three grades of concentrations were not affected significantly. At 1000  $\mu\text{mol/L}$ , all species died out just after exposure. Each species in the microcosm did not respond to gadolinium in the same manner as its constituents in pure-culture systems. For example, at 50 and 100  $\mu\text{mol/L}$  gadolinium, *T. thermophila* was not affected in the microcosm, while it died out earlier than controls in the pure-culture systems. At 300  $\mu\text{mol/L}$ , *T. thermophila* did not die out in the microcosm, though it temporarily decreased compared with controls. On the other hand, at the same concentration of gadolinium, pure-cultured *T. thermophila* did not grow at all, and died out much earlier than controls. At 300  $\mu\text{mol/L}$ , *Eu. gracilis* was not affected in the microcosm, while it died out in the pure-culture systems. This mitigation of gadolinium toxicity to *T. thermophila* or *Eu. gracilis* in the microcosm might arise from co-existence of other species. That is, there is the following possibility: (1) Coexisting species decreased gadolinium concentrations in the medium by absorption or adsorption of gadolinium. (2) Co-existing species transformed a chemical form of added gadolinium to a less toxic one. For example,  $\text{Gd}^{3+}$  might be chelated with metabolites or breakdown products of co-existing species. This is supported by the fact that adding organic ligands which can form a gadolinium organic species complex led to a great reduction of the gadolinium bioconcentration in algae (Sun et al. 1997), which is expected to reduce gadolinium toxicity to the algae. For another example, at 100  $\mu\text{mol/L}$ , the populations of *E. coli* in the microcosm temporarily decreased compared with controls, while *E. coli* cultured alone was not affected. This enhancement of effects on *E. coli* in the microcosm might arise from transformation of  $\text{Gd}^{3+}$  to more toxic chemical forms by co-existing *Eu. gracilis* or *T. thermophila*.

These results indicate that the microcosm responded to gadolinium at the community level despite its simplicity as shown to  $\gamma$ -rays and acidification. This suggests that the evaluation of gadolinium ecotoxicity by this microcosm test is more realistic than single-species tests, which are generally used for ecotoxicity evaluation.

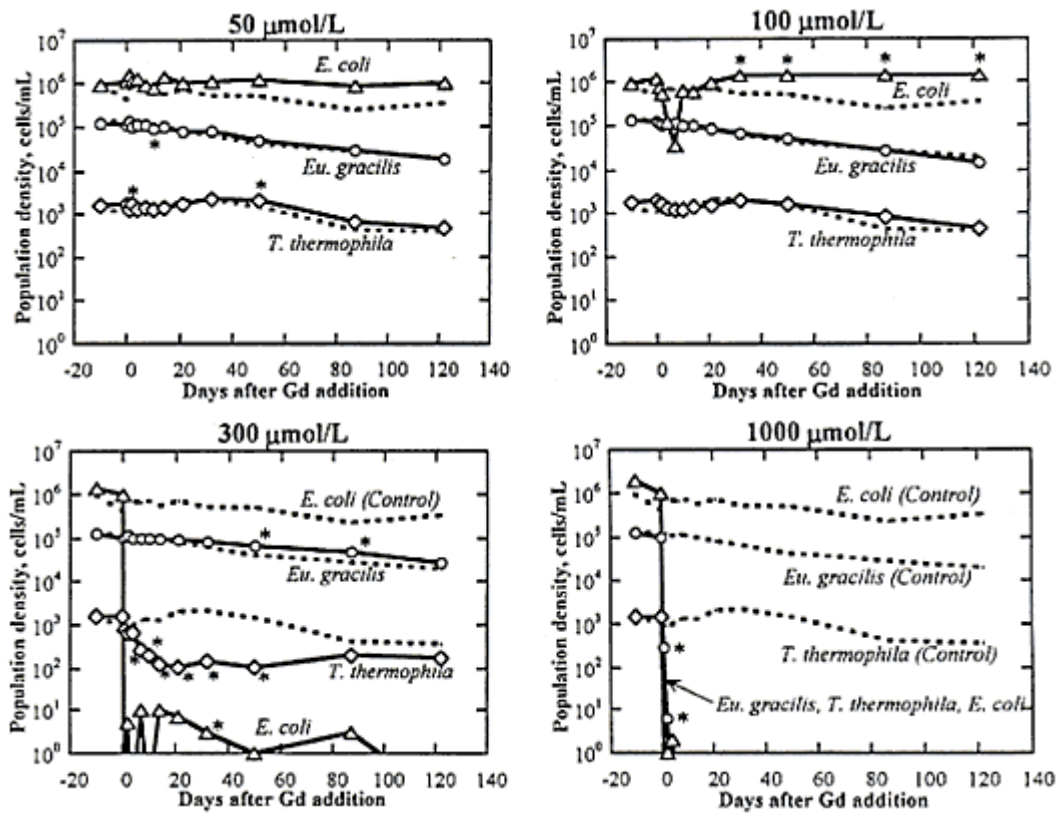


Fig.22. Effects of gadolinium on the populations in the microcosm. Solid lines represent results of the microcosm exposed to gadolinium. Broken lines represent results of controls. Values are the mean of three replicates. Asterisks indicate statistically significant differences from controls ( $p < 0.05$ , Student's t-test).

### Publications:

- 1)Fuma, S., Takeda, H., Miyamoto, K., Yanagisawa, K., Inoue, Y., Sato, N., Hirano, M., Kawabata, Z. Int. J. Radiat. Biol., 74, 145-150, 1998.
- 2)Fuma, S., Miyamoto, K., Takeda, II., Yanagisawa, K., Inoue, Y., Sato, N., Hirano, M., Kawabata, Z.:In: Inaba, J., Nakamura, Y. (eds). Comparative Evaluation of Environmental Toxicants-Health ef fects of Environmental Toxicants Derived from Advanced Technologies. Kodansha Scientific Ltd.,Tokyo, pp 131-144, 1998.

## 58. The Concentrations of Technetium-99 in *Sargassum thunbergii* along the Coast of the Japanese Islands

**Shigeki Hirano**

**Keywords:** *algae*,  $^{99}\text{Tc}$

Technetium-99 is already present in the terrestrial and the marine environment as a result of nuclear weapon tests carried out in the past. It is very important to study the distribution of the nuclide in the marine environment in regards to increasing number of power plants all over the world because of its high yield in nuclear fission, its long half- life, its high solubility and stability in water media, and its high concentration factor (CF) by brown algae.

We have been determining the concentration of the nuclide in algae collected along the coast of the Japanese Islands to assess an internal exposure to Japanese through marine foods. The concentration of the nuclide was also determined in seawater collected on the coast of Hitachinaka City.

It was found that the present level of the nuclide was very low in algae collected in most areas of Japan and this level was attributed to global fallout. However, it was found that a relatively high concentration of the nuclide was detected in samples collected in Hitachinaka City which neighbors Tokai Village where there are many nuclear facilities in operation. The concentration of the nuclide in the algae was in the range of 50 to 1,500 mBq/kg wet. It was found that the level of the nuclide in the algae in Kitaibaraki City was the same as that in other areas, except Hitachinaka City, despite the fact that Kitaibaraki City is also near Tokai. There is a down current along the coast of those areas so that northern sites are free from the influence of the emission of waste from Tokai. The level of the nuclide in the algae collected in Chiba Prefecture was low and the waste from Tokai did not reach this far and the concentration of the nuclide in the algae was below 10 mBq/kg wet. The concentration of the nuclide in seawater was not detected in most samples obtained along the coast of the Japanese Islands. However, in Hitachinaka City, the concentrations of the nuclide were detected several times through the year and the values varied from below the detection limit, 10mBq, to 230mBq/m<sup>3</sup>.

---

## 59. Space Radiation Dosimetry Using Solid State Integrating Detectors

Hiroshi Yasuda, Masashi Takada, Kazunobu Fujitaka, Sayaka Sato<sup>1</sup> and Tatsuto Komiyama<sup>2</sup> (<sup>1</sup>Tohoku University, <sup>2</sup>NASDA)

**Keywords:** space radiation dosimetry, solid-state detectors, HIMAC

In the early 21<sup>st</sup> century, Japanese astronauts will begin to continuously stay in the International Space Station (ISS). Even without a severe solar-particle event (SPED, the personal dose equivalent in a ISS mission will be higher than the occupational dose limit recommended by ICRP. Thus, career dose to each astronaut must be monitored and controlled in keeping with radiological protection practices. However, much uncertainty still remains on the availability of existing personal dosimeters for use in space. In the present study, responses of several solid-state passive detectors were examined at HIMAC using heavy-ion beams with energy comparable to galactic cosmic rays. The detectors employed herein were: radiophoto-luminescent glass (RPL-glass) (SC-1, Toshiba Glass), thermoluminescent dosimeters of Mg<sub>2</sub> SiO<sub>4</sub>:Tb (MSO-rod/ disk, Kasei-optonics), BeO (BeO ceramic sheet, Goodfellow), <sup>6</sup>LiF:Mg,Ti (TLD-GOD Harshaw), <sup>7</sup>LiF:Mg, Ti, (TLD-700, Harshaw), and plastic nuclear-track detectors (CR-39) (HARZLAS TD-1, Fukui Chemical Industry Inc.). Radiophotoluminescent glass and several TLDs showed different dependence on LET. Glow-curve shapes of selected TLDs also changed for different particles. Strong dependence on beam incident angles was found in the track-formation sensitivity (S) of TD-1 plastic. Such systematic errors (type-B uncertainty) need to be conservatively incorporated in view of radiological protection.

The detectors listed above were used for space radiation measurements in three recent missions at the low-Earth orbit (400km X 51.6°) relevant to that of the ISS: the Mir Mission in 1997, the 8<sup>th</sup> Shuttle-Mir Mission (STS-89) in 1998, and the 9<sup>th</sup> Shuttle-Mir Mission (STS 91) in 1998. Different type detectors showed different dose values as gamma-ray equivalent. Based on the calibration data obtained in the ground-based experiments, spatial variations of both dose and quality in the spacecrafts were successfully evaluated by selected combinations of the solid-state detectors.

### Publications:

- 1) Yasuda, H.: *Radioisotopes*. 48, 645-647, 1999.
  - 2) Yasuda, H.: *J. Nucl. Sci. Technol.*, 36, 1105-1107 1999.
  - 3) Yasuda, H.: *J. Health Phys.* 34, 387-390, 1999.
  - 4) Yasuda, H., Komiyama, T., and Fujitaka, K.: *J. J Aerospace Environ. Med.* 36, 105-112, 1999.
  - 5) Yasuda, H. and Fujitaka, K.: *Radial. Prot. Dosim.* 87, 115-120 2000.
  - 6) Yasuda, H. and Fujitaka, K.: *Radiat. Prot. Dosim.* 87, 203-206 2000.
-

## 60. Difference in LET-RBE Spectra for Cell Killing Exposed to Accelerated Ion Beams

Yoshiya Furusawa, Mizuho Saito<sup>1</sup> Kumiko Fukutsu, Hiromi Itsukaichi, Kiyomi Eguchi-Kasai, Tatsuaki Kanai, Koichi Ando, Fumio Yatagai<sup>2</sup> Marcelo E. Vazquez<sup>3</sup>, Tracy. Yang<sup>4</sup> and Hiroshi Ohara<sup>5</sup> (<sup>1</sup>Chiba Univ.; <sup>2</sup>Inst. Phys. Chem. Res. <sup>3</sup>Brookhaven Natl. Lab. <sup>4</sup>NASA Johnson Space Center; <sup>5</sup>Okayama Univ.)

**Keywords:** heavy ion beam, LET, RBE

The relationship between the radiobiological effectiveness (RBE) of cell killing and linear energy transfer (LET) was obtained using V79 cells for <sup>28</sup>Si-, <sup>40</sup>Ar-, and <sup>56</sup>Fe-ion beams having LET among 55-800, 85-1500, and 150-6000 keV/ $\mu$ m, respectively, using HIMAC (NIRS, Chiba), RRC (RIKEN Wako), and AGS (BNL, New York). Cell survival curves and their parameters were obtained by a colony-forming assay and curve-fitting using the LQ-equation. The LET-RBE relationship for each ion could be well-fitted by a newly established fitting function to LET with 3 constants, i. e. maximum RBE, LET giving maximum RBE, and width of the peak. The maximum RBEs were found at around 200 keV/ $\mu$ m, and the values were 4.7 3.7 for Si-, Ar-, and Fe-ions. By increasing the particle atomic number, we found: a) a shift of the peak RBE towards a higher LET region, b) a decrease in the maximum RBE, and c) a less sharp fall-off of the RBE at very high LET. These data agree with previous results obtained with <sup>3</sup>He-, <sup>12</sup>C and <sup>20</sup>Ne ions, and point out a general behavior for splitting of RBE-LET curve for particles with different atomic number Z or mass number A.

The LET-RBE spectra on cell killing for cultured mammalian cells exposed to accelerated heavy ions were investigated in order to design a spread-out Bragg peak beam for cancer therapy at HIMAC prior to clinical trials. Human salivary-gland tumor originated HSG cells as well as V79 and TI cells were exposed to <sup>3</sup>He-<sup>12</sup>C and <sup>20</sup>Ne-ion beams with the LET ranging over approximately 20 600 keV/ $\mu$ m under both aerobic and hypoxia conditions. Cell survival curves were fitted by equations from the LQ-model and the target-model to obtain survival parameters. RBE, OER, and D<sub>0</sub>, were analyzed as a function of the LET. The RBE increased with LET showing the maximum at around 200 keV/ $\mu$ m, then decreased with LET. Clear splits of the LET-RBE or -OER spectrum were found among ion-species and/ or cell lines. The RBE for a <sup>3</sup>He-beam was higher than that of heavier ions, the LET that showed maximum RBE shifted to a higher LET region for heavier ions. The OER value was 3 for X-rays, but started to decrease at a LET of around 50 keV/ $\mu$ m, crossed 2 at around 100 keV/ $\mu$ m, and then reached the minimum above 300 keV/ $\mu$ m, though the values were greater than 1. The OER was significantly lower for <sup>3</sup>He-ions than others.

### Publications:

- 1) Durante, M., Furusawa, Y., Vlahjima, H., Gotoh, E.: 1111 Risk Evaluation of Cosmic-Ray Exposure in Long-Term Manned Space Mission. Fujitaka, K., et al. (eds.) Kodansha Scientific Lid., Tokyo, pp 71-81, 1999.
- 2) Ohara, H., Okazaki, N., Monobe, M., Watanabe, S. Minamihisamatsu, M., Furusawa, Y., Kanau, T.: In; Risk Evaluation of Cosmic-Ray Exposure in Long-Term Manned Space Mission. Fujitaka, et al. (eds.), Kodansha Scientific Lid., Tokyo, pp. 101 108, 1999.
- 3) Vazquez, M.F., Saito, M., Nojima, K., Furusawa, Y., Pelzer, A.: Proceedings of 10th Annual Space Radiation Health Investigators Workshop. Brookhaven National Laboratory, New York, 1999.5.

4)Furusawa, Y., Saito, M., Kanai, T., Yatagai, F Vazquez, M., and Yang, TC. : International Congress of Radiation Research, Dublin, 1999.

---

## 61. Effects of high LET particles on Radio-resistant cells and the Molecular Biological Factors

Hideyuki INAJIMA, Chizuru Yamaguchi, Shizuko Kakinuma, Koichi Ando and Kazunobu Fujitaka

**Keywords:** *radio-resistant cell, mitochondria DNA, HIMAC*

Radiobiological effects of  $^{12}\text{C}$  ion-beams accelerated at HIMAC were examined. The biological effects following the irradiation were determined by colony formation methods to obtain survival curves as a function of dose. The cell line used in this study is 143B a human osteosarcoma cell line which is extremely resistant to low LET x-ray irradiation. The cells without mitochondria DNA from the 143B was established from the cells (Rho 0 cells) which were extremely sensitive to X-rays. The cells, in which normal mitochondria were brought to the Rho cells, (87wt), were in middle range in the sensitivity. Effects of  $^{12}\text{C}$  ion-beams with different LET i. e. 13 and 77 keV/  $\mu\text{m}$  were examined in the three cell lines. The Rho 0 cell sensitivity to 13keV/  $\mu\text{m}$  beam was the highest and followed by 87wt and 143B. The sensitivity to 77 keV/  $\mu\text{m}$  of Rho 0 was also the highest, although the differences were not substantial in the sensitivity among the three cell lines, suggesting mtDNA lacking Rho 0 cells might have a small capability in double-strand DNA repair.

### **Publications:**

1)Yong Xu, Anuradha Krishnan, X. Steven Wan, Hideyuki Majima, Che-Chung Yeh, Gabriele Ludewig, Edward J. Kasarskis, and Daret K. St Clair: *Oncogene*, 18, 93-102, 1999.

2)Yong Xu, Kelley K. Kinningham, Madhav N Devalaraja, Che-Chung Yeh, Hideyuki Majima, Edward J. Kasarskis and Daret K. St. Clair: *DNA and Cell Biology*, 18, 709-722, 1999.

---

## 62. International Research Promotion Office

**Masako Kimura, Etsuko Ito Hiroko Tanaka, and Kazunobu Fujitaka**

**Keywords:** *international collaboration, space radiation, research promotion*

When the former Third Research Group made a fresh start as the International Space Radiation Laboratory in April 1999, the International Research Promotion Office was established as a new function to arrange and promote research collaboration on a worldwide basis in order to advance space medicine. The year 1999 is particularly marked by the fact that post-doctoral fellows have joined us for the first time, which significantly contributed to the revitalization of our laboratory. Also, we made efforts throughout the year to increase opportunities to work in collaboration by inviting many researchers from abroad and sending our researchers out to participate in workshops, conferences and experiments abroad as well as inside the country. We held an international workshop in February 2000, where leading researchers gathered from the US, Canada, Germany, Italy, Russia, China and IAEA to discuss research strategies in supporting manned space missions and the International Space Station (ISS). It is worth noting that this workshop was the first in the world in terms of international organizations officially joining discussions on space medicine, and served as a forum for an active exchange of opinions on future research collaboration, contributing to the creation of a better international network in this field.

---